3-17-2015

A Technical and Economic Comparative Analysis of Sensible and Latent Heat Packed Bed Storage Systems for Concentrating Solar Thermal Power Plants

Jamie Trahan
University of South Florida, jltrahan80@gmail.com

Scholar Commons Citation
Trahan, Jamie, "A Technical and Economic Comparative Analysis of Sensible and Latent Heat Packed Bed Storage Systems for Concentrating Solar Thermal Power Plants" (2015). *Graduate Theses and Dissertations.*
https://scholarcommons.usf.edu/etd/5598

A Technical and Economic Comparative Analysis of Sensible and Latent Heat Packed Bed Storage Systems for Concentrating Solar Thermal Power Plants

by

Jamie Trahan

A dissertation submitted in partial fulfillment
of the requirements for the degree of
Doctor of Philosophy
Department of Mechanical Engineering
College of Engineering
University of South Florida

Co-Major Professor: D. Yogi Goswami, Ph.D.
Co-Major Professor: Delcie Durham, Ph.D.
Elias Stefanakos, Ph.D.
Frank Pyrtle, Ph.D.
Viktoria Martin, Ph.D.

Date of Approval:
March 17, 2015

Keywords: Cascaded Storage, Thermal Energy Storage, High Temperature Phase Change, Economic Study, Molten Salt CSP

DEDICATION

This dissertation is dedicated to my family and community for their endless support and inspiration, and especially to my father, whose passionate and radical soul taught me the value of justice and love. I would also like to dedicate this to my dear friend Dana Landry, whose loving, care-free spirit continues to dance its way into our hearts and minds.

ACKNOWLEDGMENTS

Though a long and arduous journey, the course of this degree has been a formative and essential period of personal growth. For the sake of brevity, I cannot acknowledge all who have touched my life and walked with me on this journey. But I am grateful for you.

First and foremost, I would like to thank my major advisor Dr. Yogi Goswami for his guidance, inspiration, and words of encouragement. I feel honored to have worked under the auspices of such a passionate, wise, and caring individual whose devotion to the field of solar energy has and will always influence others to positively impact the world. I am forever grateful for my co-major advisor, Dr. Delcie Durham. I aspire to one day walk with her same degree of strength, brilliance, and compassion. I am eternally indebted to you both for all of the opportunities you have afforded me.

I would like to acknowledge Dr. Elias Stefanakos, for his years of sound advice, and to my committee members Dr. Frank Pyrtle and Dr. Viktoria Martin - your support is strongly appreciated. I would also like to thank Dr. Autar Kaw for being a friend and mentor. Thank you Chuck, Barbara, Sarada, Ginny, Saeb, Antonio, Yang Yang, Rajeev, Abhinov, Tanvir, Mehdi, Arun, Phil, Chatura, Dr. Jotshi, Dr. Jaspreet, and Dr. Krakow for the years of support. I would like to gratefully acknowledge Roman Henneberg and Alessandro Graziani, who assisted me in constructing the prototype system. I am grateful for the GAANN fellowship, mentors, and fellows, who share the same passion for sustainability. And to my girlfriends whom I deeply cherish – thank you for sharing those countless hours of conversation, tears, and laughter. Alyse, Mara, Nyssa, Natalia, Rachana, Shirley, and Trina, you taught me to live and love with an open mind and open heart. To my family and friends who offered assistance while I took on the role as my father’s caregiver, you are truly appreciated. Last but not least is my mother, who has been my light in the darkest hours. Thank you for being a pillar of unending support.

TABLE OF CONTENTS

LIST OF TABLES

LIST OF FIGURES

ABSTRACT

Though economically favorable when compared to other renewable energy storage technologies, thermal energy storage systems for concentrating solar thermal power (CSP) plants require additional cost reduction measures to help transition CSP plants to the point of grid-parity. Thermocline packed bed storage is regarded as one potential low cost solution due to the single tank requirement and low cost storage media. Thus sensible heat storage (SHS) and latent heat storage (LHS) packed bed systems, which are two thermocline varieties, are frequently investigated. LHS systems can be further classified as single phase change material (PCM) systems or cascaded systems wherein multiple PCMs are employed.

This study compared the performance of SHS, single PCM, and cascaded PCM direct storage systems under the conditions that may be encountered in utility-scale molten salt CSP plants operating between 565°C and 288°C. A small-scale prototype SHS packed bed system was constructed and operated for use in validating a numerical model. The drawbacks of the latent heat storage process were discussed, and cascaded systems were investigated for their potential in mitigating the issues associated with adopting a single PCM. Several cascaded PCM configurations were evaluated. The study finds that the volume fraction of each PCM and the arrangement of latent heat in a 2-PCM and a 3-PCM system influences the output of the system, both in terms of quality and quantity of energy. In addition to studying systems of hypothetical PCMs, real salt PCM systems were examined and their selection process was discussed.

A preliminary economic assessment was conducted to compare the cost of SHS, single-PCM LHS, cascaded LHS, and state-of-the-art 2-tank systems. To the author’s knowledge, this is the first study that compares the cost of all three thermocline packed bed systems with the 2-tank design. The SHS system is significantly lower in cost than the remaining systems, however the LHS system does show

some economic benefit over the 2-tank design. If LHS systems are to be viable in the future, low cost storage media and encapsulation techniques are necessary.

CHAPTER 1: INTRODUCTION AND BACKGROUND

1.1 Introduction

While many renewable energy technologies continue to suffer from impediments in storage, concentrating solar thermal power (CSP) plants benefit from their capacity to adopt economical, easily dispatchable storage systems [1]. When implemented, these storage systems can mitigate the issue of solar radiation intermittency to varying degrees that are dictated by its size and function. Smaller systems for instance, may be designed to provide a few hours of storage for buffering during periods of cloud cover whereas larger systems can be employed to improve a plant's dispatchability [2]. In order to promote competition between CSP and fossil fuel powered plants and to ensure long-term market viability, storage systems must ultimately play a greater role in augmenting a plant's annual energy production.

Current state-of-the-art storage systems rely on the dual-tank method to store energy. As demonstrated in Figure 1, a liquid sensible heat storage medium either directly or indirectly captures thermal energy as the liquid is actively transferred from a "cold" tank to a "hot" tank. Though low-risk and simple in design, the cost of this approach remains in excess of a value that would advance CSP plants to the point of grid parity. Alternative, more robust storage methods may also be required as developments in CSP technology continue to expand and diversify. Consequently, numerous research efforts are directed at developing storage systems that manifest lower costs through reductions in storage material volume or equipment requirements.

Packed bed thermocline storage is one such alternative that has exhibited widespread investigation from lab-scale to large pilot-scale systems. They are deemed beneficial due to the single tank requirement and potential use of low-cost storage media. The storage media in a packed bed system remains stationary as a heat transfer fluid (HTF) transfers energy from the solar field to the storage material. In this process, known as charging mode, the hot HTF enters the system from the top of the tank and exits at a lower temperature from the bottom of the system before returning to the solar field. Ideally the outlet HTF temperature would be maintained at or near the initial bed temperature, indicating efficient and complete removal of the energy that is carried in by the HTF. When the stored energy needs to be retrieved, the reverse process, known as discharging mode, is enabled. “Cold” HTF enters the system from the bottom and is pumped up vertically to the top where it exits at the “hot” temperature and proceeds to the power block.

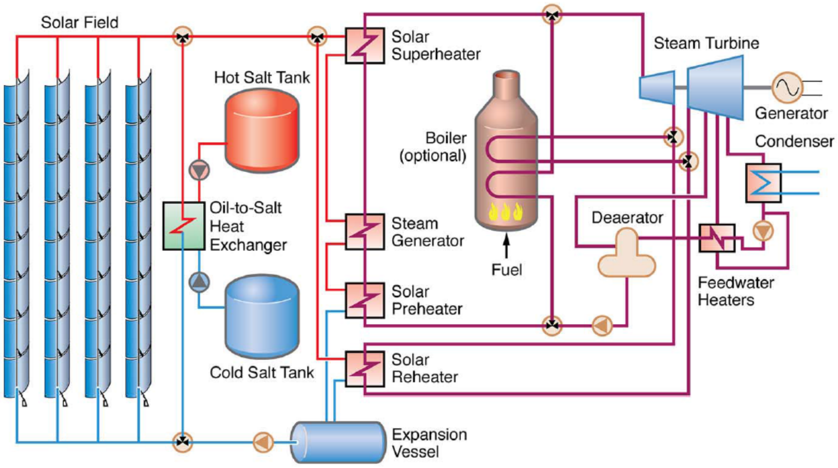

Figure 1. Configuration of a parabolic trough CSP plant with state-of-the-art indirect dual tank storage system [3]. (Copyright permission in Appendix C).

As illustrated in Figure 2, the storage process is characterized by the development of three distinct thermal zones along the height of the bed. At the onset of charging, the heat transfer fluid enters the tank and fills the pore space of the bed, exchanging energy with the solid media thus establishing a heat transfer region known as the thermocline zone. As charging progresses, the thermocline zone travels down the bed, leaving a high temperature region behind it and shortening the low temperature region below it. The nearly isothermal upper and lower regions of the tank are identified as the hot and cold zones, respectively. The heat transfer fluid and thermocline zone then move in the reverse direction during discharging mode. Thermal stratification is maintained by a density gradient which generates buoyancy forces that minimize mixing of the hot and cold zones. A well stratified system has a narrow thermocline region which enhances the operational efficiency of the system by maintaining low temperatures at the bottom of the tank during charging and a nearly constant exit temperature during discharging. Ineffective stratification results in exergy degradation characterized by high levels of mixing and loss of exergy as unutilized high temperature HTF exits the bed during charging mode [4].

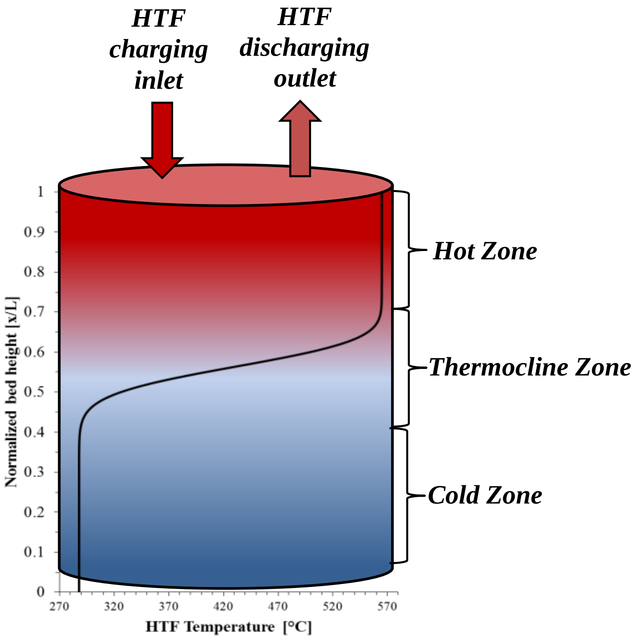

Figure 2. Schematic illustrating the zones of a thermocline storage tank.

Packed bed thermal energy storage (TES) systems can be categorized by the physical state of the material during which energy is stored and released. Sensible heat storage (SHS) packed bed systems are comprised of solid filler materials that exhibit a change in temperature as heat transfer occurs. Potential sensible heat storage media span a large breadth of materials including low cost substances such as sand and rock. Latent heat storage (LHS) systems consist of filler media that change phase, typically from solid to liquid, at a temperature that falls within the operating temperature range of the solar field. Their added value lies in reduced material requirements due to the high volumetric storage density that results from the phase change process. For high temperature utility-scale applications, whether sensible or latent heat storage, the filler material must be inert to the heat transfer fluid as well as any containment material. They mus also withstand thousands of thermal cycles.

Several studies have investigated the behavior and performance of packed bed latent heat storage systems. In such systems, the thermocline region consists not only of the sensible heat exchange zone, but is extended to include an iso-thermal heat exchange zone caused by the phase change process. The relative movement of these two heat exchange segments complicates the storage and removal of thermal energy and is heavily influenced by the thermophysical properties of the PCM, such as melting temperature and latent heat of fusion [5].

Numerous studies evaluate the thermodynamic efficiency and conduct parametric studies to assess the factors that influence system performance. Though these analyses evaluate metrics that are important in selecting a storage technique, economics ultimately defines its viability for commercialization. In order to elucidate whether latent heat storage exhibits economic gain over sensible heat storage due to the added energy density, an effort is made to compare the thermodynamic and economic efficiencies of these two storage types. The motivation for this work is to identify a cost-effective storage technology that can be commercially deployed in the near future. The objective is to demonstrate the technical and economic benefit of thermocline storage systems, and to conclude whether latent heat storage is more advantageous than sensible heat storage systems. These objectives will be fulfilled by accomplishing the following goals:

1.) Construction and operation of an experimental packed bed sensible heat storage system that will enable validation of a numerical model. The model allows for an in-depth analysis of system performance and cost. Though the conventional 2-tank design is a sensible heat storage system, use of the acronym “SHS” throughout the remainder of the study specifically refers to sensible heat packed bed thermocline systems.

2.) Development of a packed bed LHS model that will be employed for a detailed study of the dynamics and trade-offs of using phase change materials (PCMs). Hypothetical and real PCMs are evaluated. A comparative analysis between single PCM, multiple PCMs, and sensible heat storage systems with realistic storage media will be conducted.

3.) Establishment of the economic benefits and weaknesses of all three storage system types, i.e. single PCM, multiple PCMs, and SHS, over the state-of-the-art 2-tank system.

1.2 Background

The HTF that is to be used in the solar field and hence the packed bed storage system is dictated by the CSP technology in place. These potential HTFs include air, molten salt, synthetic oil, and steam. The interaction between the HTF and storage media can be studied from different levels. For a component level assessment, the focus can pertain to material selection, compatibility between the storage material, containment material and HTF, and heat transfer enhancement mechanisms that improve the rate of energy exchange between the HTF and storage media. From a system level perspective, studies include investigations on controls for charging and discharging of the HTF, costs, performance evaluation, as well as system behavior and losses. Since the motivation for this work is to evaluate the economics and performance of CSP storage from a systems level perspective, the following discussion provides a review on system studies of high temperature sensible heat and latent heat storage.

1.2.1 Sensible Heat Storage

In sensible heat packed bed storage systems, the HTF is typically in direct contact with the storage media. This rather simple storage strategy does not require HTF piping or encapsulation techniques, thus minimizing extraneous costs. There are several aspects from which these systems are evaluated. From a thermo-mechanical perspective, it is important to assess the relative thermal expansion between the storage media and the tank to prevent thermal ratcheting. Cyclability, chemical and thermal stability, and chemical compatibility must also be evaluated to ensure that the materials need not be replaced during the expected lifetime of the plant, typically over 10,000 heating/cooling cycles for a 30-

year plant life [6]. Parametric studies are often conducted to determine how various factors affect system performance. Examples of such factors include mass flow rate, thermophysical properties, tank height-to-diameter ratio, and particle diameter.

A numerical or analytical model is needed in the analysis of storage systems, particularly to understand performance and behavior, and to design large scale systems. Experimental prototypes are constructed to validate these numerical models and are therefore critical in ensuring that the model is able to capture the physics of the system and incorporates appropriate assumptions. To date, several experimental packed beds have been constructed and tested on a laboratory scale. One of the main reported drawbacks of construction on this scale is related to the "wall effect" phenomenon, which stems from the interaction of the tank wall and the packed bed media. As depicted in Figure 3, a high porosity region develops at the confining wall and this higher void fraction can penetrate into the bed, resulting in inhomogeneous and unpredictable thermal and hydraulic behavior.

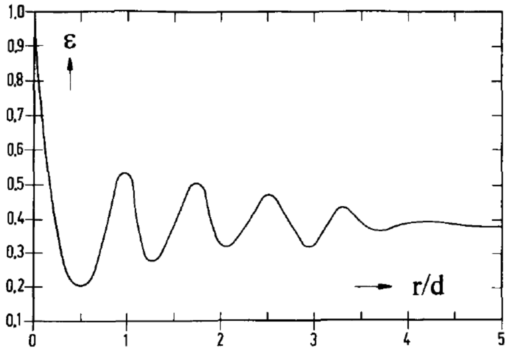

Figure 3. Radial void fraction distribution of a packed bed [7]. (Copyright permission in Appendix C).

Several authors have investigated how the phenomenon affects the pressure drop of a packed bed and it is generally concluded that the tank-to-particle diameter ratio (d/D_p) is the most profound factor [7-17], though many studies have conflicting conclusions on the exact ratio in which the wall effect comes into play. The phenomenon can either increase the local flow rate due to the increased porosity or it can reduce the local flow rate due to wall friction. Eisfeld and Schnitzlein [15] conducted a thorough investigation of more than 2300 experimental data points from previous studies and concluded that the these two counteracting effects are strongly contingent upon the particle Reynolds number [15]. For streamline flow, wall friction tends to dominate whereas with more turbulent flow and therefore a thinner boundary layer, the increased porosity has a more prominent role. Eisfeld and Schnitzlein also concluded that the tank-to-particle diameter ratio is only important when it is less than 10.

Understanding how a packed bed system behaves under varying parametric conditions has been the focus of several studies, and the performance of such systems has been quantified by indicators such as first and second law efficiencies as well as utilization ratios. These performance metrics are discussed in further detail in Chapter 3. Important to an analysis is also ensuring that the study incorporates realistic conditions that can be applied to real-world applications. In Hanchen et al. [18] for example, the performance results for a single charging/discharging cycle and for 20 consecutive charging/discharging cycles are provided. In doing so, the study demonstrated that the trends in performance between a single cycle and steady state can be divergent, revealing the importance of investigating a system under continuous cyclic operation. The need to evaluate a system under steady state conditions was corroborated by Bruch et al. [19] via experimental testing of a molten salt packed bed system that underwent multiple charge/discharge cycles.

When air is used as the HTF, pumping power requirements can be substantial. A commonly employed pressure drop correlation is the Ergun equation [20], Equation 1, which demonstrates the dependency of pressure drop on particle diameter, porosity, and flow rate.

$$\frac{\Delta P}{H} = 150\frac{(1-\varepsilon)^2}{\varepsilon^3}\frac{\mu_{HTF}U}{D_p^2} + 1.75\frac{1-\varepsilon}{\varepsilon^3}\frac{\rho_{HTF}U^2}{D_p} \tag{1}$$

The equation indicates that the pressure drop decreases as the particle diameter increases, thus a larger particle diameter would be ideal if the goal is to minimize the pumping requirement. The thermal performance improves however, when the particle diameter decreases. This is apparent when examining heat transfer correlations such as that provided by Wakao et al.[21] in Equation 2,

$$h = \frac{k_{HTF}}{D_p}\left[2 + 1.1Pr^{\frac{1}{3}}Re^{0.6}\right] = k_{HTF}[\frac{2}{D_p} + \frac{1.1}{D_p^{0.4}}\left(\frac{c_{p,HTF}\mu}{k_{HTF}}\right)^{\frac{1}{3}}\left(\frac{G}{\mu}\right)^{0.6}]. \tag{2}$$

Therefore an optimal particle diameter would balance the effects of pressure drop and heat transfer. In the parametric study conducted by Hanchen et al. [18], the steady state analysis demonstrated that pumping work increased significantly for small particle sizes, however this undesirable effect was counteracted by enhanced convective heat transfer. For the smallest particle diameter under study, i.e. D_p = 2 mm, the pumping work was the highest at approximately 2% of the energy supplied to the tank, yet it had the greatest overall efficiency due to the sharper temperature front, i.e. a narrower thermocline zone, which allows for more efficient extraction of energy.

The effect of particle diameter in the presence of other heat transfer fluids has also been evaluated, however pumping losses were neglected. Xu et al. [22] investigated the effect of particle diameter on a system that utilized molten salt as the HTF under discharging mode. They concluded that large particle diameters result in lower rates of heat transfer between the particle surface, center, and HTF, resulting in a thicker thermocline region and reduced discharging efficiency. The large particle diameter was 25 cm, which is unrealistic for packed bed systems however. Yang et al. [23] similarly studied the effect of particle diameter in the presence of molten salt as the HTF, yet under charging conditions only. They concluded that a particle with smaller diameter reduces the rate of entropy generation within the system, enhances charging efficiency, and produces a sharper thermocline zone. Neither of these studies investigated the performance of the system under cyclic conditions, nor did they consider overall system efficiencies.

Under the given conditions of a power plant, it is necessary to understand the rate at which charging and discharging occurs as well as utilization of the storage system. The thermal properties of the storage material can affect the dynamics of these processes and are thus an essential component to study. Aly and El-Sharkawy [24] investigated the charging process of a packed bed and demonstrated that increasing the thermal conductivity of the solid storage media increases the rate of heat transfer and energy stored inside the bed, but only to a certain time period. Initially the high rate of heat transfer quickly charges the system, eventually leading to a decrease in the temperature difference between solid and fluid. At a certain point in time, a low heat transfer rate starts to dominate and the temperature of the material with low thermal conductivity then starts to exceed that of the high thermal conductivity. Hanchen et al. [18] and Adebiyi et al. [25] evaluated the overall efficiency, i.e. charging and discharging, rather than just the charging process, and concluded that the solid media thermal conductivity has an insignificant influence on the performance of a system. Adebiyi et al. [25] attributed the minor difference in performance to the fact that intraparticle conduction was negligible, which is often the case with sensible heat storage systems due to the low Biot number.

Conduction within the individual solid and fluid phases does not account for all mechanisms of heat transfer within a packed bed. Other mechanisms include conduction between solid particles, film convection through the fluid layer in contact with the solid particles, and radiation between solid surfaces [26]. These additional means of heat transfer are often assimilated through the use of the effective thermal conductivity. Xu et al. [27] conducted a parametric study of the discharging process, comparing five different correlations for the effective thermal conductivity of fluid and solid phases found in the literature. The study showed that four of the correlations agreed well with each other, and the correlation that resulted in the highest values of effective thermal conductivity resulted in a slightly thicker, thus less ideal thermocline zone. This unfavorable effect is accredited to the fact that a higher effective thermal conductivity leads to enhanced thermal diffusion, causing the thermocline region to expand. They also evaluated the effect of changing the solid thermal conductivity to values that ranged from 0 W/m-K to 400 W/m-K and found that a higher thermal conductivity resulted in a wider temperature gradient, resulting in decreased discharging efficiency, i.e. increasing the thermal conductivity from 0 to 400 W/m-K led to efficiencies of 89.9% and 81.7%, respectively. They concluded that a low solid filler thermal conductivity is preferable for molten salt packed bed systems. The study did not evaluate the charging process nor did it mention conducting the study under steady state conditions.

The volumetric heat capacity was shown by Hanchen et al. [18] to have a stronger influence on packed bed systems than the solid thermal conductivity. The study evaluated the behavior of four materials with dissimilar volumetric heat capacities subjected to 6 hour charging and 6 hour discharging periods. The thermocline zone of the material with the largest volumetric heat capacity advanced more slowly down the bed than that of the three remaining materials, resulting in less energy stored. The overall efficiency was slightly higher for this material since the slower moving thermocline zone did not reach the bottom of the tank within the allotted charging time. This results in less energy being wasted during the charging process. If a system must charge and discharge within a certain amount of time, the volumetric heat capacity can thus influence the utilization of the system. In actual solar field operation however, the charging and discharging process is not necessarily defined by a specific time period, but by a maximum cut-off temperature during charging and a minimum cut-off temperature during discharging [5]. In this scenario, the thermocline zone would reach the bottom of the tank, however it would take significantly longer for a material with high volumetric heat capacity. Thus the charging and discharging periods are strongly affected by the volumetric heat capacity. This phenomenon can be explained by the concept of the propagation velocity of the thermocline zone, $v_{t,sens}$, which is defined as [28]

$$v_{t,sens} = \frac{C_{p,HTF,h}\rho_{HTF,h}U}{\varepsilon C_{p,HTF,h}\rho_{HTF,h}+(1-\varepsilon)C_{p,s,h}\rho_{s,h}} \tag{3}$$

and is dependent on the physical properties of the solid and fluid phases as well as the void fraction of the bed. If t_o is the charging or discharging period, then $v_{t,sens}\ t_o$ is the front propagation distance. This value characterizes the length that the thermocline zone travels during the specified time period and provides a measure of the tank height required for the discharge/charge process [29]. Ideally the height of the bed would be larger than $v_{t,sens}\ t_o$ in order to fully utilize the packed bed. If the height is less than $v_{t,sens}\ t_{o,}$ then the bed will be completely charged before the charging time period ends and will run out of thermal energy before the discharging period completes.

Aside from the physical properties of the filler material, the particle Reynolds number, defined as

$$Re = \frac{\rho_{HTF}UD_p}{\mu_{HTF}} = \frac{\dot{m}D_p}{A_{bed}\mu_{HTF}} \tag{4}$$

and hence mass flow rate, affect system performance. Equation 3 demonstrates that there is a concomitant increase in thermocline zone propagation velocity with an increase in superficial bed velocity. This indicates that for a high particle Reynolds number, a longer flow distance is needed to exchange the same amount of energy between HTF and storage material than that of a lower Reynolds number. Thus the temperature rise is more gradual for a high Reynolds number, which corresponds to an extended thermocline zone, potentially leading to a waste in thermal energy [28].

The packed bed porosity is another parameter that has been studied for its effect on system performance. Xu et al. [30] investigated the influence on discharging efficiency and thermocline thickness by varying the porosity of a packed bed system from 0.1 to 0.8. The resulting discharging efficiency increased with increasing porosity, however the growth was marginal over the large porosity range. The authors concluded that beyond a small porosity value (e.g. 0.22), its effect is insignificant on the development of the thermocline thickness. Since the HTF can be a costly component of the storage system, the porosity would ideally be kept at a low value to minimize the HTF volume requirement.

Aside from system level analyses, several authors have conducted studies that evaluate plant level performance when a thermocline packed bed storage system has been integrated. Typical solar field operation requires that charging terminates when the outlet HTF temperature reaches a maximum threshold temperature that is defined by the temperature limitations of the solar field [31]. Similarly, a minimum cut-off temperature is imposed during the discharging process in order to maintain reasonable turbine efficiencies and electrical power output by sustaining a high outlet HTF temperature from the storage system. Though packed bed systems have the advantage of a single tank requirement, the thermocline zone is confined to the tank if these two cut-off criteria are induced, thus rendering a portion of the bed unusable. Therefore it is beneficial to design a system with conditions that promote a narrow thermocline zone, i.e. a high rate of heat transfer, to extend the amount of energy that can be stored before the maximum charging cut-off temperature is reached.

During the discharging process, the HTF exits the bed at or near the hot charging inlet temperature, $T_{h,HTF}$, and subsequently decays before discharging ceases. This attenuation of HTF temperature has been shown to impact plant performance, yet to a degree that is acceptable. Kelly [32] evaluated the performance of a power plant operating with a supercritical Rankine cycle, wherein the inlet turbine steam temperature decreased from 650°C to 550°C as a result of the declining HTF temperature. The 100°C temperature drop resulted in a 14% decrease in cycle output and a 5% decline in cycle efficiency. These penalties occurred near the end of the discharge period and did not show a strong impact on annual plant performance. Flueckiger et al. [31] conducted a plant level study of a 100 MWe power tower plant with a 6 hour thermocline storage system. The simulation accounted for off-design conditions, which occurred when the HTF temperature deviated from the hot inlet charging temperature of 600°C to a minimum threshold value of 473°C. Under these conditions, the thermocline system increased the annual capacity factor of the plant from 27.3% to 53.1% and the solar-to-electric efficiency from 7.6% to 14.7%. Thus SHS systems appear to be a viable option for CSP systems from a plant performance perspective.

1.2.2 Latent Heat Storage

Several of the trends observed in SHS packed beds are shared with LHS systems. For instance, system efficiency is similarly enhanced as the particle diameter and inlet HTF velocity decrease [33, 34]. There are additional parameters that can strongly influence the performance and behavior of LHS systems however, and their effects mandate judicious selection in storage media.

The phase change temperature is one such parameter that has been extensively studied. Wu et al. [34] investigated the effect of solidification temperature on the discharging efficiency of a molten salt packed bed system. The single cycle analysis demonstrated that discharging efficiency increases significantly with increase in phase change temperature. Nithyanandam et al. [35] conducted an extensive parametric study on high temperature packed bed LHS systems. The study showed that the phase change temperature must correspond to a value that is either above the discharging cut-off temperature or below the charging cut-off temperature to maximize usage of the potential storage capacity. Flueckiger and

Garimella [5] evaluated the annual performance of a CSP plant with a SHS system and with a LHS system. The LHS system study investigated the effect of phase change temperature on the plant's annual capacity factor and thermal energy discard. The hypothetical PCM with a melting point that fell between the charging and discharging cut-off temperature showed a significant reduction in annual capacity factor, thus corroborating the results of the aforementioned study that the phase change temperature must lie outside of the threshold window.

The latent heat, *L*, is often investigated in its non-dimensional form as the Inverse Stefan number, defined as

$$InvSte = \frac{L}{Cp(T_{h,HTF} - T_{c,HTF})} \tag{5}$$

where $T_{h,HTF}$ and $T_{c,HTF}$ are the charging inlet temperature and discharging inlet temperature, respectively. In the study by Nithyanandam et al. [35], an analysis on the effect of Inverse Stefan number showed that the system's ability to use its potential storage capacity increased with decreasing latent heat. Though its ability to store more energy increased, the useful energy discharged from the system did not show the same trend. Rather, the useful discharged energy slightly increased with increasing latent heat until a certain point, after which the useful energy plateaued.

The influence of latent heat and phase change temperature on the behavior and hence output of a TES system is largely related to the relative velocities of the sensible heat thermocline front, defined by Equation 3, and the phase change front. The velocity of the phase change front during the charging process is defined in Fleuckiger and Garimella [5] as

$$v_{latent,ch} = \frac{C_{p,HTF,h}\rho_{HTF,h}U}{\varepsilon C_{p,HTF,h}\rho_{HTF,h} + (1-\varepsilon)C_{p,s,h}\rho_{s,h}[1 + \frac{1}{Ste}\left(\frac{T_{h,HTF} - T_{c,HTF}}{T_{h,HTF} - T_{solidus,PCM}}\right)]} \tag{6}$$

and for the discharging process as

$$v_{latent,dch} = \frac{C_{p,HTF,h}\rho_{HTF,h}U}{\varepsilon C_{p,HTF,h}\rho_{HTF,h} + (1-\varepsilon)C_{p,s,h}\rho_{s,h}[1 + \frac{1}{Ste}\left(\frac{T_{h,HTF} - T_{c,HTF}}{T_{liquidus,PCM} - T_{c,HTF}}\right)]} . \tag{7}$$

Equations 6 and 7 reveal the dependence of the phase change front travel rate on the latent heat and phase change temperature. With an increase in the latent heat of fusion or a decrease in the difference between the incoming hot HTF temperature and solidus temperature, the travel rate of the phase change front during charging mode slows. Figure 4 illustrates the architecture of a LHS packed bed system during the charging process. The PCM melt temperature is 515°C, and $T_{h,HTF}$ and $T_{c,HTF}$ are 565°C and 288°C, respectively. The sub-solidus sensible heat thermocline region travels at a rate that is governed by Equation 3 while the movement of the phase change zone is subjected to the slower velocity defined by Equation 6. The hot zone is restricted by the movement of the phase change front, therefore it does not advance deep into the bed. A comparison of the top and bottom figures demonstrates the relative movement of each zone over time. As charging terminated, the sub-solidus sensible heat zone reached the bottom of the bed, the phase change front lengthened, and the hot zone only slightly expanded. Had a lower melting PCM been employed, the phase change front and hot zone would have advanced at a rate that was closer to that of the sub-solidus sensible heat zone. All three zones would have shifted further down the bed to a similar degree and a larger portion of the potential storage capacity would have been exploited by the time the saturation condition was met.

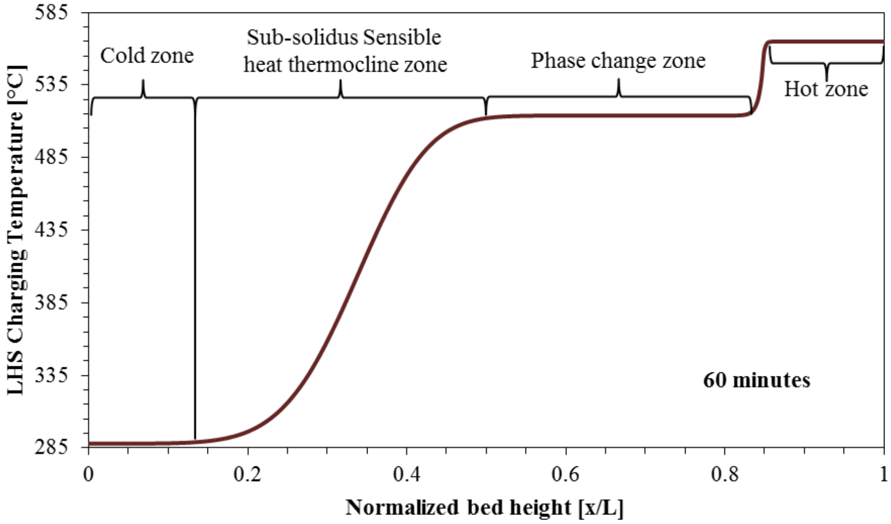

Figure 4. Progression of the zones of a packed bed latent heat storage system during the charging process.

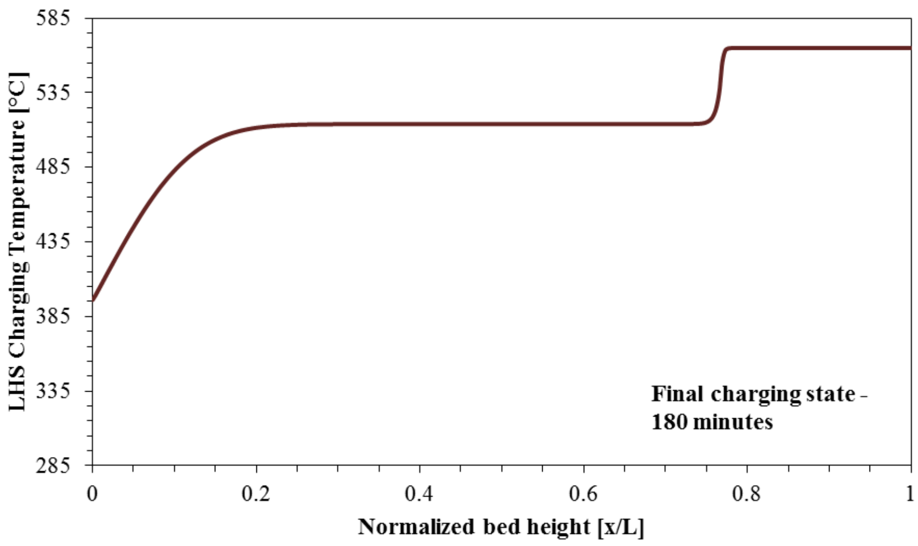

Figure 4 (continued)

Alternatively, a PCM of higher phase change temperature is an advantage during the discharging process. This induces a faster phase change front velocity that more closely coincides with the sub-sensible heat thermocline zone travel rate. The HTF exits the bed at the phase change temperature for an extended period of time and this elevated temperature is more thermodynamically favorable than a PCM of lower solidification temperature. Thus LHS systems are plagued by conflicting effects that simultaneously inhibit both maximum storage and maximum utilization of the stored energy.

1.2.3 Comparative Studies of SHS and LHS Packed Bed Systems

Several studies have parametrically evaluated the dynamic thermal behavior and performance of medium to high temperature LHS and SHS packed bed storage systems individually, yet few make a direct comparison of both systems. As previously mentioned, Flueckiger and Garimella [5] conducted a plant level study that evaluated and compared the annual performance of both SHS and LHS systems with a single PCM and cascaded PCMs. The investigation concluded that a single PCM does not demonstrate enhanced annual plant output, however the use of multiple PCMs with carefully selected melting points does show some improvement over SHS systems. The characteristics of the systems in the analysis were based on those of the packed bed system in Pacheco et al. [36]. A hypothetical PCM with the same thermal properties as the SHS filler material was used in the study in order to provide an objective assessment of the storage capacity added by the phase change process.

An exergy analysis was conducted in Bindra et al. [4] and used to compare the overall exergetic efficiency of LHS and SHS systems of constant tank size and velocity. Important in maximizing the storage and recovery of exergy from a system is the development of a steep temperature gradient within the thermocline zone. As both axial dispersion and intra-particle diffusion influence the expansion of the thermal gradient, the study demonstrated that the exergy efficiency of SHS systems can be increased by minimizing axial dispersion and increasing intra-particle diffusion. For LHS systems, the study focused on the impact of the latent heat and phase change temperature of PCMs since these two parameters have a stronger influence on performance than axial dispersion and intra-particle diffusion. For lower values of the latent heat of fusion, a narrower thermocline zone is produced, resulting in less exergy destruction and hence higher exergetic efficiencies. The same trend applies to the phase transition temperature, wherein this value should be low with respect to the inlet charging temperature for a steeper temperature gradient, but only to an optimal value, below which the exergy efficiency decreases. The authors concluded that high temperature sensible heat storage systems can provide higher energy density and higher exergy recovery than latent heat storage systems.

In Adebiyi [37], a high temperature SHS system was compared to single-PCM LHS systems of varying latent heat and phase change temperature. For the same size tank, the LHS enhanced the storage capacity, however a comparison of the overall first and second-law efficiencies revealed that the LHS system was not always thermodynamically superior to the SHS system. The enhancement in performance was largely a function of the phase change temperature and latent heat as well as the inlet temperature of the HTF. The first-law analysis alone was not sufficient to come to these conclusions, therefore the second-law efficiency was a better indicator of performance.

The following study employs the second-law efficiency to evaluate overall system performance. It also adopts the capacity ratio and utilization ratio to understand the extent to which the potential storage capacity of the sensible heat and latent heat media is exploited. These two ratios isolate the influence of the storage media on system output from the additional storage capacity that is possessed by the HTF. Hypothetical LHS systems are analyzed and compared to systems that may be realistically encountered to understand how their performance and output may deviate. Chapter 2 discusses the experimental test beds and numerical model, chapter 3 evaluates system performance, and the study concludes with an economic assessment in chapter 4.

CHAPTER 2: EXPERIMENTAL SYSTEM AND MODEL VALIDATION

2.1 Introduction

In order to evaluate the performance and economics of both SHS and LHS systems, a thermal performance model was developed and validated with the aid of experimental data from laboratory-scale systems that were constructed in USF's Clean Energy Research Center (CERC) facility. The SHS packed bed system was initially constructed as a joint effort with SunBorne Energy Inc. to develop a low-cost storage solution for central receiver CSP plants that employ air as the HTF. The LHS packed bed system and PCM pellets were fabricated by CERC student Tanvir Alam, and were funded through E·ON SE as an initiative to develop an economically feasible storage technology for medium temperature CSP plants. The following sections expound upon the elements of both experiments as well as the validated model.

2.2 General Packed Bed Model

In order to calculate the transient temperature distribution of HTF and storage media within the packed bed system, the Dispersion-Concentric (DC) model was employed. This model is based on the assumption that the fluid exhibits dispersed plug flow and that intraparticle radially concentric conduction occurs in the solid phase [21]. To simplify the analysis and minimize computational time, it is assumed that the solid particles are identical and isotropic, and the bed porosity is uniform, implying that the HTF temperature and velocity are homogeneously distributed among the storage medium. Thus the system can be modeled as a one-dimensional domain, which is shown as an acceptable assertion based on the

---

[1] Portions of this chapter were published in Energy Procedia [94]. Copyright permission is included in Appendix C.

validation results. With this underlying assumption, the energy equation must only be solved for a single sphere at each axial position of the tank bed, given that its temperature profile represents that of all other spheres at the same axial location. Each sphere is modeled as axisymmetric and discretized into equally spaced radial nodes as illustrated in Figure 5.

Heat losses from the top and bottom of the tank were neglected and it was assumed that the HTF is the only medium that exchanges energy with the environment through the tank wall. This heat loss is accounted for with an overall heat transfer coefficient, U_w. In Jalalzadeh-Azar et al. [38] the role of radiation in a high temperature packed bed with inlet HTF temperature of 900 °C was shown to be insignificant, thus radiation between particle and HTF was also ignored in the current model.

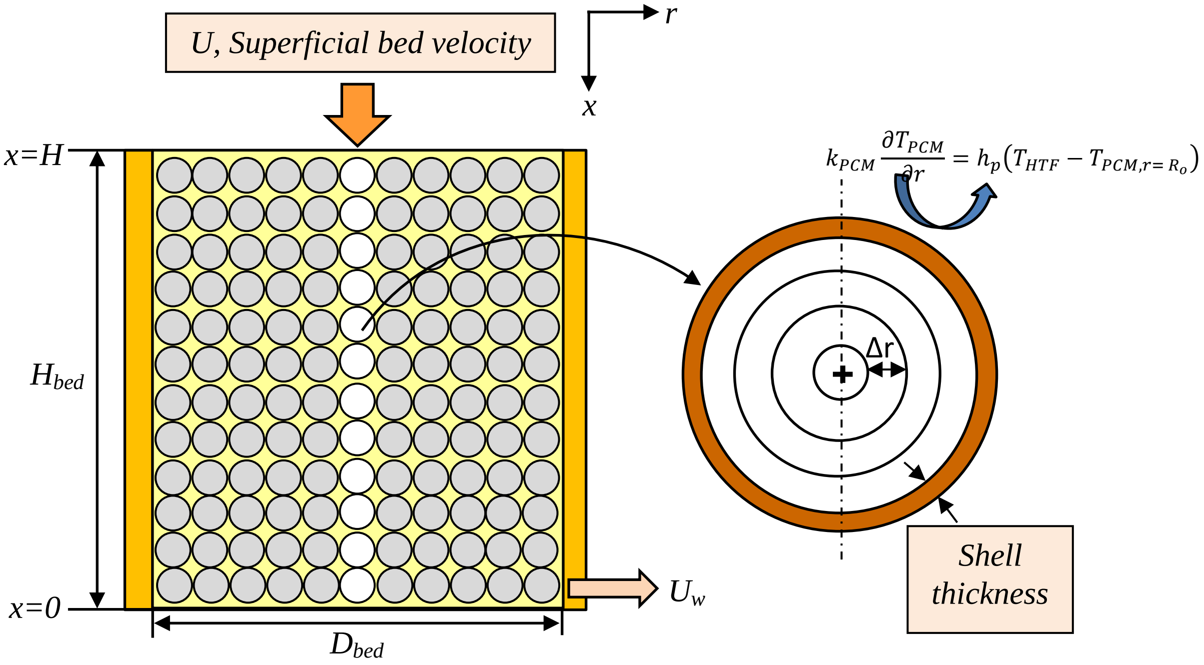

Figure 5. Schematic of the Dispersion-Concentric model numerical domain. Equation 8 determines the fluid temperature in the global domain on the left side of the figure. Equation 9 determines the solid temperature in the local domain of the sphere on the right side of the figure. Δr represents the distance between radial nodes within each sphere. The boundary condition of Equation 12 couples the two domains.

In adopting the above assumptions, the governing energy equations for the fluid and solid phases are defined respectively as

$$\frac{\partial T_{HTF}}{\partial t} = \alpha_{ax}\frac{\partial^2 T_{HTF}}{\partial x^2} - \frac{U}{\varepsilon}\frac{\partial T_{HTF}}{\partial x} - \frac{h_v}{C_{p,HTF}\rho_{HTF}\varepsilon}\left(T_{S,Ro} - T_{HTF}\right) - \frac{U_w D\pi}{C_{p,HTF}\rho_{HTF}\varepsilon A_{bed}}\left(T_{inf} - T_{HTF}\right) \quad (8)$$

and

$$\frac{\partial T_S}{\partial t} = \frac{k_S}{\rho_S C_{p,S}}\left(\frac{\partial^2 T_S}{\partial r^2} + \frac{2}{r}\frac{\partial T_S}{\partial r}\right)\ . \quad (9)$$

For intermediate and high flow rates, the second derivative $\frac{\partial^2 T_{HTF}}{\partial x^2}$ can be small as compared to the other terms in Equation 8 when the Peclet number is high, resulting in low thermal diffusivity. The first term on the right hand side of Equation 8 could therefore be neglected [21, 39] though it was retained in the analysis to accommodate the wide range of Reynolds numbers that are used in the study. The proposed criterion for neglecting axial dispersion was provided in [37] as

$$Pe = \frac{\rho_f U D_p}{\mu_f} Pr_f > 50. \quad (10)$$

The boundary conditions for the solid phase are defined as

$$\frac{\partial T_S}{\partial r} = 0, at\ r = 0 \quad (11)$$

$$k_S\frac{\partial T_S}{\partial r} = h_p\left(T_{HTF} - T_{S,r=R_o}\right), at\ r = R_o \quad (12)$$

and for the fluid phase as:

$$\frac{\partial T_{HTF}}{\partial x} = 0, at\ x = 0 \quad (13)$$

$$T_{HTF} = T_{in}, at\ x = H. \quad (14)$$

To couple the fluid and solid phases thus capturing the exchange of energy between a single sphere and the heat transfer fluid, an empirical equation for the particle convective heat transfer coefficient developed by Wakao et al. [40] was applied:

$$h_p = \frac{k_{PCM} Nu}{D_p} = \frac{k_{PCM}}{D_p}\left(2 + 1.1\left(Re^{0.6} Pr^{\frac{1}{3}}\right)\right). \quad (15)$$

The correlation is valid in the range of Reynolds number from 15 to 8500. Although the correlation is based on several experiments conducted with Prandtl numbers less than unity, the equation has proven valid with molten salts which bear larger Prandtl numbers.

To determine the volumetric heat transfer coefficient, h_v, the particle heat transfer coefficient is multiplied by the specific surface area of the bed, a_p. For spheres, this is defined by the following expression [38]

$$h_v = a_p h_p = \frac{6(1-\varepsilon)}{D_p} h_p. \tag{16}$$

To estimate the heat lost from the system to the ambient, an overall heat transfer coefficient is defined in terms of the resistances due to convection between HTF and the tank wall, conduction within the tank wall, and conduction within the insulation [18, 41]

$$\frac{1}{U_w} = \frac{1}{h_i} + r_{bed} \sum_{j=1}^{n} \frac{1}{k_j} \ln\left(\frac{r_{j+1}}{r_j}\right) \tag{17}$$

where $j = 1$ represents the inner tank wall, ($r_1 = r_{bed}$), and $j = 3$ represents the outer layer of insulation ($r_3 = r_{outer}$). The inner wall heat loss coefficient, h_i, is provided by Beek [42] as

$$h_i = \frac{k_{HTF}}{D_p}\left(\left(0.203 Re^{1/3} Pr^{1/3}\right) + \left(0.220 Re^{0.8} Pr^{0.4}\right)\right). \tag{18}$$

Heat transfer due to natural convection at the outer wall was neglected.

The assumption of a radially concentric temperature profile is physically impractical as heat conduction would not occur across the particle [21]. To account for this limitation, solid phase heat conduction is superficially included in the fluid thermal dispersion term, α_{ax}, of Equation 8 through an effective thermal conductivity [21]. Solid phase conduction is but one phenomenon that contributes to thermal dispersion of the fluid phase and the effective thermal conductivity, k_{eff}, compensates for all mechanisms. The effective conductivity is often defined in terms of the thermal properties of the individual phases as well as the geometry of the bed, and it includes two contributions: the stagnant fluid conductivity, and conductivity due to macroscopic flow effects [7]. The stagnant fluid effects correspond to the heat transfer mechanisms as mentioned in Chapter 1, including conduction through the fluid phase, axial conduction through the solid, conduction through contact points, and radiation between solid surfaces [7, 26]. The macroscopic effects that contribute to thermal dispersion are associated with the behavior of the flow and are related to the Peclet number, which is the ratio of the rate of advection to the rate of thermal diffusion of the flow. For the packed bed model, the effective thermal conductivity of the fluid phase was based on a correlation discussed in Gonzo [31, 43] as

$$k_{eff} = k_{HTF}\left[\frac{1+2\beta\phi+(2\beta^3-0.1\beta)\phi^2+\phi^3 0.05\exp(4.5\beta)}{1-\beta\phi}\right] \tag{19}$$

where $\varphi = 1 - \varepsilon$ and $\beta = (k_{PCM} - k_{HTF})/(k_{PCM} + 2k_{HTF})$.

The governing equations were solved in Matlab using direct finite difference approximation under the fully implicit scheme with *Nx* nodes in the axial direction and *Rx* nodes within each sphere. First order upwind scheme was used to discretize the temporal and advective term in Equation 8, while second order central differencing was used to discretize the diffusion term:

$$\frac{T_{HTF}{}_n^{i+1}-T_{HTF}{}_n^{i}}{\Delta t} = \alpha_{ax}\frac{T_{HTF}{}_{n+1}^{i+1}-2T_{HTF}{}_n^{i+1}+T_{HTF}{}_{n-1}^{i+1}}{\Delta x^2} - \frac{U}{\varepsilon}\frac{T_{HTF}{}_n^{i+1}-T_{HTF}{}_{n-1}^{i+1}}{\Delta x} - \frac{h_v}{C_{p,HTF}\rho_{HTF}\varepsilon}\left(T_{S,Ro}{}_n^{i} - T_{HTF}{}_n^{i+1}\right) - \frac{U_w D\pi}{C_{p,HTF}\rho_{HTF}\varepsilon A_{bed}}\left(T_{inf} - T_{HTF}{}_n^{i+1}\right) \tag{20}$$

The above equation was applied to nodes *2* through *(Nx-1)*. The first fluid boundary condition, Equation 13, was applied to node *Nx* via the following discretization by setting *(Nx-1) = (Nx+1):*

$$\frac{T_{HTF}{}_{Nx}^{i+1}-T_{HTF}{}_{Nx}^{i}}{\Delta t} = \alpha_{ax}\frac{2T_{HTF}{}_{Nx-1}^{i+1}-2T_{HTF}{}_{Nx}^{i+1}}{\Delta x^2} - \frac{U}{\varepsilon}\frac{T_{HTF}{}_{Nx}^{i+1}-T_{HTF}{}_{Nx-1}^{i+1}}{\Delta x} - \frac{h_v}{C_{p,HTF}\rho_{HTF}\varepsilon}\left(T_{S,Ro}{}_n^{i} - T_{HTF}{}_{Nx}^{i+1}\right) - \frac{U_w D\pi}{C_{p,HTF}\rho_{HTF}\varepsilon A_{bed}}\left(T_{inf} - T_{HTF}{}_{Nx}^{i+1}\right). \tag{21}$$

The solid equation, Equation 9, was discretized as follows

$$\frac{T_S{}_r^{i+1}-T_S{}_r^{i}}{\Delta t} = \frac{k_S}{\rho_S C_{p,S}}\left(\frac{T_S{}_{r+1}^{i+1}-2T_S{}_r^{i+1}+T_S{}_{r-1}^{i+1}}{\Delta r^2} + \frac{2}{r}\frac{T_S{}_{r-1}^{i+1}-T_S{}_{r+1}^{i+1}}{2\Delta r}\right) \tag{22}$$

and was applied to nodes *2* through *(Rx-1)*. The first boundary condition of the solid, Equation 11, was applied to the center of the sphere at *Rx* by employing L'Hôpital's rule [44]:

$$\frac{2}{r}\frac{\partial T}{\partial r}_{r=0} = 2\,\frac{\frac{\partial}{\partial r}\left(\frac{\partial T}{\partial r}\right)}{\frac{\partial}{\partial r}(r)} = 2\,\frac{\partial^2 T}{\partial r^2}\,. \tag{23}$$

Therefore the energy equation applied to the center of the sphere, at $r = Rx$ is

$$\frac{\partial T_S}{\partial t} = \frac{3k_S}{\rho_S C_{p,S}}\left(\frac{\partial^2 T_S}{\partial r^2}\right). \tag{24}$$

At the center node, *(r+1) = (r-1)*, therefore the resulting discretization is

$$\frac{{T_S}_{Rx}^{i+1}-{T_S}_{Rx}^{i}}{\Delta t} = \frac{6k_S}{\rho_S C_{p,S}}\left(\frac{{T_S}_{Rx-1}^{i+1}-{T_S}_{Rx}^{i+1}}{\Delta r^2}\right). \tag{25}$$

The second boundary condition of the sphere, Equation 12, applies to the surface of the sphere:

$$k_s \frac{{T_S}_1^{i+1}-{T_S}_2^{i+1}}{\Delta r} = h_p({T_{HTF}}_n^{i+1} - {T_S}_1^{i+1}). \tag{26}$$

The simulation is designed to calculate the axial temperature profile and quantity of energy stored within the filler material and HTF. Using this data, the net energy and exergy in and out of the system, first and second law efficiencies, and utilization factors are also determined.

2.2.1 Latent Heat Storage Packed Bed Model

The Dispersion-Concentric model can be used to simulate both LHS and SHS packed bed systems. Similar to the SHS model, the LHS model predicts the temperature profile of HTF and spherically shaped storage media, however the phase change process must be integrated. The nonlinear nature of the phase change phenomenon increases the complexity of the problem due to the moving interface between solid and liquid phases. For instance, a one-dimensional semi-infinite solidification problem with a single phase change temperature exhibits two distinct domains separated by the solid-liquid interface, as depicted in Figure 6. Within each respective domain, the solution of the solid temperature, T_s, and liquid temperature, T_L, must be calculated according to the following governing energy equations, assuming constant properties [45]:

$$\frac{\partial^2 T_s(x,t)}{\partial x^2} = \frac{1}{\alpha_s}\frac{\partial T_s(x,t)}{\partial x} \quad in\ 0 < x < s(t),\ \ t > 0 \tag{27}$$

$$\frac{\partial^2 T_L(x,t)}{\partial x^2} = \frac{1}{\alpha_s}\frac{\partial T_L(x,t)}{\partial x} \quad in\ s(t) < x < \infty,\ t > 0 \tag{28}$$

The solution mandates the use of a moving boundary condition, known as the Stefan condition, which serves in determining the location of the solid front, *s(t)*:

$$k_s \frac{\partial T_s}{\partial x} - k_L \frac{\partial T_L}{\partial x} = \rho L \frac{\partial T_L(x,t)}{\partial x} \quad at\ x = s(t),\ \ t > 0 \tag{29}$$

where L is the latent heat of solidification in J/kg.

Equation 29 describes the energy balance at the interface, wherein the difference in heat flux across the two domains is equivalent to the energy liberated due to the interface displacement per unit area per unit time [45, 46]. Exact solutions are limited in scope to semi-infinite problems with constant thermal properties in each phase as well as constant initial and imposed temperatures [46]. Though analytical solutions are not as restricted in nature, they are trumped by the ease and broad scope of numerical approximations, which can accommodate complex physical factors such as nucleation, variation in phase-change temperature, or multiple phase change fronts.

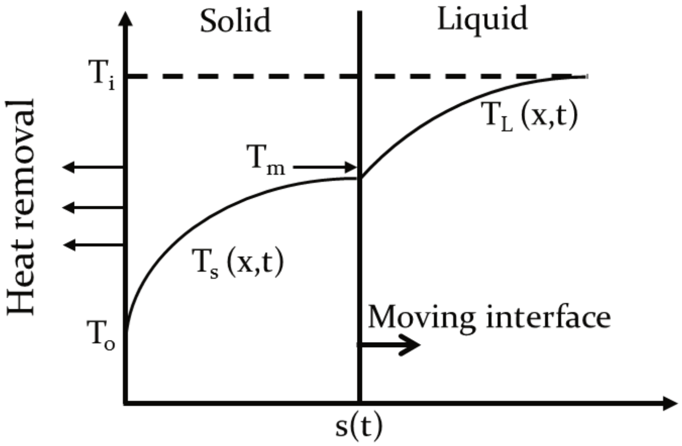

Figure 6. One-dimensional solidification. T_i represents the initial liquid temperature and T_o represents the boundary surface. Adapted from [45].

Several numerical algorithms are practiced in the literature and can be classified as either front tracking methods or fixed domain methods [47]. Front tracking methods rely on techniques that continuously locate the moving interface. This can be enacted through a deforming mesh which ensures that the front always lies on a node point. The moving interface can also be located with fixed mesh methods, in which interpolation is used to estimate the location of the front, or the time step can be varied to ensure that the interface falls on a node [45].

Alternatively, in fixed domain methods the governing energy equation can be applied to the entire domain and there is no need to apply the Stefan condition, thus the interface location is a by-product of the solution rather than a requirement [48]. Several fixed domain methods are available including

Enthalpy based formulations, the Apparent heat capacity method, Fictitious heat flow, and the Freezing index method [48]. To account for the phase change process within the PCM capsules in the current study, the Apparent heat capacity method was employed. This technique is advantageous in that it does not require modification of the Dispersion-Concentric energy equations. It simply captures the storage and release of latent heat by augmenting the heat capacity over a temperature range. The value of the apparent, or effective, heat capacity depends on the method or function used to characterize the shape of the apparent heat capacity curve. Differential scanning calorimetry (DSC) is one method that can be used to derive an apparent heat capacity function. The measured heat flow data of a sample during melting and solidification can be equated to an apparent heat capacity via the following equation:

$$c_{p,app}(T) = \frac{q(T)}{mass_{PCM}\theta} + c_{p,solid} \tag{30}$$

where *q(t)* is the heat flow of the sample obtained from the DSC, and *θ* is the ramping rate. Though this approach is valuable in providing data that is true to the material, it has been demonstrated by Arkar and Medved [49] that its accuracy in predicting the charging and discharging temperatures of a system is largely dependent on the heating rate, *θ*. This imposes a difficulty for measurements involving high melting temperature salts that exhibit high vapor pressure and therefore cannot undergo low heating rates due to evaporation of the sample. If the heat flow data are not readily available, the apparent heat capacity curve can be approximated by one of numerous equations that are found in the literature. Several of these equations are provided in Table 1.

In Alisetti and Roy [50], four different apparent heat capacity equations, Equations 31-33 and 36, were employed to simulate melting in a PCM slurry. The authors found that the greatest deviation between each of the four functions was no more than 4% and concluded that the melting point and melting temperature range was critical to modeling, rather than the shape of the curve. The results were not compared to experimental values due to limited availability of data and there was no discussion on the extent to which the melting temperature range impacted the results.

Table 1. Apparent heat capacity functions.

Equation	*Equation Title*	*Eqn #*	*Ref.*
$Cp_{app} = Cp_s + [2\left(\frac{L}{\Delta T^2} - \frac{Cp_s}{\Delta T}\right)](T - T_s)$	Right triangle	(31)	[50]
$Cp_{app} = Cp_s + [2\left(-\frac{L}{\Delta T^2} + \frac{Cp_s}{\Delta T}\right)](T - T_L)$	Left triangle	(32)	[50]
$Cp_{app} = Cp_s + \left[\left(\frac{\pi}{2}\right)\left(\frac{L}{\Delta T^2} - Cp_s\right)\right] sin\pi[\frac{T - T_S}{\Delta T}]$	Sine curve	(33)	[50]
$Cp_{app} = Cp_s + ae^{-0.5(\frac{T - T_{melt}}{b})^2}$	Gaussian	(34)	[51-53]
$Cp_{app} = Cp_s + (Cp_L - Cp_s) \cdot \frac{1}{1 + e^{-\alpha(T - T_L)}} + \frac{L\alpha}{e^{-\alpha(T - T_L)} + e^{\alpha(T - T_L)} + 2}$	Logistic Function	(35)	[54]
$Cp_{app} = \frac{Cp_s + Cp_L}{2} + \frac{L}{T_L - T_s}$	Rectangular	(36)	[55, 56]

In Lamberg et al. [51], the rectangular function, Equation 36, was used to calculate the apparent heat capacity of paraffin wax during melting and solidification in a rectangular container with and without fins. Two temperature ranges were induced for estimation of the function, one based on a 2°C range, and the other based on a 7°C range. Cooling and heating DSC curves with a ramping rate of 2°C/min were additionally employed to model the PCM with the enthalpy method. The study found that the results were similar between all three simulation methods, however the apparent heat capacity method with the narrow phase change range produced the most precise results when compared to experimental data.

Based on these previous studies, it can be ascertained that the shape of the apparent heat capacity function need not be emphasized, and that the phase change temperature and latent heat play a greater role in influencing the results. In order to validate this assumption for salts with higher phase transition temperature and to determine the most appropriate apparent heat capacity function for use in the model, three functions were employed: a DSC curve, the logistic function, and the rectangular function. The DSC curve was also used to evaluate the melting point and latent heat of the PCM. The measured HTF temperature of a laboratory-scale prototype LHS system, as discussed in Section 2.3.2, was used to validate the LHS model and evaluate each of the three apparent heat capacity functions.

2.3 Model Validation

2.3.1 Sensible Heat Storage Model Validation

2.3.1.1 SHS Pilot-Scale System Design and Construction

In order to validate the numerical model and explore the use of a low-cost SHS media proposed by SunBorne Energy, Inc., a 36 kWh_{th} packed bed system was designed and constructed. This storage capacity is based on an operating temperature range between ambient and 500°C. The filler media consists of crushed hematite, a mineral ore that was mined by the Minnesota Department of Natural Resources and purchased from Midland Research Center. As an unprocessed ore, the material ranged in composition from high grade to low grade hematite and included fine-grained silica as well as small amounts of iron oxides and iron hydroxides. Nominally sized 2 inch (50.8 mm) particles were selected for the packed bed experiment. In order to minimize the wall effect by meeting the tank-to-particle diameter ratio criteria of 10 as specified in [15], a bed diameter of 28 inches (0.610 m) was initially chosen. The tank height was selected as 48 inches (1.219 m). A schematic of the final design is presented in Figure 7 and the system components are provided in Table 2.

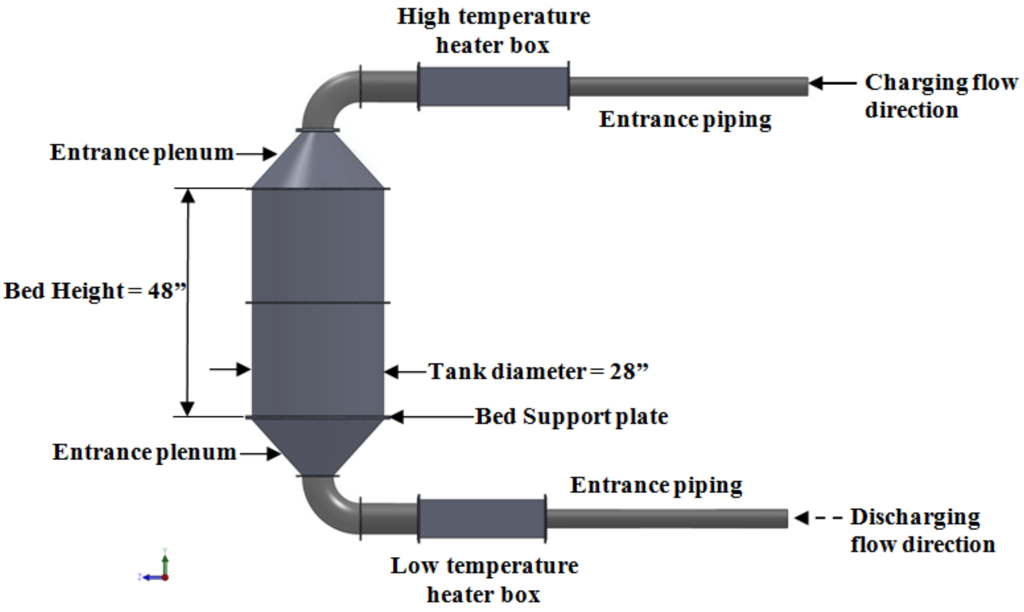

Figure 7. Prototype SHS packed bed system design.

Due to restrictions in the availability of storage media, the final bed diameter and height were limited to 0.445 m and 0.889 m, respectively. A flexible ceramic wool insulation was used to line the inside of the tank and compensate for the difference in tank diameter and bed diameter. The resulting insulation thickness was 5.25 inches (0.133 m) on the inside of the tank and an additional 2 inches (50.8 mm) lined the outside. The tank was divided into two 24 inch high flanged sections in order to facilitate ore placement and removal. Two 12 inch tall conical entrance plenums were placed above and below the bed to aid in transitioning from the large tank diameter to the smaller entrance piping diameter. In order to simulate both charging and discharging mode of a high temperature system, two stainless steel heater boxes were installed at the top and bottom of the system. A 9.53 mm thick perforated carbon steel plate with 12.7 mm diameter holes and 48% open area was used to support the pellets. The packed bed support plate was designed by first assuming a 60 degree staggered pattern, which is one of the strongest configurations of perforated plates. The maximum allowable bending stress of carbon steel at 400°C [52] was multiplied by a perforated plate modified strength coefficient in order to calculate the plate's thickness [53]. The strength coefficient was based on a ½ inch hole diameter and 11/16th inch pitch, which results in an open area of 48%. Stainless steel wire mesh was placed on top of the plate to prevent small particles from falling into the lower plenum. The tank, plenums, and packed bed plate were coated with a high temperature paint to minimize corrosion.

Flow uniformity was a concern given that 90 degree elbows were placed immediately adjacent to the entrance plenums. As fluid enters an elbow, the centrifugal force that is generated at the bend induces a radial pressure gradient that distorts the flow [54, 55]. In order to simplify the analysis, the numerical model idealizes the flow as uniform across the bed entrance, therefore the experimental inlet conditions should theoretically mimic this situation in order to validate the model. Thus extensive entrance length would preferably be incorporated in order to allow the flow to straighten before entering the packed bed. Since the system was restricted in height by the building's infrastructure, the required entrance length could not be achieved and flow conditioners were constructed in an attempt to minimize the non-uniform nature of the flow. Several flow conditioner designs were tested on a small-scale experimental system including diffusers, tube bundles, and NEL conditioners. Figure 8 shows the final diffuser plate design that was installed in the pilot-scale system at the entrance to the lower plenum. This aided in redistributing the flow when air entered the system from below, however additional measures were needed for the upper plenum. The reason that the diffuser plate did not work for the top of the system is unknown, though the combined use of the perforated packed bed plate and diffuser plate may have synergistically minimized flow maldistribution at the bottom of the system. Though the flow was not uniform at the top bed entrance, an even flow distribution developed after the HTF penetrated further into the bed and the validation results were not heavily influenced by this effect. Further details of the flow conditioner design and experiments are provided in the appendix, section A.1.

Table 2. Experimental system components.

Component	*Description*
Entrance piping	4” diameter, 60” length, 10 gauge, carbon steel
Heater box	304 Stainless steel
Elbow/Bed piping	304 Stainless steel, 6” diameter
Flow conditioner	304 Stainless steel, 6” diameter, 3/8” thickness
Packed bed plate	3/8” thick carbon steel, ½” diameter holes, 11/16” pitch
Tank	1/8” thick carbon steel, 48” height
Entrance plenum	1/8” thick carbon steel, 6”x28” diameter
Averaging pitot tube	Omega Instruments FPT-6100 High accuracy pitot tube; accuracy = ±2% of rate, repeatability = ±0.1%.
Digital manometer	Dwyer Mark II, 0-1” W.C. range; accuracy = ±0.5% of F.S.
Thermocouples	Omega Instruments- XCIB, High temperature Inconel overbraided ceramic fiber insulated; accuracy is greater of 2.2°C or ± 0.75% of reading.
Blower	Dayton ¼ hp blower, model #1TDT4

Figure 8. Final flow conditioner design. The conditioner was implemented at the bottom of the entrance plenum at the discharging inlet in the prototype system.

Air and solid temperature were measured with k-type Omega thermocouples. The thermocouple wires were insulated with a flexible Inconel overbraid ceramic fiber to withstand the high system temperature. The thermocouples used for air temperature measurement were equipped with a perforated hood to protect the exposed beaded wire junction, which allowed them to be inserted within the voids of the bed in order to measure air temperature alone. Unshielded, exposed beaded wire junction thermocouples were placed inside a hole drilled to the center of the ore to measure the ore temperature. Figure 9 provides a thermocouple location schematic for the packed bed. There were 5 rows located down the vertical axis of the bed. Each of these five rows consisted of 5 equally-spaced thermocouples across the bed diameter to measure air temperature, and one centrally located thermocouple to monitor solid temperature. Five thermocouples were placed in a horizontal plane in a cross configuration in each of the upper and lower plenums to measure air temperature entering and exiting the bed. Data acquisition was carried out via Labview SignalExpress and temperature data was monitored and recorded every 60 seconds.

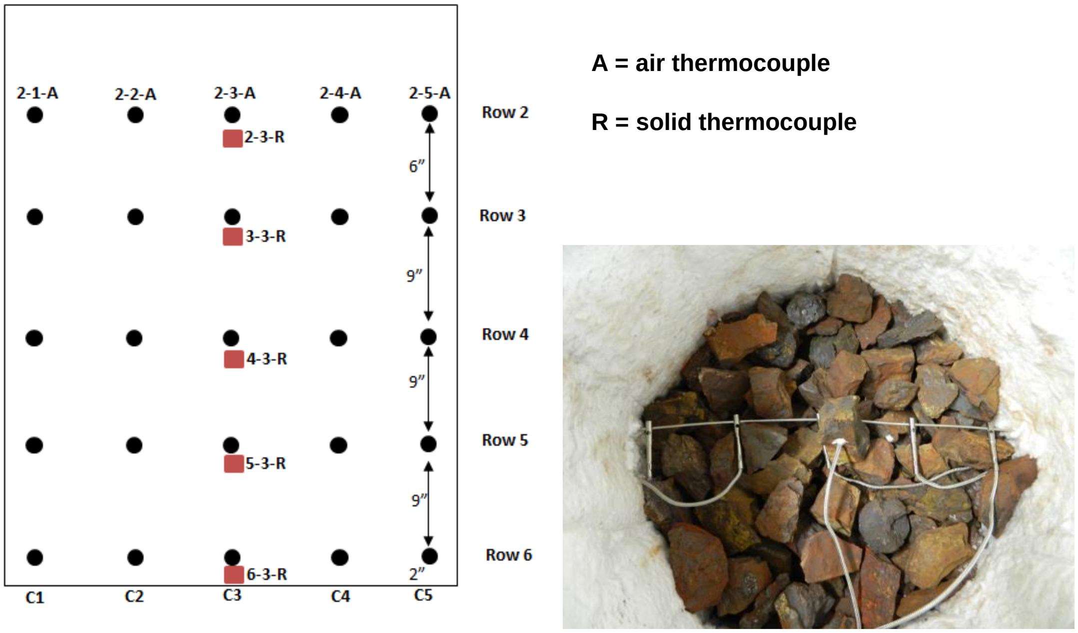

Figure 9. Schematic of thermocouple location within the packed bed and image of thermocouple placement in the experimental system. Though not depicted in the figure, the center air thermocouple is adjacent to the solid thermocouple.

A pressure tap was installed in each of the plenums and several taps spanned the height of the tank to measure the packed bed pressure drop, which was measured with a digital manometer. The same manometer was used in conjunction with an averaging pitot tube to measure the velocity in the entrance pipe before it entered the charging and discharging heaters. The entrance pipe's length was sized such that it met upstream and downstream length requirements of the pitot tube. In order to size the pitot tube and digital manometer, the system's total static pressure was first estimated by calculating the pressure drop across all system components as defined in [56]. The air entered the entrance pipe at room temperature, thus the density of ambient air and the pipe area were used to calculate the mass flow rate entering the system. Figure 10 provides the final system setup.

Figure 10. Completed pilot-scale packed bed storage system.

The system was operated under various mass flow rates, and charging and discharging inlet temperatures for the heat transfer experiments. The uncertainty in the experimental results was calculated by determining the systematic error and random error of four different experimental runs under the same operating conditions. The resulting uncertainty in experimental temperature was 4.6%. Before modeling the system, the characteristics of the particles and packed bed must first be defined. The following discussion illuminates the methodology in evaluating these parameters including sphericity, equivalent particle diameter, and porosity. It also entails an analysis on the pressure drop of the packed bed.

2.3.1.2 Pressure Drop Analysis and Determination of Packed Bed Parameters

Within packed bed systems, pressure drop pumping losses can be significant and must be known to appropriately size system pumps and blowers. Thus many studies focus on developing pressure drop correlations which are based on the key parameters that affect the transport properties of a system. These parameters can be optimally chosen such that they minimize pressure losses without compromising heat transfer and efficiency.

Of the various pressure drop correlations that have been presented, the Ergun equation, Equation 37, is one of the most widely adopted [20]:

$$\frac{\Delta P}{H} = A\frac{(1-\varepsilon)^2}{\varepsilon^3}\frac{\mu_{HTF}U}{D_p^2} + B\frac{1-\varepsilon}{\varepsilon^3}\frac{\rho_{HTF}U^2}{D_p} \tag{37}$$

where the coefficient *A* is 150 and *B* is 1.75.

In Ergun's seminal publication, previous theories and equations on pressure losses through packed beds were utilized in conjunction with experimental data to establish the above relationship. The first term on the right-hand side represents viscous energy losses that dominate during laminar flow and the second term accounts for kinetic losses that govern in the turbulent regime. Experiments used in the development of the correlation included particles of various shapes such as spheres, cylinders, tablets, and crushed solids [20]. The factors considered in the analysis were fluid superficial bed velocity, particle diameter, fluid viscosity and density, and fractional void volume. The correlation should be valid for hydraulic particle Reynolds numbers between 1 and 3000. The hydraulic Reynolds number differs from the particle Reynolds number that is typically used, in that it has a dependence on the void fraction. The hydraulic particle Reynolds number and particle Reynolds number are defined respectively as

$$Re_{p,h} = \frac{\rho U D_p}{\mu(1-\varepsilon)}\text{, and} \tag{38}$$

$$Re_p = \frac{\rho U D_p}{\mu}. \tag{39}$$

Ergun's equation has been successfully employed to predict the pressure drop of packed beds filled with regular-shaped spherical particles [10, 57, 58]. To develop a more accurate prediction of pressure drop for particle shapes that deviate from spherical, numerous correlations have also been proposed, some of which simply alter the constants *A* and *B*, or modify other bed parameters. Modification has also been made by incorporating the shape factor, or particle sphericity, which is a measure of the degree to which a particle's shape approaches the shape of a sphere. It does not necessarily define the shape, but it describes the effect that the shape has on the hydrodynamic behavior of the bed [59]. The sphericity is defined as [60]

$$\psi = \frac{surface\ of\ sphere\ of\ equal\ volume\ to\ the\ particle}{surface\ area\ of\ the\ particle} = \frac{\pi^{1/3}(6V_p)^{2/3}}{A_p} \qquad (40)$$

Pressure drop correlations are dependent on the particle diameter, D_p, which is equal to the diameter of the particle if it is a sphere. If the particle is non-spherical, an equivalent particle diameter must be used. In Ergun's correlation this is defined as the Sauter-diameter, which is the diameter of a sphere with the same volume-to-surface area ratio as a non-spherical particle:

$$D_{sd} = \frac{6V_p}{A_p}. \qquad (41)$$

Without knowing particle surface area, the Sauter-diameter cannot be determined, therefore an alternative equivalent particle diameter by volume, D_v, defined as the diameter of a sphere having the same volume as the given particle, can be used:

$$D_v = (\frac{6}{\pi}V_p)^{1/3} = \frac{6V_p}{A_{sp}} = \frac{6V_p}{\psi A_p} = \frac{D_{sd}}{\psi}\,. \qquad (42)$$

Ergun's equation can then be written as

$$\frac{\Delta P}{H} = 150\frac{(1-\varepsilon)^2}{\varepsilon^3}\frac{\mu_{HTF}U}{(\psi D_v)^2} + 1.75\frac{1-\varepsilon}{\varepsilon^3}\frac{\rho_{HTF}U^2}{\psi D_v}. \qquad (43)$$

Since particle sphericity is difficult to calculate with irregular shaped solids, it was deduced from Ergun's correlation using Equation 37. The predicted pressure drop was calculated for a range of sphericity values using this equation. The percent average relative absolute error (ARAE) between measured and predicted pressure drop was determined. The sphericity that resulted in the minimum ARAE value was selected. The ARAE is defined as

$$\%ARAE = \frac{1}{n}\sum_{i=1}^{n}\frac{|x_{i,predicted}-x_{i,measured}|}{x_{i,measured}}x\ 100\ . \qquad (44)$$

In order to evaluate Equation 43, the remaining packed bed parameters must be known. The equivalent diameter by volume of the pellets was obtained by measuring the mass of 35 random samples and then utilizing the true density to calculate the volume of each of the samples. The average volume of the 35 samples was subsequently used to obtain the equivalent particle diameter by volume as defined in Equation 42. The resulting diameter was 0.04259 m with a standard deviation of 0.006426 m. Midland Research Center provided the ore density of 3200 kg/m^3.

To determine bed porosity, the total pellet mass and the bed volume were used to estimate the bulk density, where *bulk density = bed mass/bed volume*, which was then used in the following equation to calculate porosity:

$$\varepsilon = 1 - \frac{Bulk\ density}{True\ density}\ . \qquad (45)$$

Porosity was also measured in a separate container of known volume with a diameter that was similar to the final bed diameter to confirm the voidage.

Figure 11 provides an additional system schematic that illustrates the location of the pressure taps and the packed bed arrangement. As can be seen in the figure, the packed bed support plate and the restriction created by the insulation at the exit and entrance of the bed introduce an additional pressure drop. To estimate this value, the pressure drop was measured under varying velocities while the bed was empty. A third-order polynomial best-fit equation was then used to calculate the additional pressure loss. This value was subtracted from the total bed pressure drop to isolate the pressure drop due to the packed bed alone. In order to test whether there was flow maldistribution due to the inlet geometry, velocity was measured at various points in the cross section of the first five to ten centimeters of the bed with a vane anemometer and found to be acceptable.

Pressure drop measurements were conducted for particle Reynolds numbers between $353 \leq Re_p \leq 5206$. This large range was needed to achieve an accurate assessment of the slope of the pressure drop curve. In order to meet this wide range of velocities, three blowers were employed, i.e. a ¼ hp blower, a 1/30 hp blower, and a 7.5 hp blower. The results of the pressure drop measurements as a function of particle Reynolds number are provided in Figure 12. An error propagation uncertainty analysis was conducted and the pressure gradient (ΔP/L) uncertainty is included in the figure. Air mass flux (kg/m^2-s) uncertainty was also calculated and ranged from 3.1% to 3.8%.

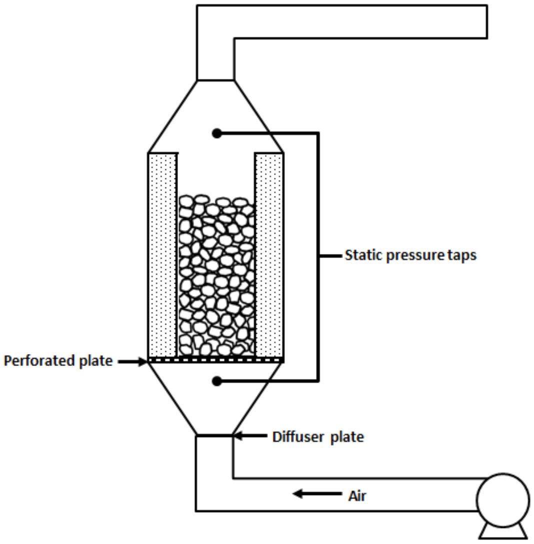

Figure 11. System schematic illustrating the pressure tap locations in the upper and lower plenums.

The figure also includes the pressure drop gradient predicted by Ergun's equation, Equation 43, which combines the sphericity and equivalent particle diameter to produce the Sauter-diameter as provided in Equation 42. Figure 12 additionally includes the predicted pressure drop gradient when particle sphericity is neglected. By using the equivalent particle diameter by volume alone, the Ergun equation underpredicts the pressure drop, therefore the sphericity should be known and incorporated in order to forecast pumping requirements of larger systems with greater certainty. After calculating the percent average relative absolute error for varying values of sphericity, a value of 0.495 resulted in the lowest error of 6.9%.

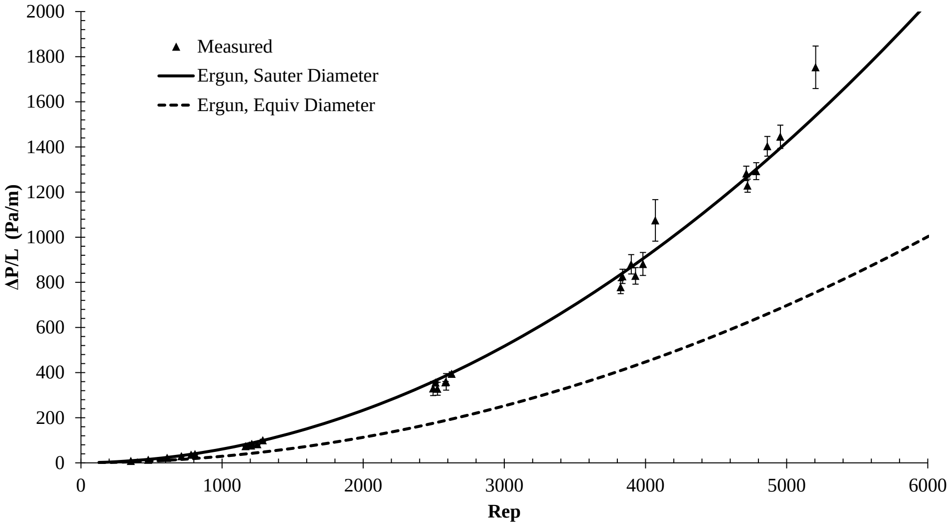

Figure 12. Measured and predicted pressure drop versus particle Reynolds number.

2.3.1.3 Model Validation

The thermal and physical properties of the storage material and packed bed are provided in Table 3. The specific heat capacity of the storage media varies as a function of temperature and was measured by Thermophysical Properties Research Laboratory, Inc. The following equation provides the specific heat capacity of the storage media as a function of temperature in J/(kg-K):

$$Cp(T) = \left(5.18135x10^{-6}(T^3)\right) - \left(7.580075x10^{-3}(T^2)\right) + 5.88548145T - 429.234632 \quad (46)$$

where T is in Kelvin. The equation is valid for temperatures between 23°C - 590°C and was used to model the solid temperature.

Table 3. Experimental and simulation parameters used in validating the SHS model.

Parameter	*Value*
Porosity, ε	0.51
Ore thermal conductivity, k_s	1.5 W/m-K
Ore density, ρ_s	3200 kg/m^3
H_{bed}	0.889 m
D_{bed}	0.4445 m
D_p	0.0425 m
Insulation thickness	0.184 m (7.25in.)
Insulation thermal conductivity	0.06 W/m-K
Tank wall thickness	3.175mm (0.125in.)
Nx	100
Rx	10
Δt	1 sec

Air was used as the HTF in the SHS packed bed experimental system. The thermophysical properties of air were evaluated at the system's average temperature, expressed as the average of the inlet temperature during charging mode and the initial bed temperature, which was defined as ambient. The equations used for evaluating the thermophysical properties of air are defined as follows:

$$\rho_{Air} = (-5.75399E-16)(T^5) + (3.02846E-12)(T^4) - (6.18352E-9)(T^3) + (6.29927E-6)(T^2) - (3.5422E-3)(T) + 1.25079 \text{ in (kg/m}^3\text{)} \tag{47}$$

$$\mu_{Air} = (6.10504E-10)(T^3) - (2.13036E-6)(T^2) + (4.71398E-3)(T) + (1.67555E-5) \text{ in kg/(m-s)} \tag{48}$$

$$Cp_{Air} = (1.28806E-13)(T^4) - (4.46054E-10)(T^3) + (4.8772E-7)(T^2) + (1.82754E-5)(T) + 1.00651 \text{ in kJ/(kg-K)} \tag{49}$$

$$k_{Air} = (-4.44955E-15)(T^4) + (2.41702E-11)(T^3) - (4.09601E-8)(T^2) + (7.91034E-5)(T) + 0.242006 \text{ in W/(m-K)} . \tag{50}$$

Several experimental runs were conducted to furnish a robust data set for model validation. The inlet temperature during charging and discharging mode varied with temperature in the experiments and in the simulation, and were defined by the plenum temperature of the respective mode. Table 4 provides the operating conditions for the validation data set. Figures 13 – 14 and 16 - 19 compare the experimentally measured and numerically modeled air temperature at the five axial positions within the packed bed during charging and discharging mode. Figure 15 provides a comparison of the solid temperature profile during charging mode of Experiment #1. The inlet temperature to the system during each of the modes is provided as a dashed line in the figures that provide air temperature.

Table 4. Operating conditions of the experiments used for model validation.

Experiment #	*Nominal Charging Inlet Temperature (°C)*	*Nominal Discharging Inlet Temperature (°C)*	*Charging Mass Flow Rate (kg/sec)*	*Discharging Mass Flow Rate (kg/sec)*
1	500	190	0.044015	0.04484
2	400	23	0.03453	0.035429
3	200	100	0.035197	0.036356

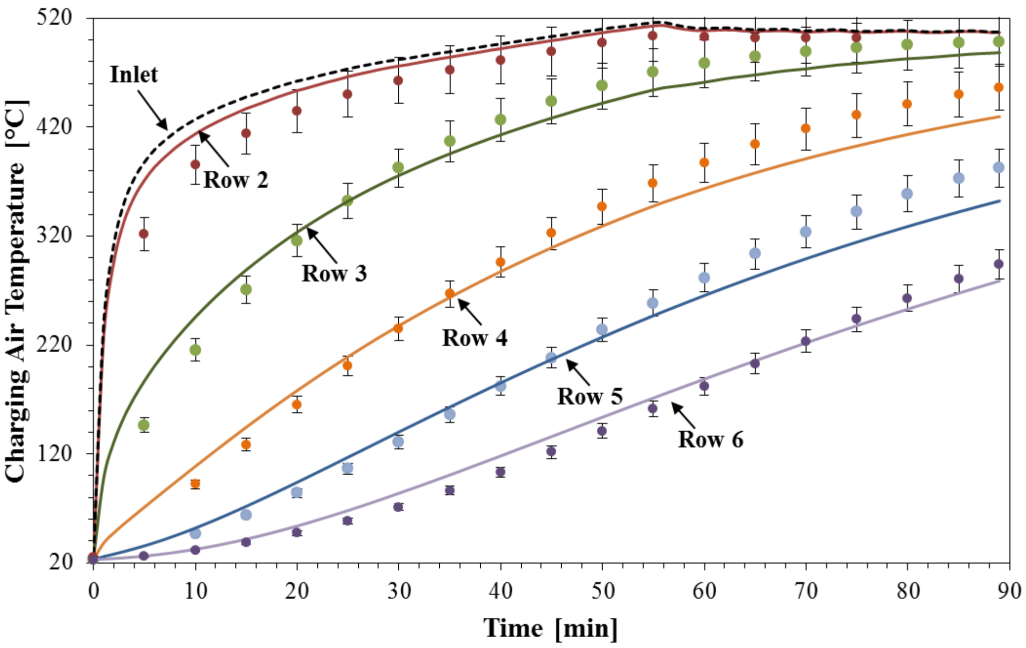

Figure 13. Comparison of modeled and experimental data for charging air temperature of Experiment #1.

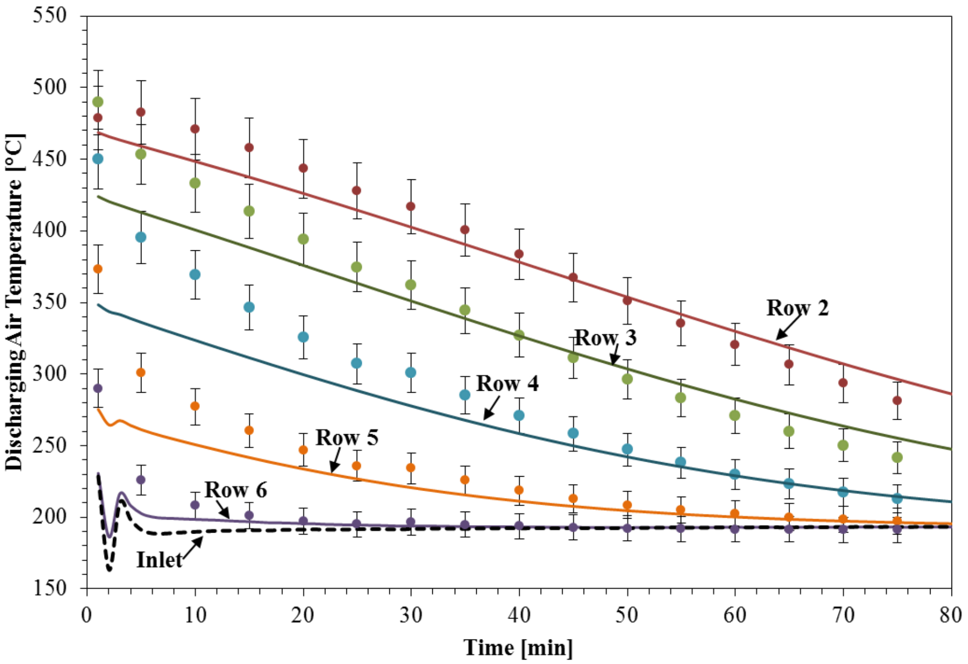

Figure 14. Comparison of modeled and experimental data for discharging air temperature of Experiment #1.

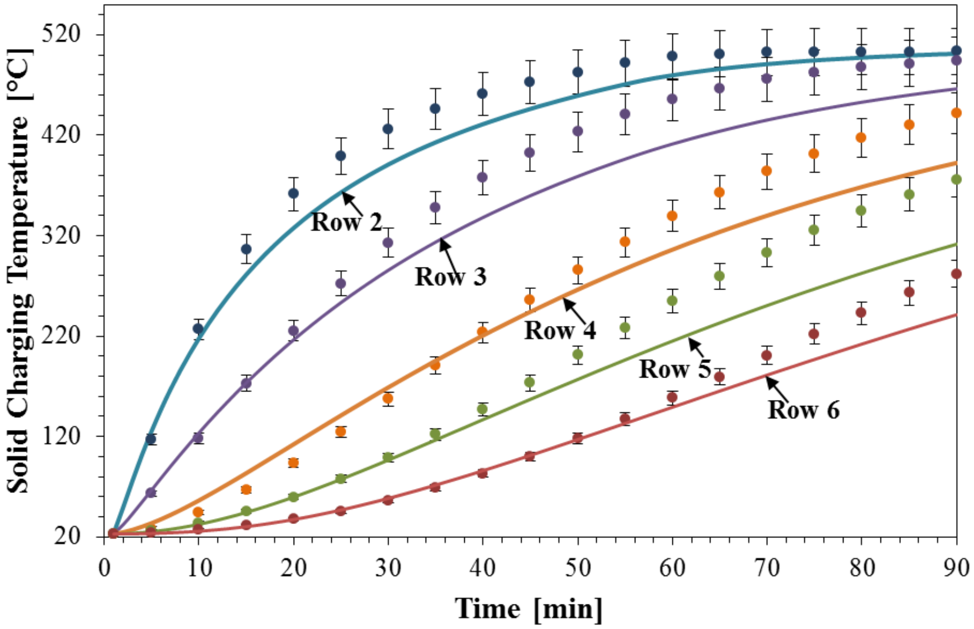

Figure 15. Comparison of modeled and experimental data for solid temperature during charging mode of Experiment #1.

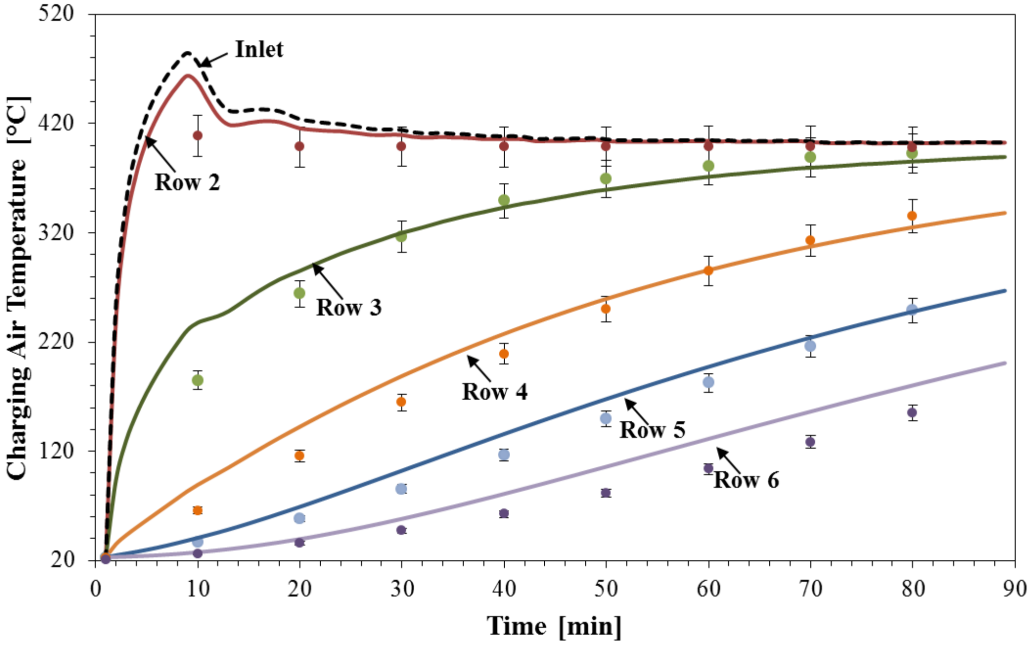

Figure 16. Comparison of modeled and experimental data for charging air temperature of Experiment #2.

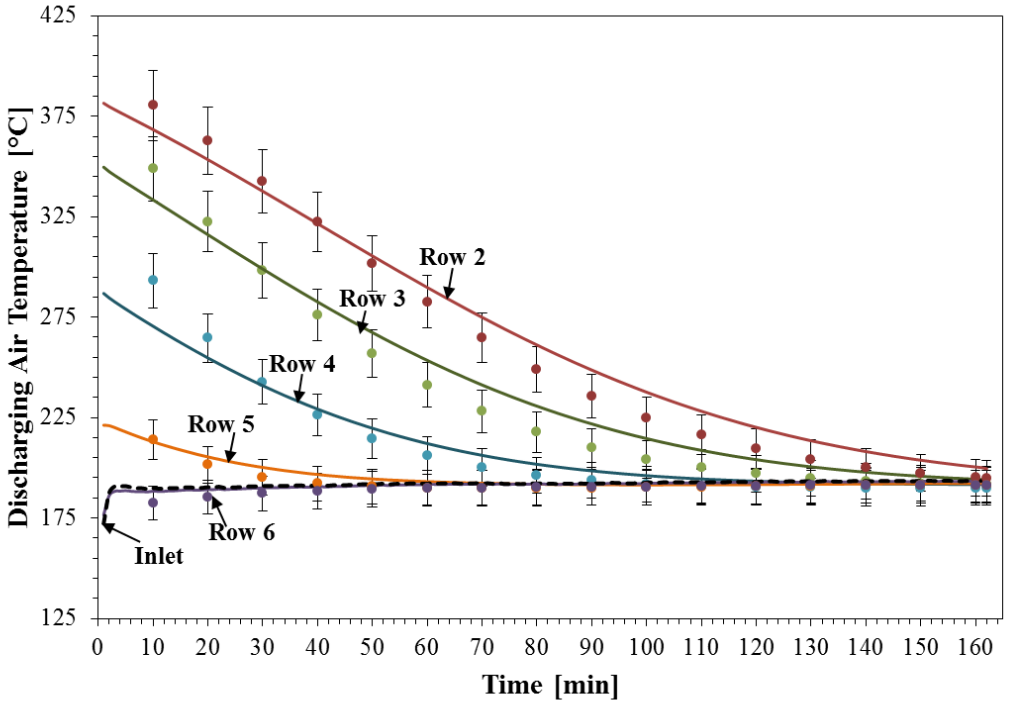

Figure 17. Comparison of modeled and experimental data for discharging air temperature of Experiment #2.

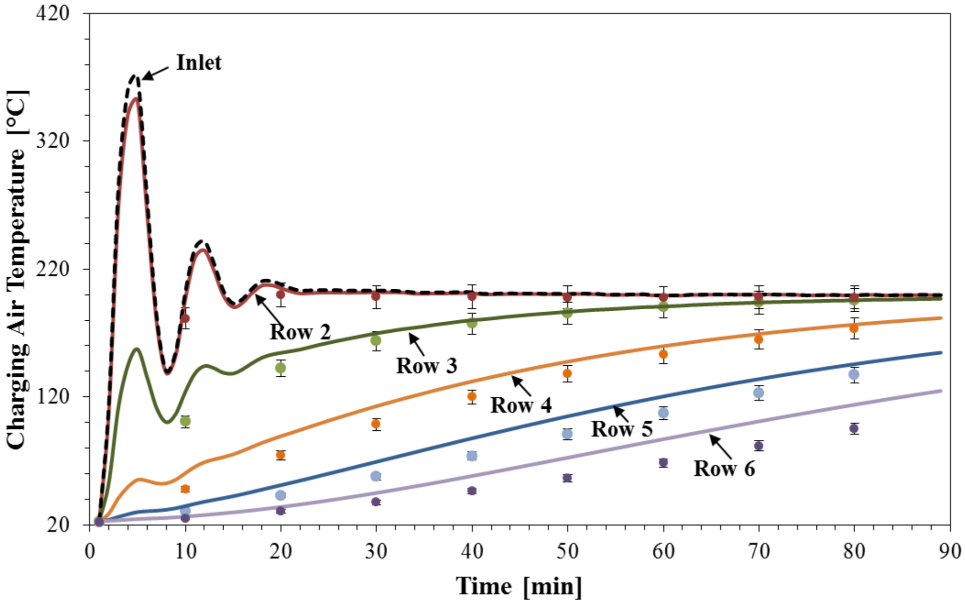

Figure 18. Comparison of modeled and experimental data for charging air temperature of Experiment #3.

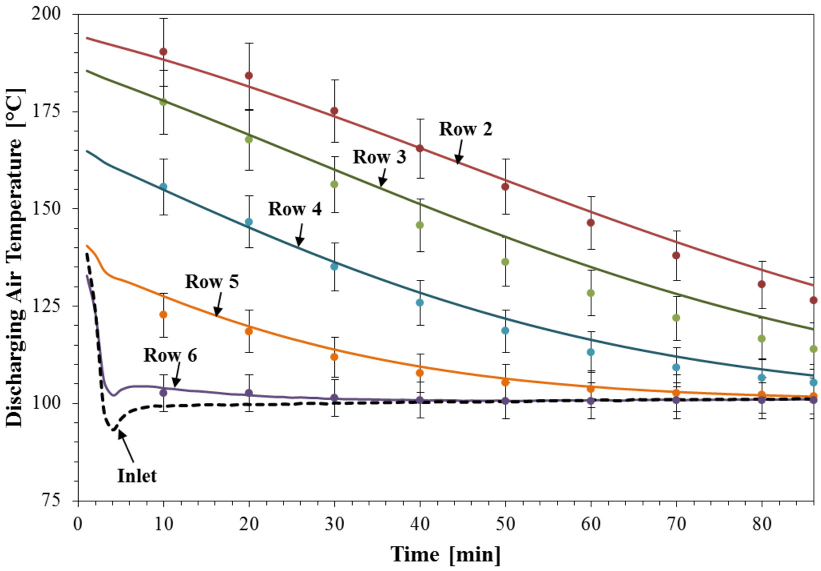

Figure 19. Comparison of modeled and experimental data for discharging air temperature of Experiment #3.

Though the simulated temperature profile does not fall within the uncertainty range of the experimental data in all instances, there is also uncertainty associated with the numerical data due to the inherent error in measurement of the operating parameters that were used in the model (e.g. porosity, mass flow rate, particle diameter, etc.). Thus the numerically modeled temperature profiles are in reasonable agreement with the experimental data.

2.3.1.4 Validation of the Use of Molten Salt as a HTF

Though air is used as a HTF in central receiver CSP plants, molten salt is more commonly adopted in demonstration and utility-scale facilities. As such, performance analyses in subsequent chapters are carried out with molten salt as the HTF. To validate the use of molten salt in the Dispersion-Concentric model, the experimental data of Pacheco et al. [36] was employed. A 2.3 MWh thermocline pilot-scale system used a $NaNO_3$-KNO_3 eutectic as the HTF and a combination of quartzite and silica sand as the storage medium. The same validation methodology of Flueckiger et al. [31] was adopted, wherein the final temperature during charging mode was taken as the initial temperature of the system during discharging given that the initial condition was not provided in the original study. The input parameters included the following: superficial bed velocity = 4.36x10^{-4} m/s; solid density = 2500 kg/m^3; porosity = 0.22; specific heat capacity = 830 J/kg-K; inlet HTF temperature = 290°C; solid thermal conductivity = 5 W/m-K; particle diameter = 0.01905 m; tank wall thickness = 0.04 m and insulation thickness = 0.23 m [27, 31]. In order to determine if the thermophysical properties of the HTF must vary with temperature in the simulation, the results of constant properties versus temperature dependent properties were compared and the difference was negligible. Therefore the thermophysical properties of the HTF were taken as a constant, average value over the operating temperature range of the system. These values are as follows: ρ_{HTF} = 1818.8 kg/m^3, k_{HTF} = 0.524 W/(m-K), and $C_{p,HTF}$ = 1516.4 J/kg-K. The thermophysical properties of the molten salt are provided in [27] as

$$\rho_{salt}(T) = (-0.6354T) + 2089.9 \text{ in kg/m}^3 \tag{51}$$

$$\mu_{salt}(T) = (-1.473189317978E^{-10} \cdot T^3) + (2.279835623143E^{-7} \cdot T^2) \\ -(1.199467889194E^{-4} \cdot T) + 2.270644077145E^{-2} \text{ in kg/(m-s)} \tag{52}$$

$$Cp_{salt}(T) = (0.172T) + 1443 \text{ in J/(kg-K)} \tag{53}$$

$$k_{salt}(T) = (0.00019T) + 0.44299 \text{ in W/(m-K)} \tag{54}$$

The system discharged for 2 hours and the simulated results are compared to the experimental data in Figure 20.

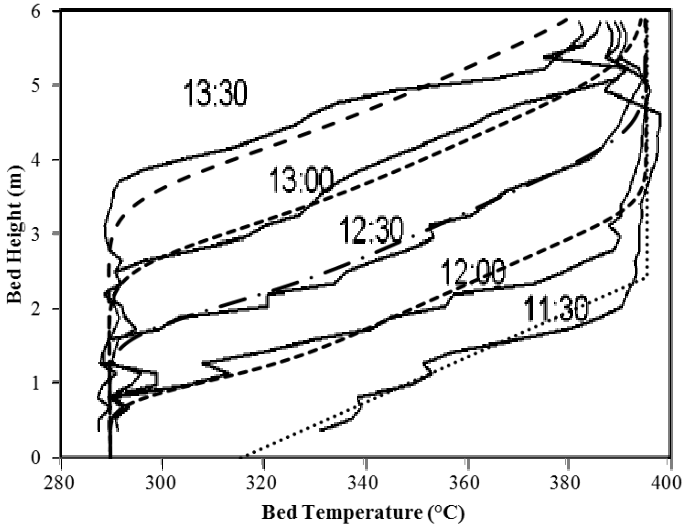

Figure 20. Plot of simulated data and experimental results for a packed bed molten salt SHS system. The experiment was conducted in Pacheco et al. [36]. Dashed lines represent results from the D-C model.

2.3.2 Latent Heat Storage Model Validation

As discussed in Section 2.2.1, three apparent heat capacity functions were analyzed for their ability to simulate the phase change process. Model validation was executed with the use of a laboratory-scale prototype LHS system of 770 randomly packed sodium nitrate spheres that were encapsulated in a high melting temperature polymer. The experimental setup for charging mode is provided in Figure 21 and the specifications of the complete experimental setup as well as the uncertainty calculations can be found in the work of Alam et al. [61, 62]. The tank of the pilot-scale SHS system described in Section 2.3.1.1 was replaced with a smaller tank that could accommodate the lower volume required for the capsules. The system was operated with volumetric flow rates that ranged between 110 m^3/hr and 151 m^3/hr, and it utilized the same instrumentation to measure pressure, flow rate, and temperature as the SHS system. Hooded k-type thermocouples were installed at four axial positions along the packed bed height. At each axial position, there were five thermocouples placed across the diameter of the bed to monitor air temperature and flow uniformity. Thermocouples were also placed within a PCM capsule that was positioned at the center of each thermocouple row. These capsules were constructed differently than the remaining capsules in order to accommodate the thermocouple. Rather than a single contiguous sphere of salt encapsulated in polymer, the monitoring capsules consisted of two individually encapsulated hemispheres that were bound together to form a single sphere. The thermocouple was placed between the two hemispheres. Consequently, the temperature provided by this thermocouple did not accurately represent the center temperature of each sphere, as was later proven in an external study. Thus the HTF temperature of the system was used in validating the model and the PCM temperature was disregarded.

Table 5. LHS packed bed simulation parameters.

Description	Nominal value	Reference
Bed height	0.254 m	
Bed diameter	0.254 m	
Bed porosity	0.348	
Particle inner diameter	0.02653 m	
Particle shell thickness	0.00045 m	
Tank wall thickness	0.00635 m	
Tank thermal conductivity	43.84 W/m-K	[63]

Table 5 (continued)

Insulation thickness	0.1524 m
Insulation thermal conductivity	0.06 W/m-K
$NaNO_3$ solid thermal conductivity	0.50 W/m-K
$NaNO_3$ liquid thermal conductivity	0.54 W/m-K
$NaNO_3$ solid density	1908 kg/m^3 [64]
$NaNO_3$ liquid density	2125 kg/m^3 [64]
$NaNO_3$ latent heat	172,000 J/kg
$NaNO_3$ solid specific heat	1835.4 J/kg-K [65]
$NaNO_3$ liquid specific heat	1655 J/kg-K [65]
$NaNO_3$ melting point	306°C
$NaNO_3$ solidification point	304°C
Capsule PTFE thermal conductivity	0.22 W/m-K
N_x – axial grid steps	50
R_x – radial grid steps per sphere	50

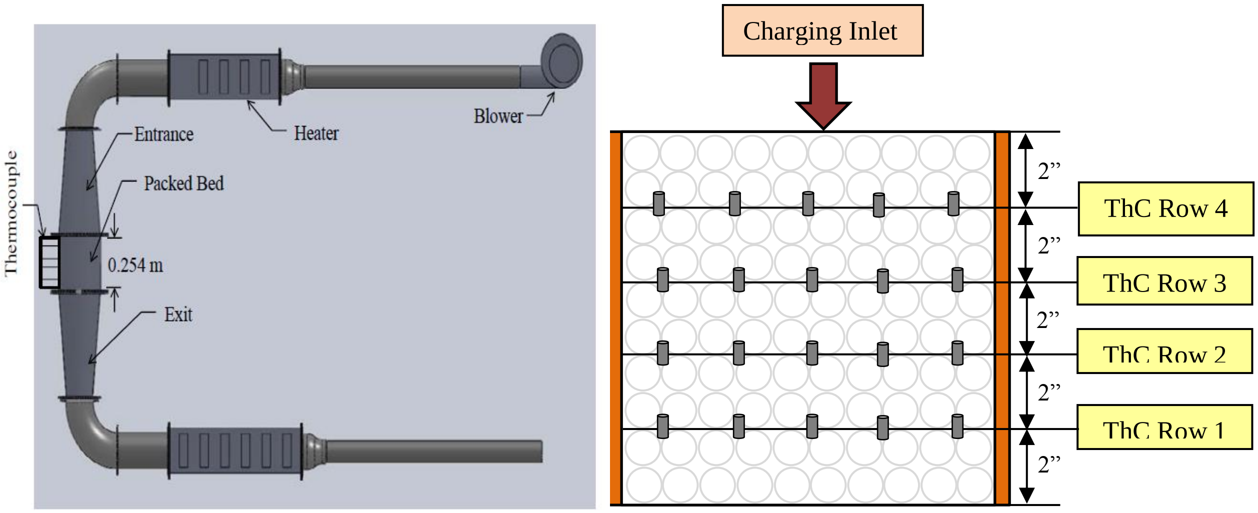

Figure 21. LHS laboratory-scale prototype system schematic and thermocouple (ThC) map. Details of the experiment can be found in [61].

For each experimental run, the entire packed bed was first completely pre-heated to 285°C using the top heater and centrifugal blower. Charging mode then commenced by heating the inlet air at the top of the bed to 326°C and was completed when the PCM temperature at the bottom row reached the inlet temperature. The blower was then positioned at the bottom of the system and discharging mode began by heating the inlet air at the bottom of the system to 286°C and removing energy from the capsules until the PCM temperature at the top of the bed reached approximately 286°C. The parameters used in the model are provided in Table 5. Though a constant inlet temperature was assumed during charging, the inlet temperature during discharging mode initially varied with time due to the thermal inertia of the system and is included in the plot of row 2 for the discharging process.

2.3.2.1 Evaluation of the Effective Heat Capacity Function

The three aforementioned effective heat capacity functions, i.e. the DSC curve of Equation 30, rectangular function of Equation 36, and logistic function of Equation 35, were used in the Dispersion-Concentric model to evaluate their efficacy in predicting the temperature profile of the experimental data. Though the Dispersion-Concentric model accounts for intra-particle diffusion, during the validation process it was observed that there was additional resistance to heat transfer during phase change that was not accounted for by the physics of the model. Hence the external convective heat transfer correlation proposed by Wakao et al. [21] was used in conjunction with the effective heat transfer equation, Equation 55, provided by Jeffreson [66], to create a closer match between the experimental and simulated data.

$$h_{effective} = \frac{h_p}{1+0.2Bi} \tag{55}$$

This effective heat transfer coefficient replaced the particle coefficient, h_p, in the energy equation calculations. All other correlations used in the SHS model were employed in the LHS model. When natural convection was included in the simulation, the PCM increased in temperature too rapidly and the simulated temperature profile was not in good agreement with the experimental results, therefore natural convection within the PCM capsules was excluded. In Nithyandandam and Pitchumani [35], it was shown that natural convection did not have any significant effect on the charge rate for small particles. In Jalalzadeh-Azar et al. [67], the results from a high temperature packed bed of 12.7 mm diameter PCM pellets (T_{melt} = 880°C) were used to validate a numerical model that neglected natural convection within the PCM capsules. The simulation matched within reason of the experimental values, therefore the inclusion of natural convection may not be necessary for all packed bed scenarios and is considered negligible for the particle size under study in this investigation.

A constant solid heat capacity and constant liquid heat capacity was assumed when the PCM was in each respective phase. The effective heat capacity is applied to any node in which the PCM temperature lies between the solidus and liquidus temperatures, as can be visualized by Figure 22 for the rectangular function.

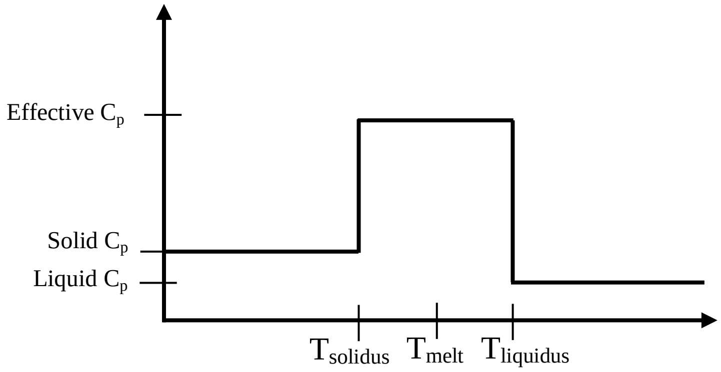

Figure 22. Variation of heat capacity with temperature for a rectangular effective heat capacity function.

To obtain an effective heat capacity function using DSC measurements, a heat flow curve was determined via a TA Instruments Q600 TGA/DSC. The instrument provides simultaneous thermogravimetric analysis as well as differential scanning calorimetry. A sample of sodium nitrate of the same grade used in the packed bed pellets (98+%) was heated and cooled through the phase change temperature in ceramic alumina pans under a nitrogen gas purge. The instrument was calibrated for a ramping rate of 1K/min, and this rate was used in the measurements and to determine the melting and solidification effective heat capacity curves with Equation 30. The latent heat of fusion and melting temperature acquired from the measurements were 170.9 kJ/kg and 306.35°C, respectively. The latent heat of solidification and solidification temperature were 170.1 kJ/kg and 302.34°C, respectively. The solid and liquid specific heat capacities were referenced from [64, 65] and are provided in Table 5. The effective heat capacity curves are illustrated in Figures 23 and 24.

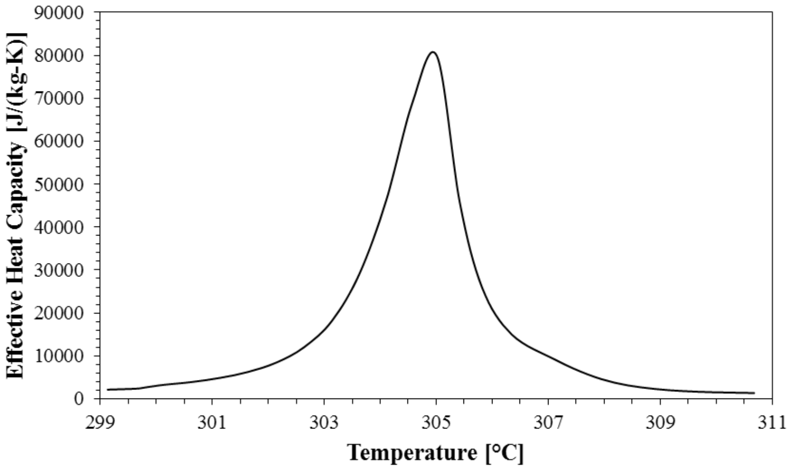

Figure 23. Effective heat capacity curve of the melting process for sodium nitrate. The sample was heated at 1K/min.

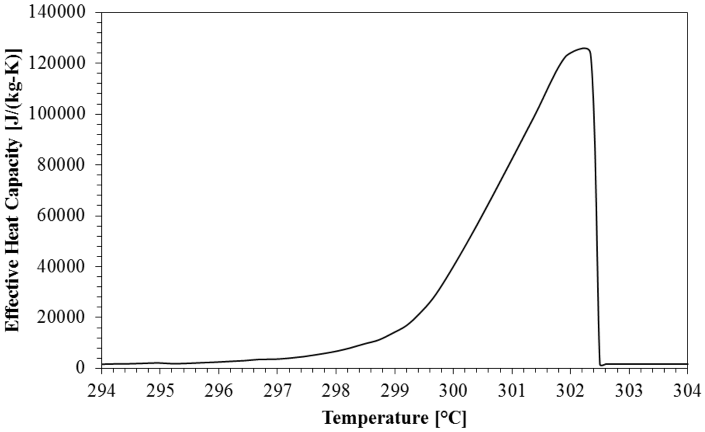

Figure 24. Effective heat capacity curve of the solidification process for sodium nitrate.

Polynomial regression equations were employed to reproduce the shape of the effective heat capacity curves. Two distinct fourth order polynomial equations were used to model the heat capacity during melting: one from the onset to the peak of melting and another from the peak to the liquidus point, defined respectively as

$$Cp_{eff} = (-6.138410916 \cdot T^4) + (8.184093887E^3 \cdot T^3) - (4.054467609E^6 \cdot T^2) + (8.859274628E^8 \cdot T) - 7.212555798E^{10} \quad \text{for } 299.84°\text{C} \le \text{T} < 306.35°\text{C} \qquad (56)$$

and

$$Cp_{eff} = (40.885751986 \cdot T^{4}) - (5.1536031432E^{4} \cdot T^{3}) + (2.4355700734E^{7} \cdot T^{2}) - (5.1148076097E^{9} \cdot T) - 4.0272892760E^{11} \quad \text{for } 306.35°\text{C} \le T \le 310.68°\text{C} \qquad (57)$$

A single 6th order polynomial was used to characterize solidification from the peak to the solidus point:

$$Cp_{eff} = (-11.7992675546556 \cdot T^{6}) + (2.10409802521218E^{4} \cdot T^{5}) - (1.5633494286549E^{7} \cdot T^{4}) + (6.19491471878624E^{9} \cdot T^{3}) - (1.38078998166774E^{12} \cdot T^{2}) + (1.64138018646662E^{14} \cdot T) - 8.12961689535658E^{15} \quad \text{for } 295.2°\text{C} \le T \le 302.34°\text{C} \qquad (58)$$

It should be noted that the significant figures in Equations 56 - 58 are needed to provide a reasonably accurate estimate of the effective heat capacity.

The logistic function provides a smooth, continuous effective heat capacity curve, the shape of which is defined by the parameter α. As illustrated in Figure 25, a short, broad peak develops for low α values, therefore the melting temperature range increases as α decreases.

The rectangular function invokes a constant effective heat capacity value between the solidus and liquidus temperatures. For the comparison, a phase change temperature range of 2°C was chosen for both rectangular and logistic functions. An alpha parameter of 15 induces the 2 degree phase change temperature range. Figure 26 provides a comparison of all three curves that were employed in the study.

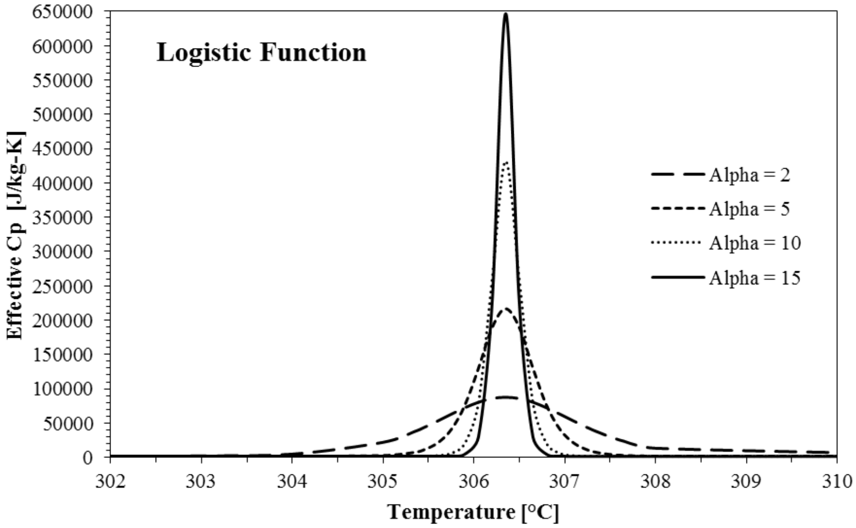

Figure 25. Effect of the alpha parameter on the shape of the logistic function effective heat capacity curve.

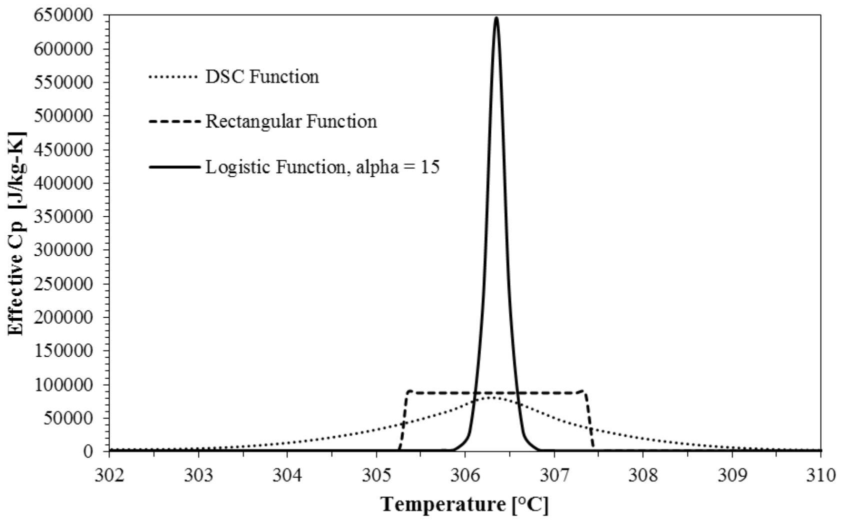

Figure 26. Effective heat capacity curves for each function studied in the LHS model.

The percent average absolute relative error, Equation 44, was calculated for the three functions of thermocouple rows 2 through 4. The comparison was made with experimental data in which the system flow rate was 151 m^3/hr (0.05 kg/s). Figure 27 provides a comparison of the simulated temperature profile of the three functions and experimental data of row 3. For the charging and discharging processes, the logistic function and rectangular function are nearly indistinguishable and deviate slightly from the DSC function. During discharging mode, the DSC function diverges from the logistic and rectangular functions as the PCM is liberated from the solidification process. The same trend was observed in rows 2 and 4 and is likely due to the DSC curve's lack of symmetry during solidification as compared to the logistic and rectangular functions, which are symmetric about the solidification temperature.

Table 6 presents the percent average relative absolute error for the three functions. The relative error between simulated and measured air temperature remains below 1% in every instance, and though the rectangular function shows the largest error, the difference is minor. The simplicity of the rectangular function warrants its use, therefore this function was adopted in the LHS model using a 2°C phase change temperature range.

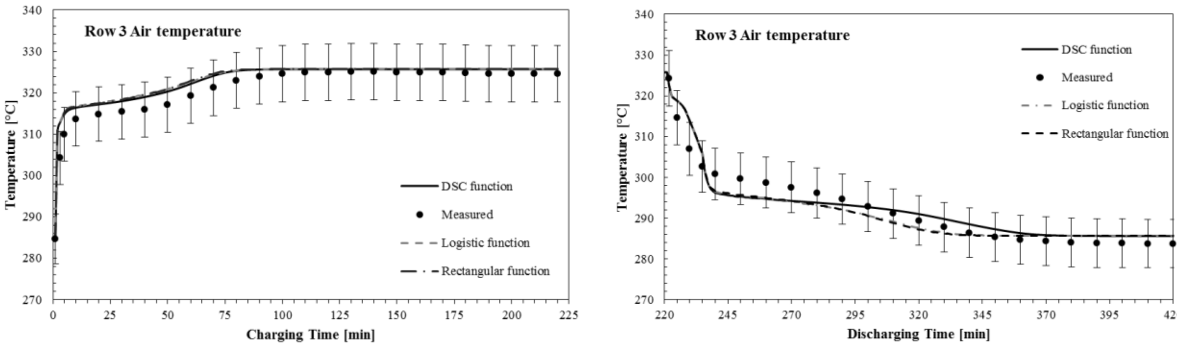

a. b.

Figure 27. Row 3 comparison of simulated air temperature profile vs. experimental results. The three effective heat capacity functions are presented for a) charging mode and b) discharging mode.

Figure 28 provides the measured and simulated temperature profile for rows 2 through 4 of the packed bed system. As previously mentioned, the inlet air temperature during discharging mode varied with time, therefore this profile is provided in the row 2 discharging air temperature figure 28b. The rectangular function with a 2°C phase change temperature range was adopted in the simulation. The figure demonstrates that the simulated temperature of air predominantly falls within the experimental uncertainty range and is in close agreement with the measured results.

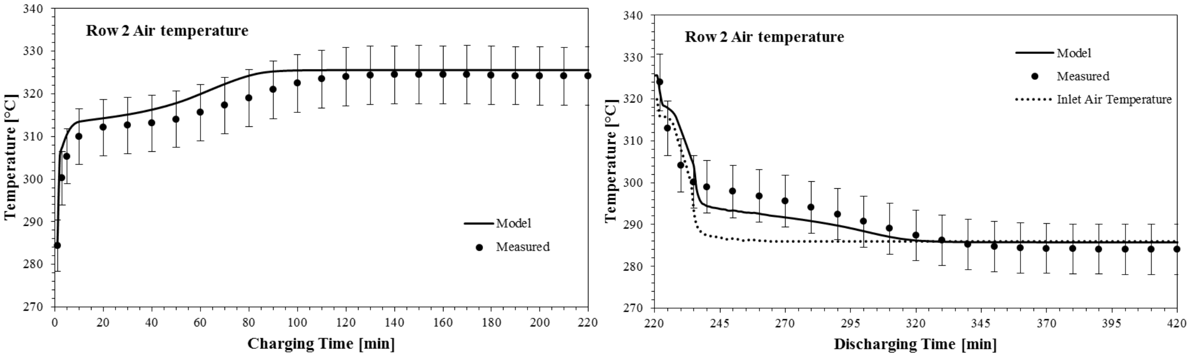

a. b.

Figure 28. Numerically modeled and experimentally measured temperature profile of air in a packed bed of sodium nitrate capsules. Figures 28a, c, and 3 provide charging mode results and b, d, and f provide discharging mode results for thermocouple rows 2 through 4 in the experimental system.

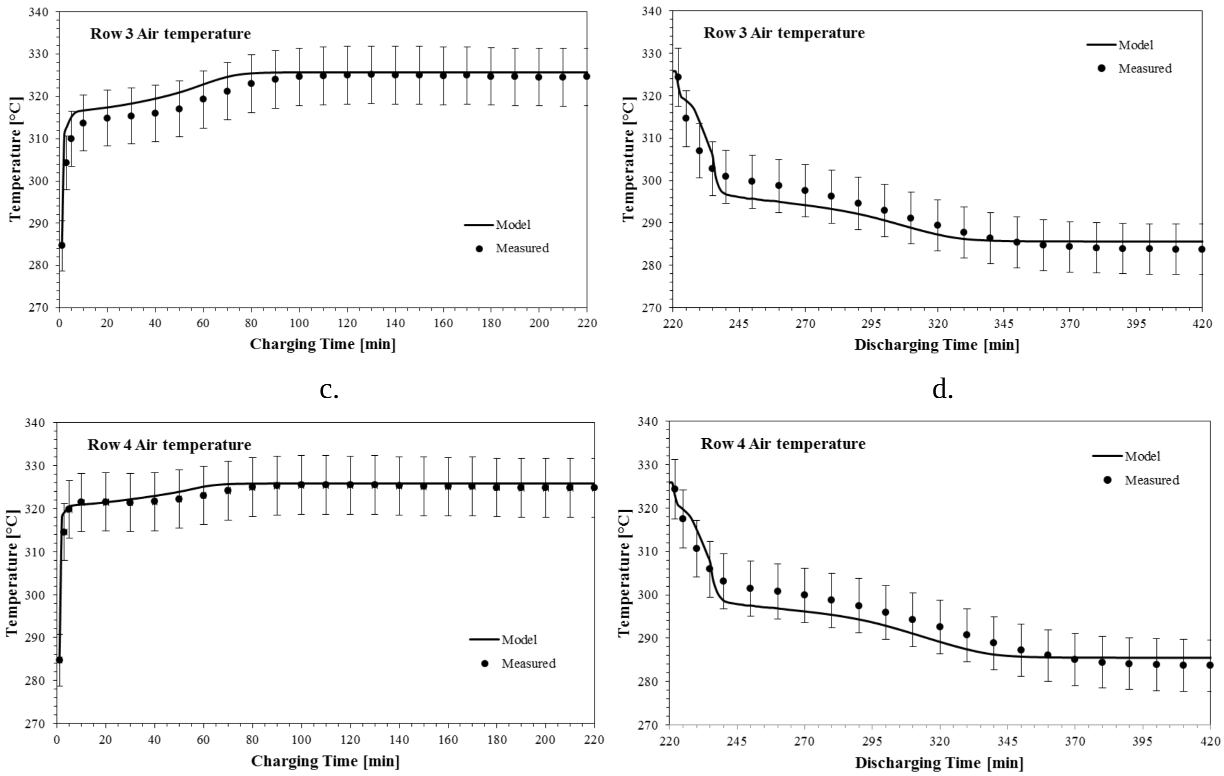

c. d.

e. f.

Figure 28 (continued)

Table 6. Percent ARAE of measured and simulated air temperature for each effective heat capacity function.

Thermocouple row	*DSC function*	*Logistic function*	*Rectangular function*
Row 2	0.759%	0.809%	0.813%
Row 3	0.659%	0.680%	0.684%
Row 4	0.499%	0.551%	0.556%

Thermocouple row 1 was neglected in the analysis as the simulated results deviated significantly from the measured data. To gauge whether there was a flaw in the simulation or the experimental system, the air temperature profile was simulated while the sodium nitrate capsules were heated sensibly. Figure 29 provides the temperature profile for all four rows and demonstrates that during the pre-heating stage, i.e. from room temperature to 285°C, row 1 diverges to a greater degree from the measured data than the remaining three rows. Since this row was located at the bottom of the bed, there may have been an issue with leakage of the PCM or shifting of the capsules. The input parameters for the simulation during sensible heating include the following: initial bed temperature = 23°C, solid density = 2200 kg/m^3, solid thermal conductivity = 0.5 W/(m-K), solid specific heat capacity = 1394 J/(kg-K), and mass flow rate = 0.05 kg/s. The effective heat transfer coefficient, Equation 55, was not applied during this phase of sensible heating and the solid-solid second order transition that occurs at 275°C was not observed in the measured results, which is likely due to its low value that is reported between 12 – 45 J/g [64].

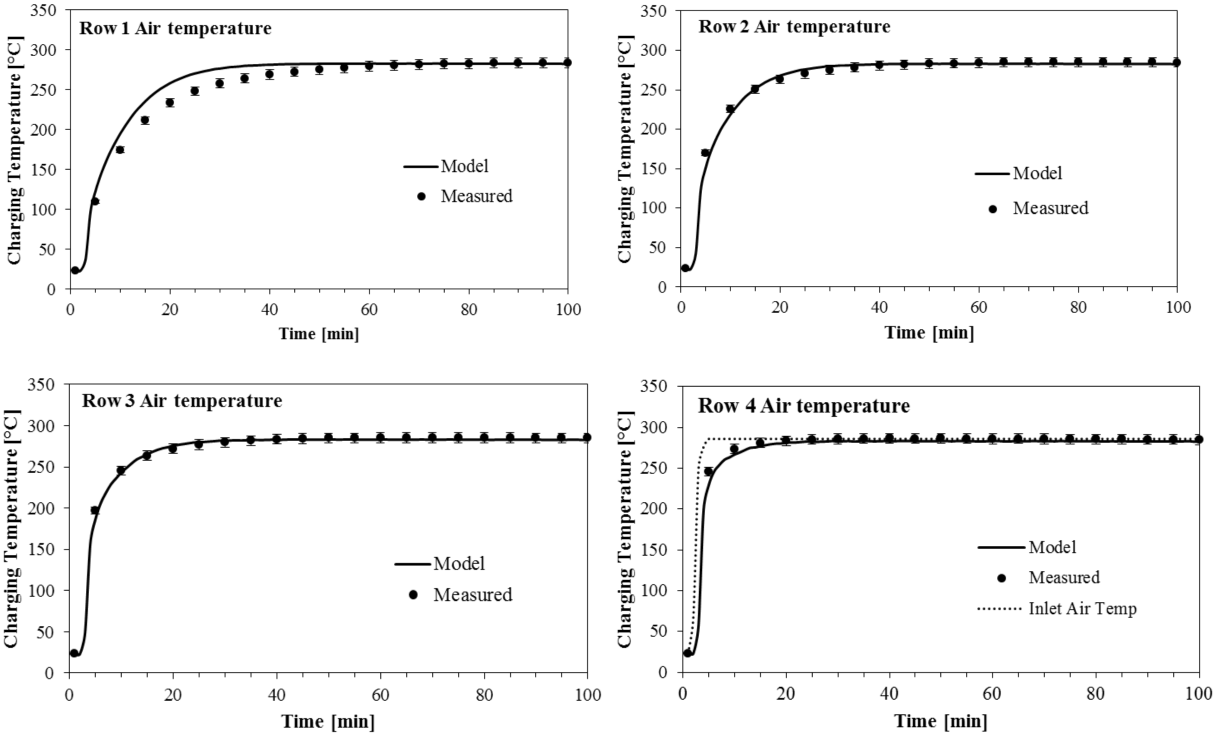

Figure 29. Numerically modeled vs. measured air temperature profile of the LHS packed bed as the capsules were heated sensibly during charging mode. The inlet air temperature is provided in the profile of Row 4.

CHAPTER 3: PERFORMANCE ANALYSIS

3.1 Introduction

The purpose of this chapter is to compare the performance of LHS and SHS thermocline systems and understand the dynamics of their behavior. The evaluation will expound upon two previous studies that investigated LHS systems from a plant level and a storage system level, i.e. the work of Flueckiger and Garimella [5], and Nithyanandam and Pitchumani [35], respectively.

Three assessments are conducted. The first two assessments evaluate hypothetical PCMs in order to isolate the influence of different parameters under investigation, and the third analysis evaluates the use of potential PCMs for use in a real system. The three analyses are conducted as follows:

1.) A SHS and two single-PCM LHS packed bed systems are compared under the context that all thermal and physical properties are equal, aside from the addition of latent heat in the LHS system. The goal is to understand how the phase change process and phase transition temperature affects the LHS system's output and efficiency.

2.) 2-PCM and 3-PCM LHS cascaded systems are compared to investigate thermodynamic and energy output advantages over the single-PCM design.

3.) Realistic parameters for each system are designated by adopting the thermal and physical properties of the respective experimental packed beds used in validating the model. Thus the parameters used for the SHS system are derived from the actual packed bed characteristics of the pilot-scale system in Pacheco et al. [36] and the parameters for the LHS system stem from the characteristics of the lab-scale setup of Alam et al. [62], however a PCM with higher melting temperature is substituted.

In order to compare the systems, they each operate under the conditions defined in Table 7. To minimize the effect of dissimilar convective heat transfer rates, the HTF mass flux is maintained as a constant value across all systems by defining a constant tank diameter and mass flow rate for each system, as specified in Table 7. After completing a grid and time step study, the axial domain of the packed bed was discretized into uniformly spaced nodes that were 0.025 m apart and the time step was defined as 1 second. Each filler sphere was divided into 30 equally spaced elements in the radial direction for the LHS system and 10 equally spaced elements in the SHS system. The volume averaged filler temperature was used to calculate the temperature difference between storage material and HTF in subsequent sections.

The parameters of the analysis are based on a central receiver CSP facility that employs molten salt as the HTF. The hot operating temperature of the solar field, $T_{HTF,h}$ is based on the safety margin needed to minimize the formation of corrosive nitrites in the molten salt [1]. The inlet temperature during discharging mode, or the cold operating temperature of the solar field, $T_{HTF,c}$, is required to prevent solidification of the salt. The cut-off criteria for the charging and discharging processes from Nithyanandam and Pitchumani [68] are applied. These threshold values are characterized by a normalized temperature, which is expressed as

$$\theta = \frac{T - T_{HTF,c}}{T_{HTF,h} - T_{HTF,c}}. \tag{59}$$

The charging threshold normalized temperature is 0.39 and the discharging threshold value is 0.74. Each system was cycled until steady state was achieved. At this point, the system consistently discharged the same quantity of thermal energy in MWh to the fourth decimal place.

The previous LHS investigations of Flueckiger and Garimella [5], and Nithyanandam and Pitchumani [35] provide a starting point for PCM melting point selection. The studies demonstrated that there is a severe reduction in system output, utilization, and a plant's capacity factor when the the phase transition temperature falls between the charging (θ_c') and discharging (θ_d') cut-off temperatures, i.e. when $\theta_c' < \theta_m < \theta_d'$. Flueckiger and Garimella [5] additionally demonstrated that a LHS system only outperforms a SHS packed bed system when the transition temperature falls below the charging cut-off temperature. When this condition is met, there is an improvement in a plant's capacity factor and a decrease in thermal energy discard, where the thermal energy discard is the energy lost due to storage limitations. If, for example, a storage system reaches its saturation condition while sufficient solar radiation is still available, the heliostats must defocus to a state that supplies energy for steam generation alone. The energy that could have been harnessed for storage is the thermal energy discard.

Based on these phase transition temperature limitations, two PCMS with a low and high melting point were chosen for use in the LHS system of Analysis 1. The first is based on a eutectic of sodium chloride and potassium sulfate with a phase transition temperature of 515°C. This PCM was deemed suitable for the current application ($\theta_{melt} = 0.82$) as it lies above the discharging threshold temperature. The two salt components form a quaternary system consisting of 15.1wt% K_2Cl_2 - 21.8% Na_2Cl_2 - 25.2% K_2SO_4 - 37.9% Na_2SO_4. The latent heat of fusion was measured with a TA Instruments Q600 TGA/DSC and the resulting value is 187000 J/kg. The corresponding heat flow curve is illustrated in Figure 30. The melting point of the second PCM falls immediately below the charging cut-off temperature. The chosen temperature is 395 °C ($\theta_{melt} = 0.386$), and the latent heat is defined as equivalent to the first PCM, with a value of 187000 J/kg.

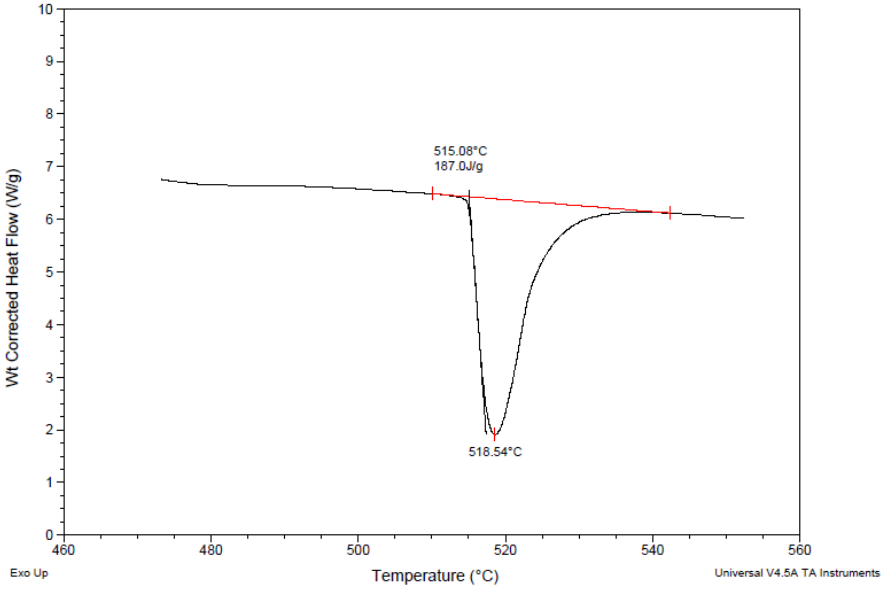

Figure 30. Melting heat flow curve of the sodium chloride and potassium sulfate eutectic mixture.

Table 7. Input values for TES model. Theses common assumptions are used in all analyses.

Description	**Value**
$T_{HTF,h}$	565°C
$T_{HTF,c}$	288°C
$T_{max,Ch}$	396°C
$T_{min,Dch}$	493°C
$\dot{m}$	84.5175 kg/s
Tank diameter	10.593 meters
ρ_{HTF}	1818.8 kg/m^3
k_{HTF}	0.524 W/m-K
$C_{p,HTF}$	1516.4 J/kg-K

3.2 Performance Indicators

Various indicators are used in the literature to quantify the performance of storage systems and to compare different operating scenarios. The second-law efficiency, or exergy efficiency, is one such metric that is used in this study to take into account the quantity and quality of energy that is stored and recovered from the system. This efficiency is used in conjunction with the capacity ratio and utilization ratio to understand system behavior.

Assuming that the HTF is incompressible, the overall exergetic efficiency of a complete cycle is defined as the ratio of net exergy recovered over the net exergy supplied [69]:

$$\eta_{II} = \frac{Ex_{recovered,HTF,NET}}{Ex_{supplied,HTF,NET}} \tag{60}$$

where

$$Ex_{recovered,HTF} = \int_{t_{initial,Dch}}^{t_{final,Dch}} \dot{m}_{HTF} c_{p,HTF} \left(T_{HTF,out} - T_{HTF,inlet} - T_o \ln\left(\frac{T_{HTF,out}}{T_{HTF,inlet}}\right)\right)]dt \tag{61}$$

$$Ex_{supplied,HTF} = \int_{t_{initial,ch}}^{t_{final,ch}} \dot{m}_{HTF} c_{p,HTF} \left(T_{HTF,in} - T_{HTF,out} - T_o \ln\left(\frac{T_{HTF,in}}{T_{HTF,out}}\right)\right)]dt \tag{62}$$

The capacity ratio describes the degree to which the maximum theoretical storage capacity is utilized during the charging process and is defined as [18]

$$Capacity\ ratio = \sigma = \frac{Q_{stored}}{Q_{max\ possible\ stored}} \tag{63}$$

The energy stored in the PCM is calculated as a summation of the total energy stored in the capsules at the end of charging mode.

To calculate the energy stored in each filler sphere, the model determines whether the control volume of each radial node is in the solid, liquid, or mushy phase. If the PCM temperature falls within the predefined phase change temperature range, the liquid fraction is determine. This is defined as:

$$Liquid\ fraction\ = \frac{T_{pcm,r} - T_{solidus}}{T_{liquidus} - T_{solidus}}. \tag{64}$$

In contrast, the utilization ratio characterizes the amount of energy that is extracted versus the maximum potential stored energy that could be recovered during the discharging process if the PCM were to be cooled to the initial bed temperature [35]

$$Utilization\ ratio = \gamma = \frac{Q_{discharged,total}}{Q_{maximum\ possible\ stored}} \tag{65}$$

where the discharged energy is determined by calculating the difference between the energy stored at the end of the charging cycle and the energy remaining in the filler material after the discharging cycle:

$$Q_{discharged,i} = Q_{stored\ after\ charging,i} - Q_{stored\ after\ discharging,i} \tag{66}$$

where i is the given cycle under consideration. The maximum possible storage capacity of the system is defined as

$$Q_{max\ possible\ stored} = m_{pcm} c_{p,liquid} \left(T_{inlet} - T_{pcm,liquidus}\right) + m_{pcm} \Delta h + m_{pcm} c_{p,solid} \left(T_{pcm,solidus} - T_{pcm,initial}\right) \tag{67}$$

Equations 61 and 62 are calculated at the end of each minute and summed over the charging and discharging period to calculate the total exergy supplied or recovered.

3.3 Comparative Performance Evaluation of Packed Bed Systems

3.3.1 Analysis 1: SHS vs Single-PCM LHS Systems

In this analysis, the tank size was defined as 650 m^3 for the LHS and SHS systems. Both systems utilize the thermal and physical properties of the prototype SHS system of Pacheco et al. [36]. The parameters used in this analysis are provided in Table 8. The SHS system has a potential storage capacity of 81 MWh, which was calculated with the difference between $T_{HTF,h}$ and $T_{HTF,c}$. The LHS systems have the same potential sensible heat storage capacity yet have an additional 66 MWh due to latent heat, totaling 147 MWh. To distinguish the two LHS systems, they are identified as $\mathrm{LHS}_{\mathrm{high}}$ and $\mathrm{LHS}_{\mathrm{low}}$, corresponding to melting points of 515°C and 395°C, respectively.

Table 8. Thermal properties of storage media and physical parameters of the SHS and LHS systems evaluated in Analysis 1.

Parameter	*Value*
Porosity	0.22
$C_{p,PCM,solid}$	830 J/kg-K
$C_{p,PCM,liquid}$	830 J/kg-K
ρ_{PCM}	2500 kg/m3
k_{PCM}	5.0 W/m-K
Latent heat	187000 J/kg
Particle diameter	0.01905 m
Bed volume	650 m^3
Bed height	7.376 m

Table 9 provides a breakdown of the energy recovered from the filler and HTF, and also includes the potential storage capacity of the filler material, Q_{bedMax}, for each case. The $\mathrm{LHS}_{\mathrm{high}}$ system reached steady state after 4 cycles and at this point, the system consistently discharged 104.68 MWh within 206 minutes and completely charged within 182 minutes. Of this energy, 81.8 MWh was extracted from the PCM and the remaining was due to the storage capacity of the HTF. Alternatively, $\mathrm{LHS}_{\mathrm{low}}$ system reached steady state after 3 cycles, consistently discharging 103.39 MWh within 177 minutes and completely charging within 238 minutes. Of the total energy discharged, 83.89 MWh was recovered from the PCM, and the remaining from the HTF. The SHS system achieved steady state in 10 cycles, at which point it reached the charging and discharging threshold temperatures in 164 and 161 minutes, respectively, and discharged 93.0 MWh. This exceeds the maximum potential storage capacity of the storage media due to the fact that the HTF contributed 24.3 MWh to the energy output. The maximum potential storage capacity of the HTF is 30.3 MWh, which is based on a temperature differential defined between $T_{HTF,h}$ and $T_{HTF,c}$.

Table 9. Division of recovered energy from each storage system, and total potential storage capacity.

	$E_{dischargedPCM}$ (MWh)	$E_{dischargedHTF}$ (MWh)	Total $E_{discharged}$ (MWh)	Q_{bedMax} (MWh)
SHS system	68.73	24.31	93.04	81

Table 9 (continued)

LHS$_{high}$ *system*	*81.84*	*22.84*	*104.68*	*147*
LHS$_{low}$ system	83.89	19.51	103.39	147

Table 10 lists the performance indicators of each system for the first cycle while Table 11 provides the same indicators for the steady state cycle. All systems achieve overall exergy efficiencies greater than 95% at steady state. The net exergy supplied during the charging process is high during the first cycle since the systems initially charge for a long period of time in order to establish the baseline energy that remains in the system throughout cyclic operation. As such, the first cycles exhibit lower exergy efficiencies than the steady state cycles. Though the LHS systems discharge more energy, they only utilize slightly more than half of their potential storage capacity. Of this, 10.7% of the recovered energy is due to latent heat in the LHS$_{high}$ system, and 17.2% is due to latent heat in LHS$_{low}$ system. Discharging efficiency would be a synonymous metric to gauge utilization of the stored energy, however it includes the storage capacity of the HTF in addition to the filler media. Since the HTF has a high volumetric heat capacity, it has a strong contribution to the stored energy and skews the utilization due to PCM alone.

Table 10. First cycle performance values.

Performance metric	*SHS system*	*LHS*$_{high}$ *system*	*LHS*$_{low}$ *system*
$\eta_{II,overall}$	0.915	0.972	0.597
Capacity ratio	0.951	0.564	0.987
Utilization ratio	0.870	0.557	0.572

Table 11. Steady state cycle performance values.

Performance Metric	*SHS system*	*LHS*$_{high}$ *system*	*LHS*$_{low}$ *system*
$\eta_{II,overall}$	0.991	0.979	0.961
Capacity ratio	0.937	0.564	0.987
Utilization ratio	0.849	0.558	0.571

As was illustrated in Figure 4 of chapter 1, the architecture of the LHS thermocline zone consists of two sub-zones, i.e. a phase change region, and a sub-solidus sensible heat region. Equations 6 and 7 described the relationship between the movement of the phase change front in relation to the latent heat and solidus/liquidus temperatures of the PCM during charging and discharging. When the charging and discharging cut-off temperature are induced, the phase transition temperature has a conflicting effect on the charging and discharging processes. Before discussing this effect, the heat transfer mechanism in a SHS system is first evaluated.

In Figure 31, the axial temperature profile of the SHS material and HTF is plotted with the degree of thermal non-equilibrium, or temperature difference between both media, at different charging states. As is illustrated and expected, thermal non-equilibrium exists in the thermocline zone and is negligible in the hot and cold zones. At the onset of charging, a large temperature difference exists between filler material and HTF at the top of the bed, resulting in an elevated degree of thermal non-equilibrium (not shown in figure). As the central region of the thermocline advances down the bed, it enters a region that was pre-heated by the lower region of the thermocline, therefore the degree of thermal non-equilibrium gets progressively smaller over time and the rate of heat transfer decreases, causing the thermocline zone to widen. Eventually the thermocline exits the bed, inducing a saturation condition.

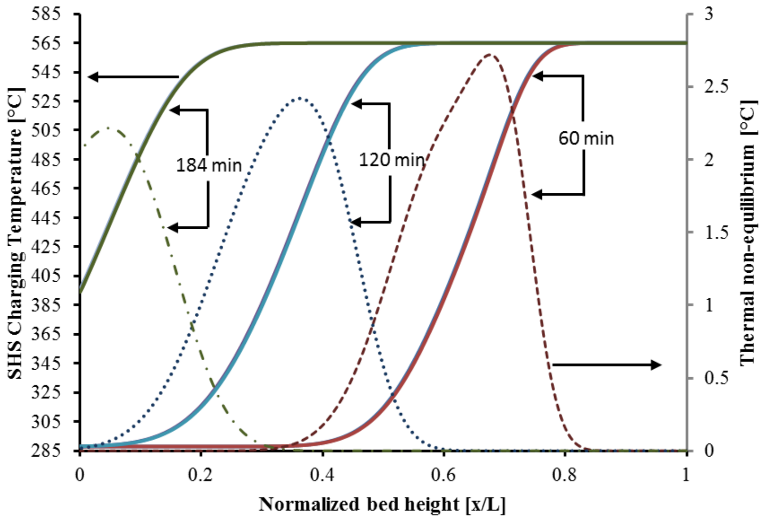

Figure 31. Advancement of the thermocline and concomitant progression of thermal non-equilibrium during charging in the SHS system. HTF and storage media temperature are indistinguishable in the plot. The thermocline travels from the normalized bed height of 1 at the onset of charging, to 0 as charging terminates.

The mechanism of heat transfer in a latent heat storage system differs due to the nearly constant temperature phase change process. Throughout charging mode in a LHS system, there lies an elevated region of thermal non-equilibrium that resides at the interface of the hot zone and the phase change zone. This is identified as the pinch point interface in Figure 32b due to its systemic effect. As the HTF enters the system, it approaches a region of the bed that is at the phase change temperature, and the temperature difference between the two media promotes a high degree of heat transfer. At this juncture, the HTF supplies energy to the PCM, but is limited by the second law of thermodynamics which requires that the HTF remains above the PCM temperature to maintain a positive driving force for heat transfer. After exchanging energy with the PCM, the HTF then exits the interface near the phase transition temperature and continues to flow down the bed, preheating the downstream capsules to the phase transition temperature. This establishes the phase change zone. As time progresses, the HTF continues to exit the interface at the phase transition temperature. There is no longer a driving force for heat transfer, therefore the phase change zone serves as a pinch point region. In cascaded systems, the pinch point region shifts along the vertical axis of the bed and does not necessarily coincide with the phase change process, therefore the phase change zone will be referred to as the pinch point zone.

The travel rate of the pinch point interface during charging mode can be characterized with Equation 6 in chapter 1, which is repeated here for convenience:

$$v_{latent,ch} = \frac{C_{p,HTF,h}\rho_{HTF,h}U}{\varepsilon C_{p,HTF,h}\rho_{HTF,h}+(1-\varepsilon)C_{p,s,h}\rho_{s,h}[1+\frac{1}{Ste}\left(\frac{T_{h,HTF}-T_{c,HTF}}{T_{h,HTF}-T_{solidus,PCM}}\right)]} \tag{6}$$

The equation defines the following conditions that affect the movement of the pinch point interface:

1.) The interface travel rate increases with increasing difference between the solidus temperature and inlet HTF temperature, i.e. a lower melting point PCM is more favorable during the charging process.

2.) The pinch point travel rate increases with decreasing Inverse Stefan number, i.e. decreasing latent heat of fusion.

The effect of melting point is illustrated in Figure 32, which provides the first charging cycle's axial temperature profile of both LHS systems as well as the SHS system for comparison. The system of Figures 32a and 32b consists of the PCM that melts at 515°C, whereas the PCM in the system of Figures 32c and 32d melts at 395°C. As can be seen by comparing the top and middle figures, the lower melting point reduces the severity of the pinch point problem by enabling a higher degree of heat transfer at the interface. At 120 minutes of charging, the pinch point interface of the $\mathrm{LHS}_{\mathrm{low}}$ system has traveled further down the bed than the $\mathrm{LHS}_{\mathrm{high}}$ system, and the pinch point region is shorter. Since the lower melting PCM exhibits a phase transition temperature that falls below the charging threshold value, the system can charge for a long period of time before the saturation condition is met. This enables the system to exploit a large portion of the storage capacity, as is demonstrated at the final charging state in Figure 32d. The final temperature profiles at steady state look similar to the final temperature profiles of the first cycle.

The pinch point phenomenom is exacerbated by a high latent heat value. Figure 33 provides different charging states of the first cycle for four systems of melting point equivalent to that of the $\mathrm{LHS}_{\mathrm{high}}$ system, yet differing latent heat values. The sub-solidus front moves at the same velocity for each system. Since charging terminates when the sub-solidus front exits the bed, its movement defines the charging time, which is nearly equivalent for all four systems in this case. What differs is the movement

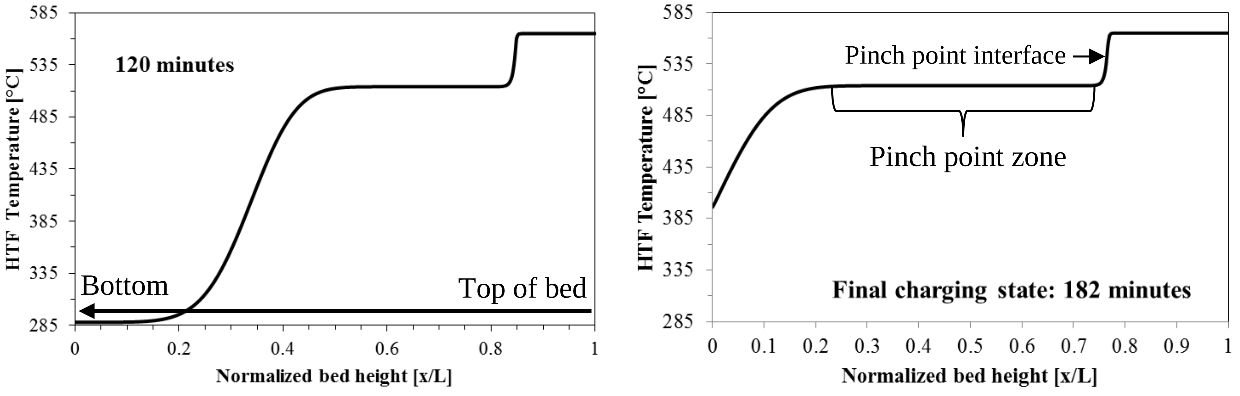

a. b.

Figure 32. Axial HTF temperature profile for different states of the first charging cycle. In (a) and (b), the PCM melting point is 515°C, and in (c) and (d) the PCM melting point is 395°C, which falls below the charging cut-off temperature. The axial temperature profile of the SHS system is provided in (e) and (f).

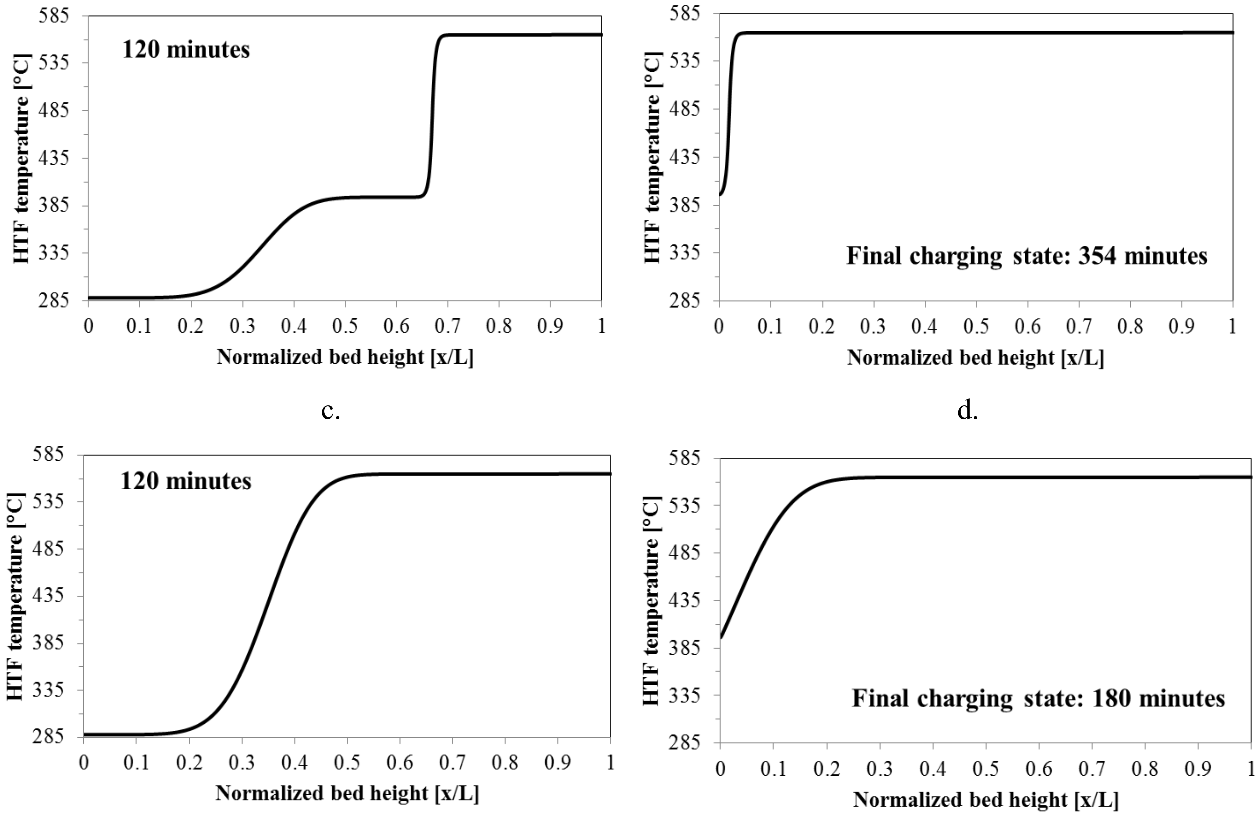

c. d.

e. f.

Figure 32 (continued)

of the pinch point interface. In the systems exhibiting low latent heat, the interface moves faster down the bed as less time and energy are needed for complete melting of the PCM. As such, a larger fraction of the bed has reached the inlet HTF temperature and is characterized by a higher exergy state. This is reflected in the outlet temperature during the discharging process, as demonstrated in Figure 34 for the steady state discharging cycle.

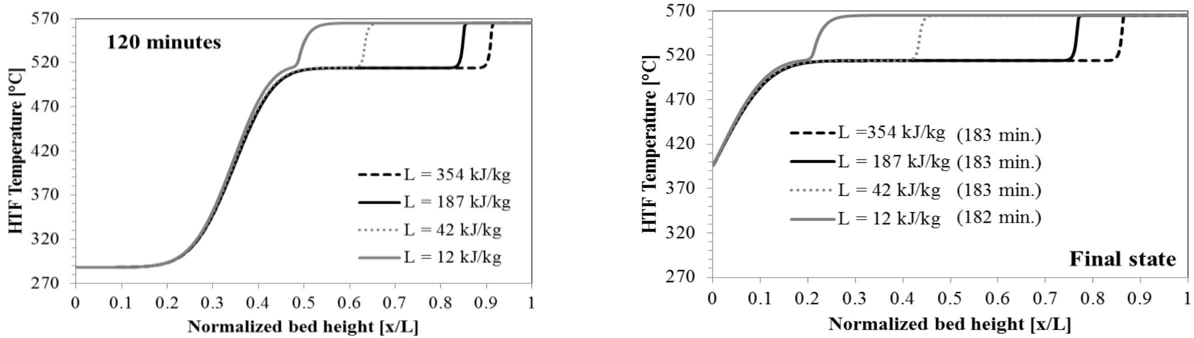

a. b.

Figure 33. Axial HTF temperature profile of systems with varying latent heat. The first charging cycle is depicted for a) 120 minutes, and b) the final charging state. Final charging time is included in parenthesis.

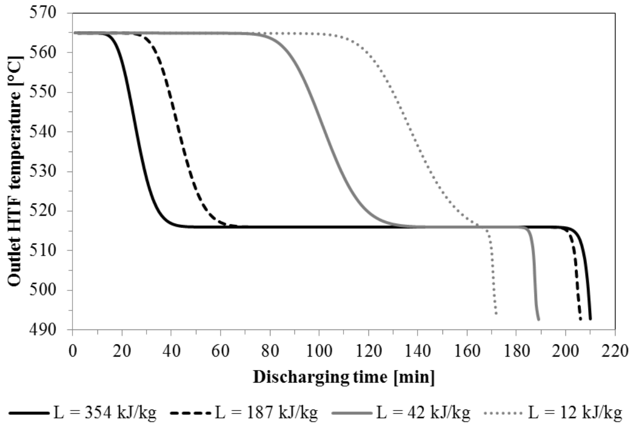

Figure 34. Outlet HTF temperature as a function of time for four systems of varying latent heat and a melting temperature of 515°C. The temperature profile is provided for the steady state discharging cycle. As latent heat decreases, discharging time similarly decreases, yet the HTF exits at the high operating temperature for a longer period of time.

During charging mode, a high phase transition temperature results in a lengthening pinch point region that serves as a bottle neck in heat transfer. During discharging however, the high phase transition temperature has the opposite effect. Equation (7) describes the velocity of the phase change front during the discharging process. It indicates that the front moves at an increasingly faster rate as the difference between liquidus temperature and inlet HTF temperature grows.

$$v_{latent,dch} = \frac{C_{p,HTF,h}\rho_{HTF,h}U}{\varepsilon C_{p,HTF,h}\rho_{HTF,h} + (1-\varepsilon)C_{p,s,h}\rho_{s,h}\left[1+\frac{1}{Ste}\left(\frac{T_{h,HTF}-T_{c,HTF}}{T_{liquidus,PCM}-T_{c,HTF}}\right)\right]} \tag{7}$$

Faster movement of the phase change front is advantageous in that it enables a higher degree of energy depletion before discharging terminates. Therefore the high phase transition temperature provides an advantage in heat transfer during the discharging process. Latent heat has the same effect for both charging and discharging, i.e. an increase in latent heat reduces the velocity of the phase change front. When combined with the charging process, this is not necessarily a shortcoming. The large thermal inertia of a high latent heat value serves as a buffer, stalling movement of the sub-solidus front before it reaches the top of the system and terminates the discharging process.

To illustrate the effect of phase transition temperature on the system's behavior, Figure 35 provides the final charging axial temperature profile for systems in which the melting point falls below the charging cut-off temperature and above the discharging cut-off temperature. To summarize system behavior during the charging process:

1.) When the melting point falls below the charging cut-off temperature, the pinch point interface can travel down the full length of the bed before the saturation condition is met. A large fraction of the system is able to exploit its latent heat capacity and store energy at $T_{HTF,h}$, which is the maximum potential exergy state.
2.) When the melting point lies above the discharging cut-off temperature, slow movement of the pinch point interface results in a long pinch point zone and a short hot zone. Therefore, when the saturation condition is met, a small fraction of the bed has reached the hot HTF temperature, and a large percentage of the particles remain in the phase change process.

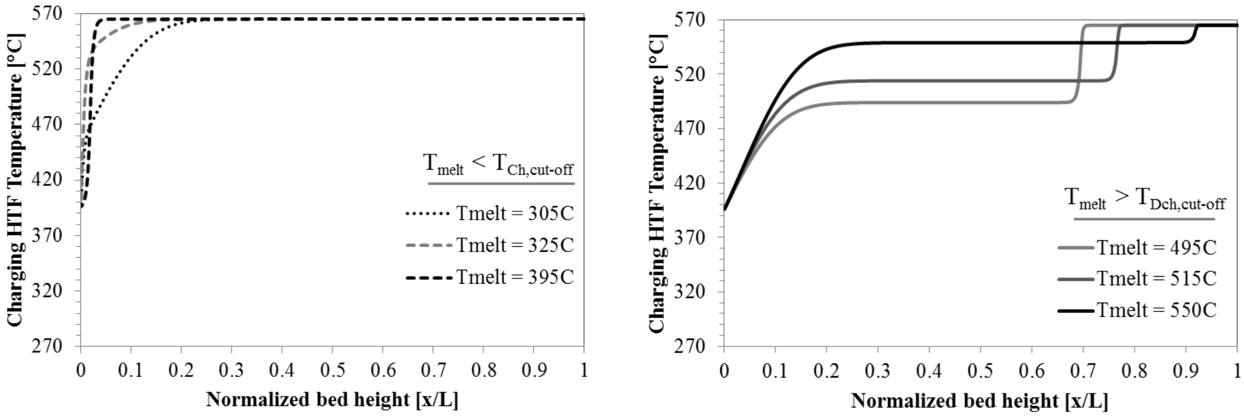

a. b.

Figure 35. Effect of melting temperature on the final charging state of a single-PCM system. (a) provides the final axial HTF temperature profile when the melting temperatures fall below the charging threshold value. (b) provides the final axial HTF profile when the melting temperatures lie above the discharging threshold value.

Figure 36 provides the same information as Figure 35, but for the final discharging state. The systems are able to recover the energy that is above the discharging threshold value, therefore the following trends are observed:

1.) When the phase change temperature falls below the charging cut-off temperature, the system utilizes all of the energy at the maximum exergy state, yet does not recover all of the latent heat.

2.) When the phase change temperature lies above the discharging cut-off temperature, the system can recover a large fraction of the stored energy, including latent heat. The degree of energy depletion is significantly high.

An ideal system would exhibit the final charging state of the low melting PCMs, in which most of the system reaches the hot inlet temperature, and would exhibit the final discharging state of the high melting PCMs, in which nearly all of the stored energy is extracted.

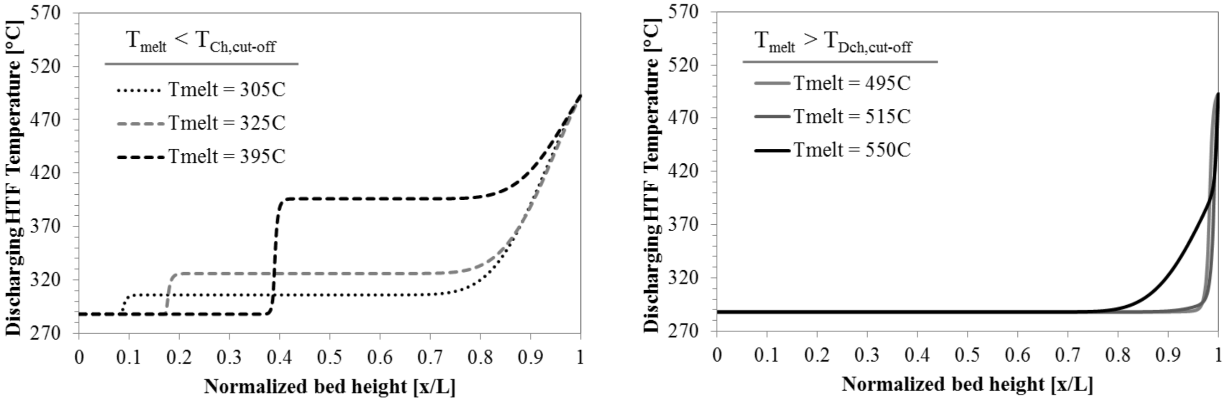

a. b.

Figure 36. Effect of melting temperature on the final discharging state of a single-PCM system. (a) provides the final axial HTF temperature profile when the melting temperatures fall below the charging threshold value. (b) provides the final axial HTF profile when the melting temperatures lie above the discharging threshold value.

Figure 38 depicts the resulting outlet HTF temperature as it discharges from the system with time for four systems of different melting points. Important to note is that the temporal variation in outlet temperature affects the recovered energy and exergy in differing ways. From a perspective based purely on energy, the trends lead to the results of and Nithyanandam and Pitchumani [35], which demonstrated that energy output increases as the melting point increases from the low operating system temperature to the charging threshold value (i.e. from $T_{HTF,Dch}$ to $T_{ch,cut-off}$) and also increases as the melting point decreases from the high operating system temperature to the discharging threshold value (i.e. from $T_{HTF,Ch}$ to $T_{dch,cut\text{-}off}$). This is depicted in Figure 37, which displays the nondimensional energy output for systems of the same charging and discharging cut-off temperature as the current study. The useful energy was evaluated under three different Reynolds numbers, which are represented by the solid and dashed lines.

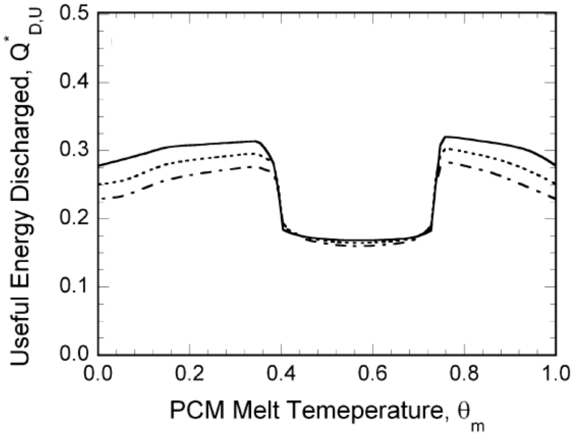

Figure 37. Dimensionless useful energy discharged versus normalized melt temperature for the system under evaluation in Nithyanandam and Pitchumani [35]. The normalized charging and discharging cut-off temperatures are 0.39 and 0.74. The three curves represent useful energy discharged under different Reynolds numbers. (Copyright permission is included in Appendix C).

The quality of energy, or exergy, strongly differs however, when the melting point is less than the charging threshold value as opposed to when it is above the discharging threshold. In the former case, the outlet temperature is primarily at the maximum exergy state before diminishing to the discharging threshold value. In the latter case, the HTF exits the bed at the high exergy state for a short period of time before reducing to the melting temperature, which is a shift to a lower exergy state throughout most of the process. For example, Table 12 provides the discharging time as well as the energy and exergy discharged from the LHS_{high} and LHS_{low} systems. The discharging time for the LHS_{high} system is 16% higher than the LHS_{low} system, and provides a 1.2% increase in energy output. On the other hand, the LHS_{high} system recovers less exergy than the LHS_{low} system. In the plant level study of Flueckiger and Garimella [5], it was demonstrated that the benefit of LHS systems over SHS packed bed systems is only realized when the melting point is below the charging cut-off temperature. The annual plant capacity factor was enhanced and the thermal energy discard was reduced for these cases. Though a high phase transition temperature allows the system to discharge for a longer period of time before the cut-off criteria is prompted, the reduced quality of energy dictates that the turbine operates at partial load conditions, leading to less power production when compared to systems of low phase transition temperature. Low phase transition temperature systems are also able to charge for extended periods of time before the saturation condition is induced, therefore they additionally benefit from reduced thermal energy discard.

Table 12. Total energy and exergy recovered, and discharging time for the packed bed systems.

	Total Energy$_{discharged}$ (MWh)	*Total Exergy$_{discharged}$ (MWh)*	*Discharge time (min)*
SHS system	93.04	52.98	161
LHS$_{high}$ system	104.68	58.66	206
LHS$_{low}$ system	103.39	58.92	177

The above analysis explores the performance and behavior of SHS and LHS packed bed systems and exemplifies that they can both achieve high overall exergy efficiencies. Though the LHS systems exhibit greater potential in storage capacity, they cannot fully harvest this capacity due to the limitation in heat transfer caused by the pinch point phenomenon. LHS systems can provide more energy than a SHS system of equivalent tank size, however the phase change temperature must be judiciously chosen to ensure that the exergy exceeds that of the SHS system in order to achieve a gain in plant output. When threshold values are implemented, this is realized through the use of low melting point PCMs, which discharge energy at the high exergy state for a longer time period than the SHS packed bed system. This is demonstrated in Figure 39. One shortcoming of SHS packed bed systems is the presence of the thermocline zone, which reduces the system's ability to utilize its maximum potential capacity. Figure 33f provided the final charging state of the SHS packed bed system. At steady state, only 72% of the system could be used to store energy at the high operating temperature, the thermal gradient occupying the remaining fraction of the bed. In comparison, Figure 33d demonstated that 96% of the low phase change temperature system stored energy at the high exergy state. Thus one can see that an advantage of the LHS system over the SHS system is not just the added storage capacity due to latent heat, but its ability to store more energy at the high exergy state.

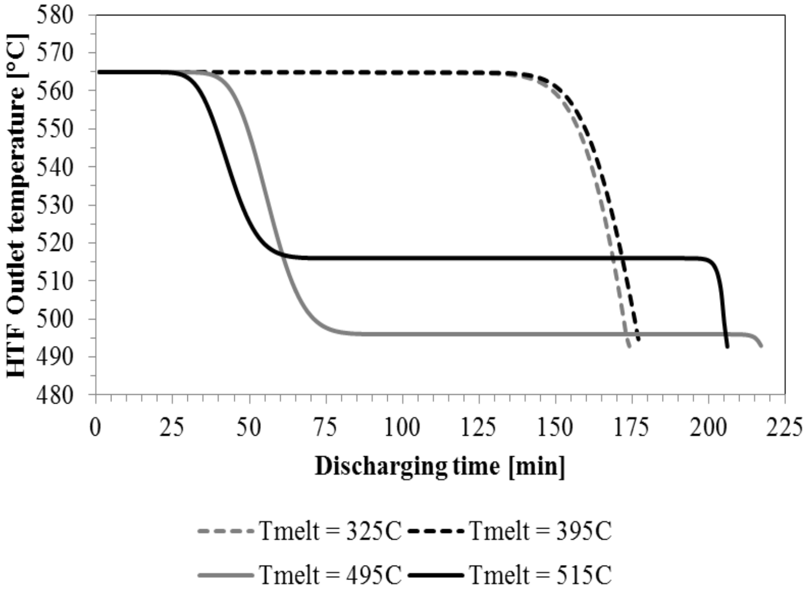

Figure 38. Steady state discharging outlet HTF temperature as a function of time. Shown are two systems in which the PCM melting temperature falls above the charging threshold value and for two systems in which the melting temperature lies above the discharging threshold value.

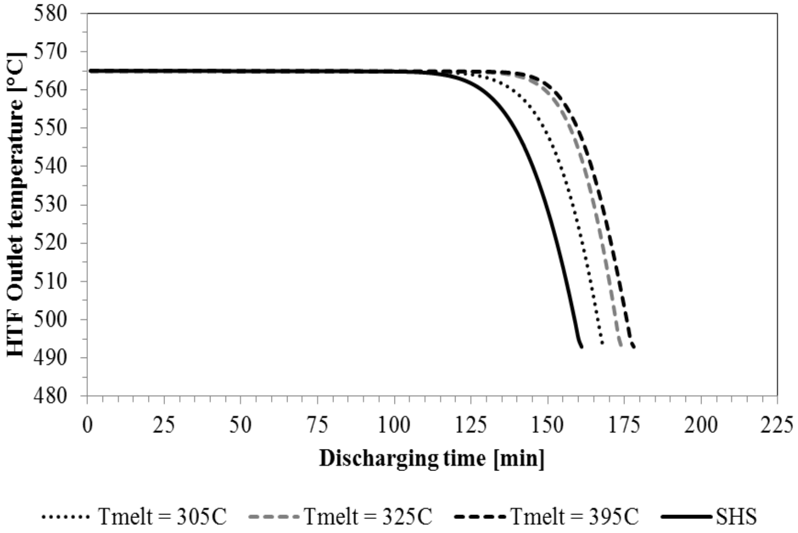

Figure 39. Steady state HTF temperature discharged over time. The dashed lines represent the temperature exiting the system when the PCM melting point is less than the charging threshold value and the solid line represents the HTF outlet temperature profile for the SHS packed bed system.

3.3.2 Analysis 2: Cascaded LHS System Study

Previous publications have emphasized the thermodynamic benefit of a cascaded latent heat storage system design [5, 70-73], wherein multiple PCMs are stacked in series with melting points that decrease with increasing distance from the charging inlet. This phase change temperature sequence ensures optimum performance by facilitating a good thermal match between HTF and PCM, and by minimizing the loss of exergy from the bed outlet [70]. Similar to the single PCM case, the melting points of the cascaded system must also fall below and above the charging and discharging cut-off temperatures respectively, to maximize utilization [5]. An additional constraint, as was demonstrated in Flueckiger and Garimella [5], is the application of a small disparity between the phase change temperatures of the top and bottom layers of a three PCM system, while still maintaining the aforementioned constraint. The merit of this configuration is a large gain in plant capacity factor when compared to other melting point arrangements and compared to sensible heat packed bed storage.

Not only is the sequence of phase change temperature important, but the progression of latent heat can additionally impact performance. An increase in latent heat does not improve the overall exergetic efficiency when the latent heat of all PCMs are augmented equally [70, 74]. Adebiyi et al. [70] concluded however, that the PCM at the bottom of the charging outlet in a three PCM system should have the lowest melting point and highest latent heat to achieve optimum thermodynamic efficiency of high-temperature LHS systems.

In Analysis 1, it was demonstrated that the second law efficiency did not fluctuate notably between cases, albeit the deviation between recovered energy and exergy during the discharging process was significant. Therefore thermodynamic efficiency does not necessarily coincide with an optimally designed system. In the plant level study of Nithyanandam and Pitchumani [68], for any given tank height it was shown that both the capacity factor and total energy recovered from the system increased with decrease in particle diameter. The same progression was not observed with overall annual exergy efficiency, i.e. the trend in performance did not equate to the trend in output. In Shabgard et al. [73], single PCM thermosyphon heat pipe systems were compared to a three PCM system in the 280 – 390°C temperature range. The authors found that the single PCM system with the lowest melting point exhibited the highest exergy efficiency, yet the cascaded system recovered more exergy during a charging-discharging cycle, again emphasizing that the output does not necessarily follow the same trend as performance.

In selecting PCMs for a cascaded system, several scenarios are possible. The succeeding studies evaluate a combination of hypothetical PCMs in a cascaded design under the premise that the optimal configuration is not based on efficiency alone. Though Adebiyi et al. [70] asserted that the lowest melting PCM should have the largest latent heat based on second law efficiency, this is investigated in the following analysis for a 2-PCM system and 3-PCM system. The goal is to understand if there is a combination of PCMs that would induce an energy output penalty rather than an improvement when compared to the nominal case of a single PCM. The thermal properties and packed bed characteristics of the LHS system of Analysis 1 are employed in order to compare the cascaded systems to the baseline case. In each study, the PCM closest to the charging inlet is referred to as the top PCM and that closest to the charging outlet is referred to as the bottom PCM.

Before studying the cascaded systems parametrically, the mechanism for enhanced energy storage and recovery with multiple PCMs is discussed. A single PCM, 2-PCM, and 3-PCM system are compared, all having the same potential storage capacity of 146.8 MWh, and system characteristics defined in Table 8. The following three cases are evaluated:

1.) The single-PCM LHS_{high} case, which assumes the phase change temperature and latent heat of the $NaCl/K_2SO_4$ eutectic. The values of this baseline case are 515°C and 187000 J/kg.
2.) A 2-PCM system in which each PCM occupies half of the bed and both are assigned the same latent heat of 187000 J/kg. The melting point of the top PCM corresponds to the eutectic, and the bottom PCM was assigned a normalized melt temperature of 0.25 (T_{melt} = 357.25°C).

3.) A 3-PCM cascade wherein each PCM occupies 1/3 of the bed and all are assigned the same latent heat as the baseline 1-PCM case. The same melting points of the 2-PCM system are assumed for the top and bottom PCM. A normalized melt temperature of 0.50 (T_{melt} = 426.5°C) is assigned to the middle PCM.

Figure 40 provides the temporal progression of the axial HTF temperature profile for the 1,2, and 3-PCM cases during charging mode of the first cycle. At 60 minutes of charging, all three temperature profiles are equal. When multiple PCMs are employed, melting initiates as the sub-solidus sensible heat zone approaches a new cascade. As discussed in Section 3.3.1, a high rate of heat transfer occurs at the pinch point interface and the HTF leaves the interface at a temperature that draws near the phase transition temperature. In a cascaded system, each lower cascade can take advantage of that incoming low exergy flow stream to accelerate the phase change process, promoting greater usage of latent heat as well as sensible heat. Rather than one high heat transfer region at the pinch point interface as in the single PCM case, the cascaded systems exhibit several regions of thermal non-equilibrium, depending on the number of cascades, and each of these regions stimulates a high degree of heat transfer.

At 180 minutes, the lengthening pinch point of the single PCM case mandates that most of the PCM remains in the process of changing phase, and shortly thereafter the charging cut-off temperature is met. In the remaining two cases, the low melting PCM serves as a buffer by inhibiting the saturation condition. At 240 minutes for the 2-PCM case, the top pinch point zone has lengthened into the bottom PCM cascade, and a fraction of the top PCM remains in the phase change process. On the other hand, it is at this time that the top PCM in the 3-PCM system is completely molten, allowing the pinch point interface to collapse. With this event, the hot zone is free to move at a higher velocity through the bed, as illustrated in the final charging time figure, which shows that more than half of the bed in the 3-PCM system has reached the hot inlet temperature. When a low melting PCM is adopted, as in the single-PCM LHS_{low} system, the large temperature difference between the hot inlet HTF and the phase transition temperature provides a large driving force for heat transfer, fostering rapid movement of the pinch point interface. Under this condition, the pinch point interface is not necessarily an impediment in storage utilization. When the melting point is high however, as in the top PCM of the 2-PCM and 3-PCM system, the pinch point interface travels slowly down the bed, curbing growth of the hot zone. Since the 3-PCM system has a lower fraction of the high melting PCM, it completes the melting process before charging terminates, allowing the pinch point interface to break down.

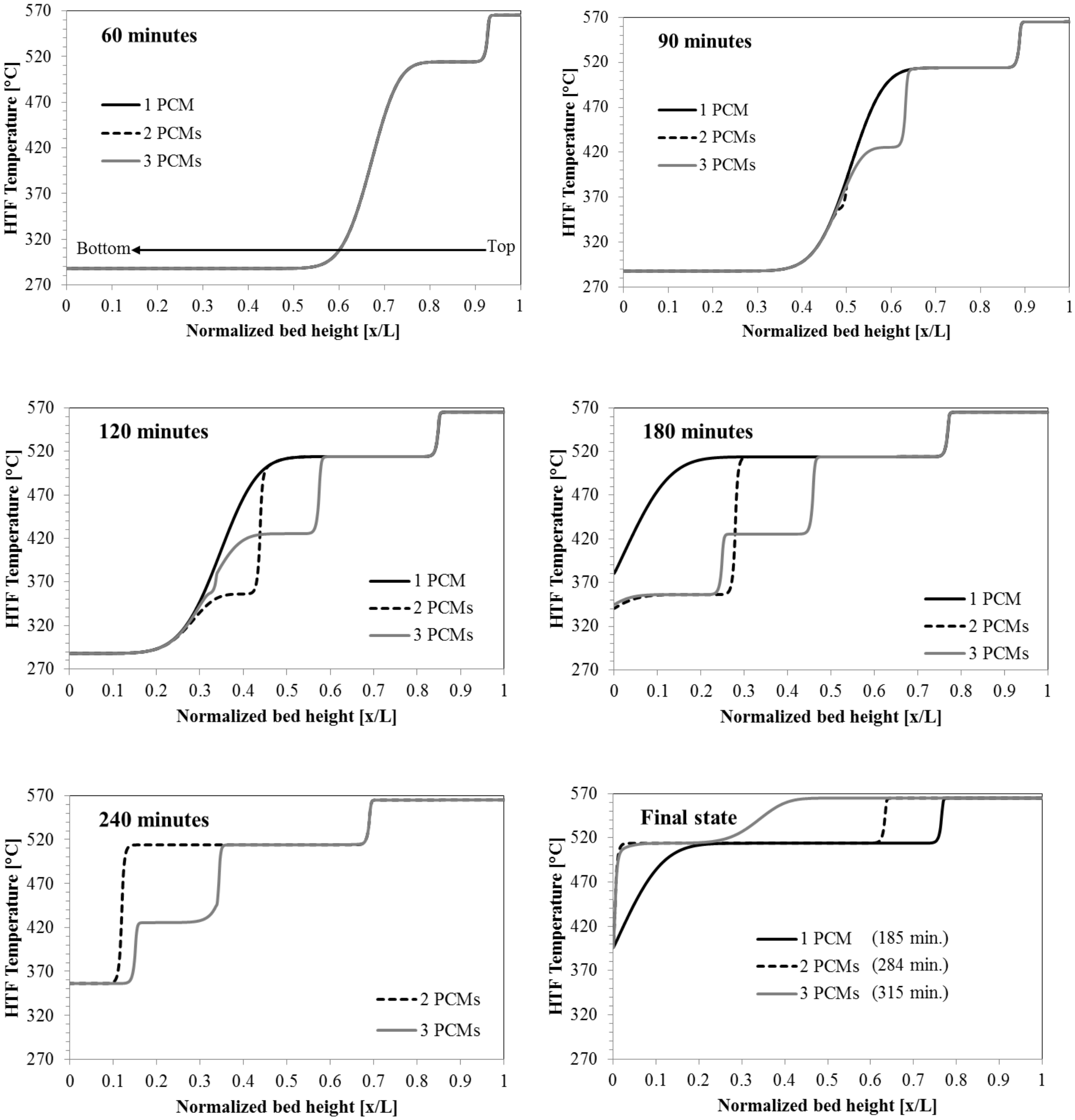

Figure 40. Comparison of charging axial temperature profile of a single-PCM, 2-PCM, and 3-PCM cascade with equivalent storage capacity and latent heat.

To enable a direct comparison of the above three cases, Table 13 provides their performance profile. The use of three PCMs facilitates greater utilization of the potential storage capacity and enhanced energy and exergy output, however the overall exergy efficiency is highest for the single PCM case.

Table 13. Steady state characteristics of each case assessed for the 1, 2, and 3-PCM comparison. All three cases have the same potential storage capacity of 146.8 MWh.

#PCMs (Case #)	t_{Ch}/t_{Dch} (min)	$E_{Discharged}$ (MWh)	$Ex_{Discharged}$ (MWh)	Capacity Ratio	Utilization Ratio	$\eta_{ExOverall}$
1	182/206	104.7	58.7	0.564	0.558	0.979
2	258/244	125.1	70.2	0.859	0.729	0.955
3	292/285	149.1	83.9	0.948	0.883	0.966

3.3.2.1 Two-PCM Cascaded System

Three sets of analyses are conducted for the two-PCM system parametric study. Aside from varying the latent heat, the effect of the PCM volume fraction is investigated. The first analysis assumes that the latent heat is equivalent for both PCMs in order to isolate the impact of volume fraction. The melting points are based on the results of Analysis 1 of section 3.3.1. The objective is to select values that maximize storage and enable complete recovery of energy at the high exergy state. As previously mentioned, the top PCM must be greater than the discharging cut-off temperature ($T_{Dch,cut\text{-}off}$ = 493°C/ $\theta_{Dch,cut\text{-}off}$ = 0.74). As the melting point decreases, the pinch point interface can travel at a higher rate down the bed, lengthening the hot zone; therefore the top PCM would also benefit by being furthest from the inlet HTF temperature. Thus the top PCM phase transition temperature was selected as 495°C, which lies just above the discharging cut-off value and corresponds to a normalized melt temperature of 0.747.

The bottom PCM should be less than the charging threshold value of $T_{Ch,cut\text{-}off}$ = 396°C ($\theta_{Ch,cut\text{-}off}$ = 0.39). When the melting point was slightly less than this temperature, 96% of the bed reached the high exergy state, hence a melting point of 395°C was selected for the bottom PCM. This corresponds to a normalized melt temperature of 0.386. The latent heat of both PCMs was assigned the same value as the

NaCl/K_2SO_4 eutectic, which is 187000 J/kg and corresponds to an Inverse Stefan number of 0.64. Figure 41 illustrates the division of PCM volume for the cases under study.

The second and third analyses examine the effect of latent heat on the systems of the first analysis. The second analysis assigns a high latent heat to the bottom PCM and the third analysis assigns a high latent heat to the top PCM. The high latent heat was arbitrarily chosen as twice the value of the eutectic. All other conditions remain the same as in the first analysis. Table 14 provides the conditions of each case.

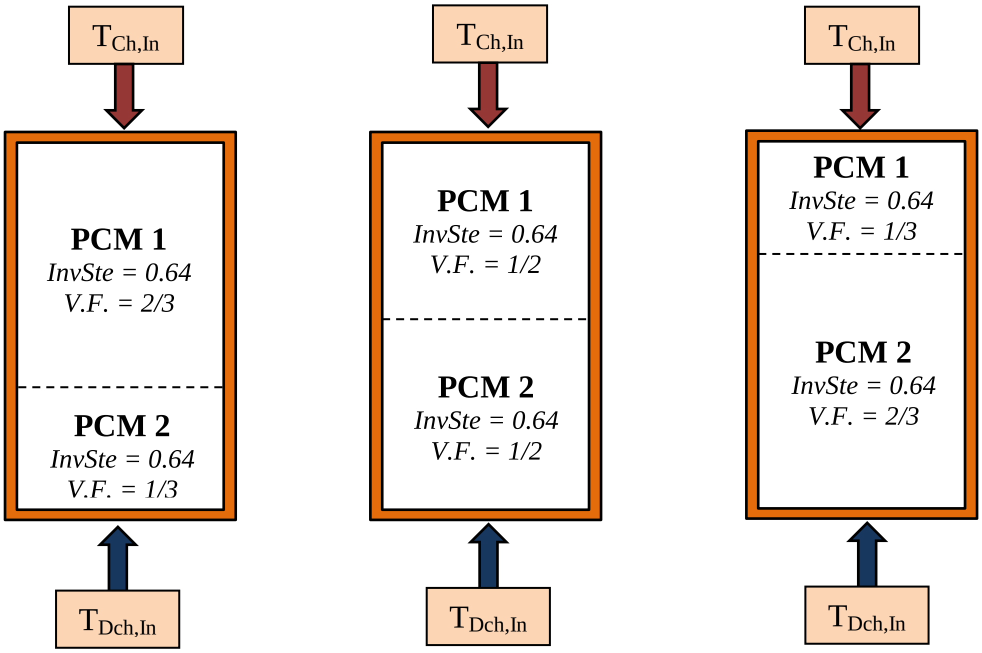

Figure 41. Schematic illustrating the division of PCM volume fraction (*V.F.*) for the cases evaluated in cascade analysis 1. A tank volume of 650 m^3 and tank diameter of 10.593 m is used for each case.

Table 14. Assigned volume fraction, latent heat, and phase change temperature for the cases assessed in the 2-PCM cascade system study.

Analysis #	Case #	*Top PCM* ($\theta_{melt} = 0.747$) InvSte	Top PCM Fraction Occupied	*Bottom PCM* ($\theta_{melt} = 0.386$) InvSte	Bottom PCM Fraction Occupied
1	1	0.64	2/3	0.64	1/3
	2	0.64	1/2	0.64	1/2
	3	0.64	1/3	0.64	2/3

Table 14 (continued)

2	4	0.64	2/3	1.28	1/3
	5	0.64	1/2	1.28	1/2
	6	0.64	1/3	1.28	1/3
3	7	1.28	2/3	0.64	1/3
	8	1.28	1/2	0.64	1/2
	9	1.28	1/3	0.64	2/3

Table 15. Steady state system output and performance indicators for the cases of PCMs with equivalent latent heat.

Case #	t_{Ch}/t_{Dch} *(min)*	$E_{Discharged}$ *(MWh)*	$Ex_{Discharged}$ *(MWh)*	*Capacity Ratio*	*Utiliz. Ratio*	$\eta_{ExOverall}$	Q_{bedMax} *(MWh)*	$t_{T\geq 99\%}$ *(min)*
1	285/292	142.64	79.62	0.837	0.824	0.960	146.8	72
2	331/317	159.34	89.27	0.947	0.930	0.960	146.8	105
3	340/283	150.42	84.85	0.987	0.882	0.959	146.8	151

Table 16. Steady state characteristics of 2-PCM cascade systems which assume a high latent heat in the bottom PCM.

Case #	t_{Ch}/t_{Dch} *(min)*	$E_{Discharged}$ *(MWh)*	$Ex_{Discharged}$ *(MWh)*	*Capacity Ratio*	*Utiliz. Ratio*	$\eta_{ExOverall}$	Q_{bedMax} *(MWh)*	$t_{T\geq 99\%}$ *(min)*
4	279/356	175.33	97.98	0.935	0.920	0.948	168.7	99
5	387/330	171.28	96.35	0.891	0.834	0.955	179.7	149
6	367/284	150.90	85.13	0.986	0.700	0.950	190.7	152

Table 17. Steady state characteristics of 2-PCM cascade systems which assume a high latent heat in the top PCM.

Case #	t_{Ch}/t_{Dch} *(min)*	$E_{Discharged}$ *(MWh)*	$Ex_{Discharged}$ *(MWh)*	*Capacity Ratio*	*Utiliz. Ratio*	$\eta_{ExOverall}$	Q_{bedMax} *(MWh)*	$t_{T\geq 99\%}$ *(min)*
7	285/304	142.80	79.30	0.659	0.645	0.956	190.7	41
8	332/341	160.51	89.16	0.798	0.783	0.953	179.7	49
9	380/363	178.17	99.52	0.946	0.928	0.955	168.7	93

The performance indices and system output of cases 1 - 3 are provided in Table 15. The steady state charging time, discharging time, recovered energy, and recovered exergy during the discharging process are given. The table also supplies the time period in which the HTF exits the system at a high exergy state, denoted as $t_{T\geq 99\%}$. This is deemed a value greater than or equal to 99% of the hot system operating temperature, therefore HTF exiting the system between 565°C and 560°C is categorized as energy recovery at the high exergy state. All configurations show a gain in energy and exergy output when compared to the single PCM cases and the SHS packed bed case. The configuration in which each PCM occupies half of the volume fraction (case 2) results in the highest energy output of 159.34 MWh, a 71.3% increase over the SHS packed bed system.

Figure 42 provides the HTF exit temperature as a function of time for all three cases. The figure illustrates that the volume fraction has a significant impact on the distribution of recovered energy. As the volume fraction of bottom PCM increases, the high exergy recovery time increases. As was discussed in the previous section, the top PCM must be completely molten before the pinch point interface can collapse, allowing the hot zone to proceed down the bed. Therefore less top PCM facilitates greater storage at the hot operating temperature. Alternatively, the bottom PCM serves as a buffer, staving off the saturation condition. Thus increasing the volume fraction of the bottom PCM while decreasing that of the top PCM allows the system to charge for a longer time period and recover more energy at the higher exergy state. Though case 2 produces the highest energy output, when compared to case 3 it exhibits a 44% reduction in time in which the HTF exits the system at the high exergy state.

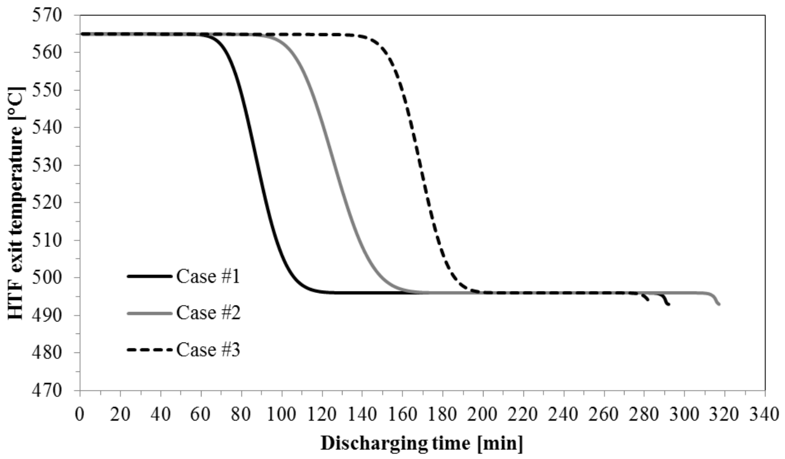

Figure 42. Temporal progression of the HTF exit temperature for cases 1 through 3 of the 2-PCM cascade.

This analysis demonstrates that an advantage of the 2-PCM cascade is the extended energy output at the top PCM melting temperature. The system with the greatest fraction of bottom PCM (case 3) releases HTF at the high exergy state in the same time frame as a single-PCM system consisting purely of the bottom PCM. The 2-PCM system benefits however, by the subsequent release of HTF at the melting temperature of the top PCM, which can be used to produce electricity under partial load conditions. Therefore the 2-PCM system of case 3 benefits from a 45.5% increase in energy output over the single-PCM system and a 61.7% increase above the SHS packed bed system. Cases 1 through 3 are able to recover approximately 96% of the net exergy that enters the system, as demonstrated by their overall exergy efficiency.

Table 16 provides the system characteristics of the 2-PCM cascade for the scenario wherein the highest latent heat is exhibited in the bottom PCM. Similar to the above scenario, the advantage of a large volume fraction of low melting PCM is manifested as an increase in high exergy recovery time, as demonstrated in Figure 43. The augmented latent heat in the bottom PCM enhances the system’s ability to store and release more energy, however the degree of the gain decreases as the fraction of bottom PCM increases. For instance, the highest volume fraction of bottom PCM is assumed in cases 3 and 6, and there is little improvement in energy output between these two cases. In case 5, each PCM occupies an equal fraction of the bed and this scenario capitalizes the most on the individual benefits of a low melting PCM with augmented latent heat and a high melting PCM. For this case, the latent heat of the bottom PCM is at a value that is large enough to extend the charging time to a point that complete melting of the top PCM can occur. Though cases 5 and 6 harness similar values of energy at the elevated exergy state for instance, the larger fraction of top PCM in case 5 additionally allows the HTF to discharge more energy at the melting temperature of the top PCM.

Table 17 provides the characteristics of the 2-PCM cascade system that incorporates a higher latent heat PCM at the top of the system. These systems experience an extended stage of HTF exiting at the top PCM melting temperature rather than at the high exergy state, as demonstrated in Figure 44. Case 9, which has the lowest fraction of top PCM, experiences the largest discharge time of all nine cases, thus releasing the highest amount of energy and exergy.

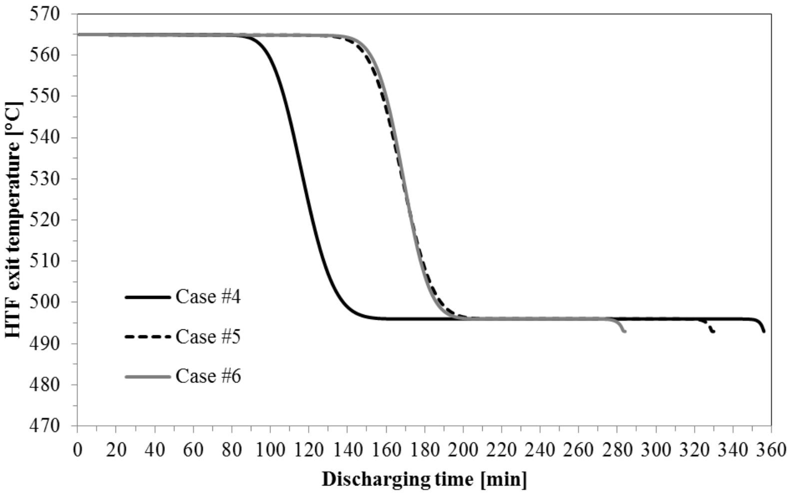

Figure 43. Temporal progression of the HTF exit temperature for cases 4 through 6 of the 2-PCM cascade.

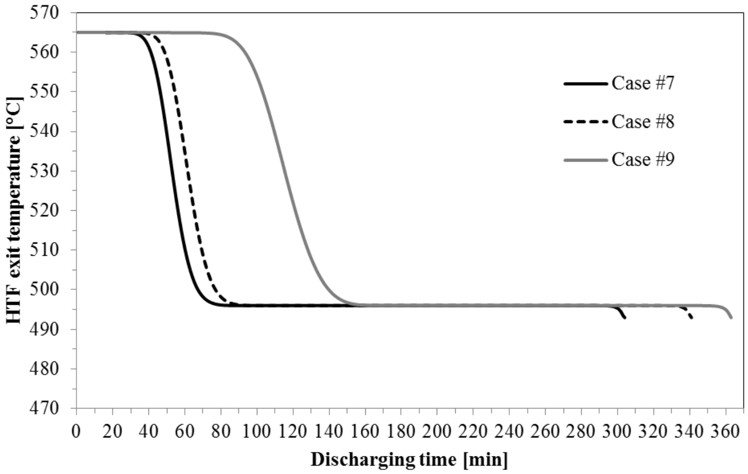

Figure 44. Temporal progression of the HTF exit temperature for cases 7 through 9 of the 2-PCM cascade.

The above assessment was used as a basis in understanding the effect of volume fraction and latent heat on the output of a 2-PCM cascade under the assigned parametric combination. A plant-level study that examines annual power production would provide a more quantitative guide on the benefits and drawbacks of various cascade design conditions. Each 2-PCM system showed an enhancement in energy and exergy output over the single-PCM systems, and all demonstrated overall exergy efficiencies of approximately 95% or higher. When the bottom PCM occupied a larger fraction of the bed than the top PCM, the system released more energy at the hot operating temperature. Increasing the latent heat of the bottom PCM improves this condition for the remaining cases in which the bottom PCM occupies a lower fraction. Increasing the latent heat of the top PCM compromises the high exergy release by lengthening HTF output at the melting temperature of the top PCM. Though all systems shared high performance in terms of second law efficiency and exhibited higher energy output than the single PCM cases, they expressed varying degrees in the quality of energy they can harness.

3.3.2.2 Three-PCM Cascaded System

As the number of PCMs in a cascaded system increases, the thermodynamic advantages are more pronounced [72, 75]. Thus a 3-PCM system should exhibit a greater second law efficiency than a 2-PCM system. The following parametric study evaluates the effect of latent heat on the performance and output of a 3-PCM cascade system. Each PCM occupies 1/3 of the bed and the phase change temperature decreases in value from the top to the bottom of the system. Similar to the 2-PCM parametric analysis, the systems adopt the same characteristics of the baseline LHS_{high} case, which were provided in Table 8. The first case assumes all 3 PCMs possess the same latent heat value. The next three cases, B – D, shift the high latent heat PCM from one cascade to the next, and the final three cases, E – G, apply the high latent heat PCM to two of the cascades in order to understand if there is any advantage in energy output. Table 18 provides the cases under evaluation. The melting points of the top and bottom PCM are equivalent to that of the 2-PCM parametric study ($T_{melt,top}$ = 495°C, $T_{melt,bottom}$ = 395°), and the middle PCM is assigned a normalized melt temperature of 0.50 ($T_{melt,middle}$ = 426.5°C).

Table 18. Assigned latent heat and phase change temperature for the cases assessed in the 3-PCM cascade system study.

Case #	*Top PCM* ($\theta_{melt} = 0.747$)	*Middle PCM* ($\theta_{melt} = 0.50$)	*Bottom PCM* ($\theta_{melt} = 0.386$)
A	InvSte = 0.64	InvSte = 0.64	InvSte = 0.64
B	InvSte = 0.64	InvSte = 0.64	**InvSte = 1.28**
C	InvSte = 0.64	**InvSte = 1.28**	InvSte = 0.64
D	**InvSte = 1.28**	InvSte = 0.64	InvSte = 0.64
E	InvSte = 0.64	**InvSte = 1.28**	**InvSte = 1.28**
F	**InvSte = 1.28**	InvSte = 0.64	**InvSte = 1.28**
G	**InvSte = 1.28**	**InvSte = 1.28**	InvSte = 0.64

Figure 45 provides the progression of the phase change front for the system in which all PCMs possess the same latent heat (case A). Figure 45(a), (c), and (e) illustrates the steady state charging process and Figure 45(b), (d), and (f) illustrates the steady state discharging process. The system charges in 352 minutes and can store 98.7% of its maximum potential storage capacity of 146.8 MWh. Discharging completes in 320 minutes, at which point the system recovers 166.88 MWh, resulting in a utilization ratio of 0.968 and overall exergetic efficiency of 96.4%. Figure 45 shows that at 120 minutes of charging, the top PCM is in the process of changing phase and by 240 minutes, the top PCM is completely molten. At this point, the sub-solidus front has exited the bed yet the bottom PCM remains below the charging threshold temperature, allowing the system to continue charging. The high capacity ratio of 98.7% is depicted in the final charging state, which shows that most of the bed reaches the hot inlet temperature. During the discharging process, the HTF exits the top of the bed at the high exergy state at 120 minutes. By 240 minutes, the HTF is exiting at the melting temperature of the top PCM and the pinch point zone of the middle PCM has shifted to the top cascade. By the final discharging time, most of the energy is depleted from the system. Due to the high degree of energy depletion at the end of the discharging process, the system immediately reaches steady state. This represents a nearly ideal scenario in which the system can store and recover a significant portion of the bed's potential storage capacity. Figure 46 provides the temporal variation of the outlet HTF temperature for the 3-PCM cascade of case A and the 2-PCM cascade of case 1, both having the same potential storage capacity. The figure illustrates the benefit of the 3-PCM cascade. The middle PCM serves as a buffer during the discharging process, allowing the system to extract more energy from the top PCM.

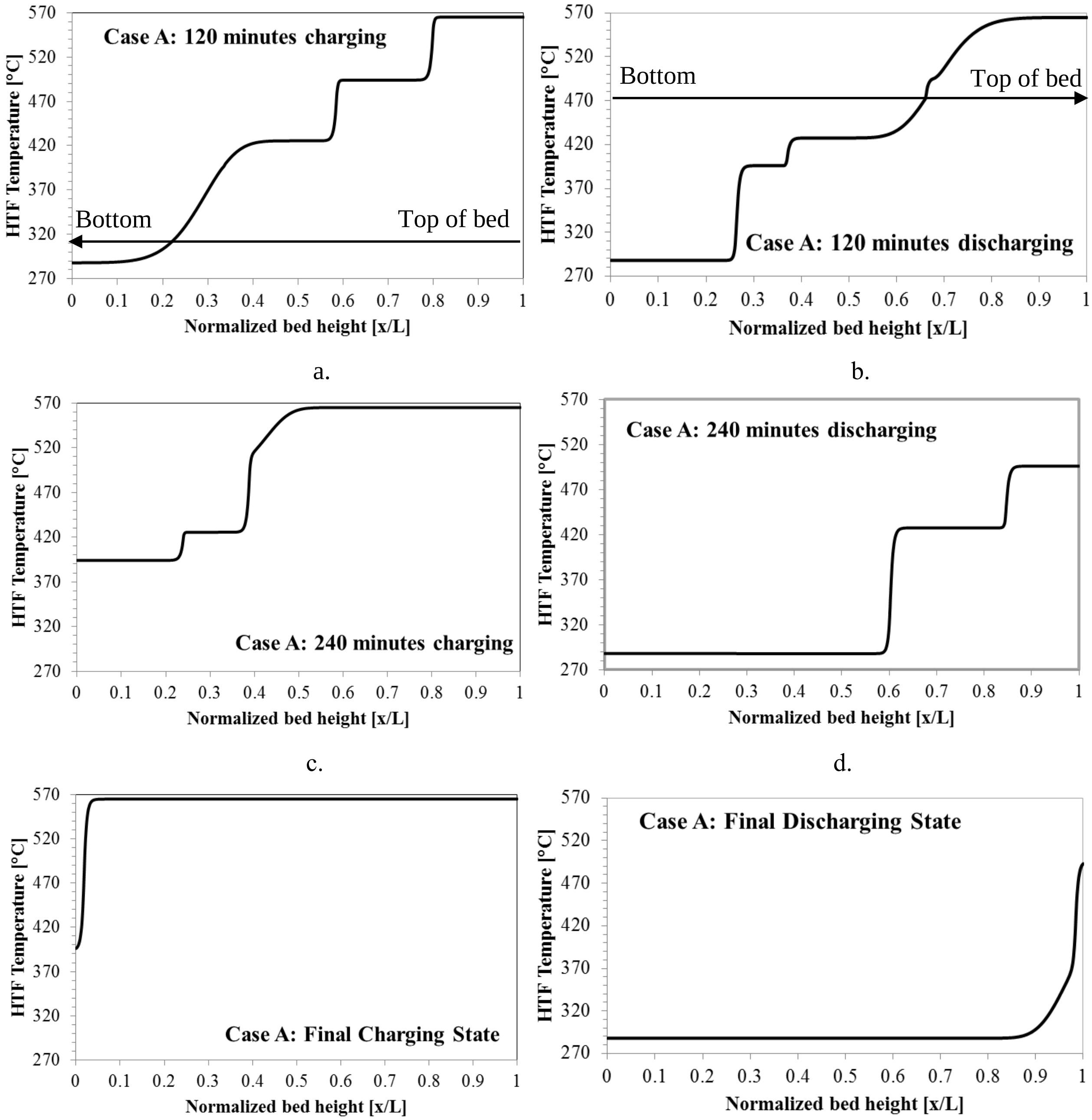

a.

b.

c.

d.

e.

f.

Figure 45. Steady state HTF axial temperature profile for a 3-PCM cascaded system. All PCMs have equivalent latent heat. 48(a), (c), and (d) provide the charging temperature profile of the HTF fluid at 120 minutes, 240 minutes, and the final state. 48(b), (d), and (f) illustrate the discharging HTF temperature profile for the same states. The arrows in (a) and (b) indicate the direction in which the phase change front moves.

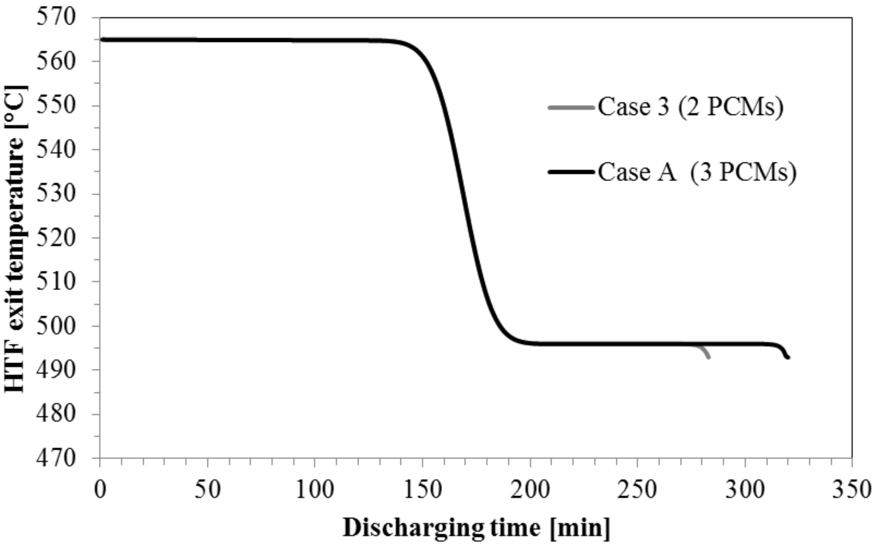

Figure 46. HTF exit temperature as a function of time for a 2-PCM and 3-PCM cascade of equivalent storage capacity.

Tables 19 and 20 provide the characteristics of the remaining 3-PCM cascade systems. Similar to the 2-PCM cascaded systems, the value of the latent heat has an impact on system output, which is a combined effect of the behavior during charging and discharing mode. Figure 47 provides the outlet HTF temperature profile over time for the cases in which the high latent heat was assigned to a single PCM. The outlet temperature profile of cases B and C are nearly identical and in both systems, the top PCM has a low latent heat value. Figure 48 provides the final charging and discharging state of cases B, C, and D. Cases B and C, which have the augmented latent heat in the bottom and middle PCM respectively, exhibit high capacity ratios, yet are not able to completely discharge all of the energy, as seen in the final discharging state figure. The case with the high latent heat in the top PCM, case D, does not completely reach the hot inlet temperature yet is able to recover the most energy of all three cases.

When the middle and bottom PCMs have the high latent heat value (case E), the system behaves in the same manner as the condition in which only the bottom PCM has a high latent heat (case B). The remaining two scenarios, wherein the middle PCM has the low latent heat (case F) and the bottom PCM has the low latent heat (case G), exhibit the greatest benefit over all other 3-PCM systems and the 2-PCM systems. They have a large potential storage capacity and demonstrate high capacity and utilization ratios, thus these last two cases deliver the largest quantity of energy and exergy. Figure 49 provides the temporal outlet HTF profile for cases E, F, and G.

Table 19. Steady state characteristics of each case assessed in the 3-PCM cascade wherein one of the three PCMs is assigned a high latent heat.

Case #	t_{Ch}/t_{Dch} (min)	$E_{Discharged}$ (MWh)	$Ex_{Discharged}$ (MWh)	Capacity Ratio	Utiliz. Ratio	$\eta_{ExOverall}$	Q_{bedMax} (MWh)	$t_{T\geq 99\%}$ (min)
B	394/326	169.57	95.41	0.985	0.895	0.947	168.7	152
C	391/325	168.96	95.06	0.987	0.889	0.951	168.7	151
D	382/364	178.98	99.99	0.947	0.931	0.957	168.7	105

Table 20. Steady state characteristics of each case assessed in the 3-PCM cascade wherein two of the three PCMs are assigned a high latent heat.

Case #	t_{Ch}/t_{Dch} (min)	$E_{Discharged}$ (MWh)	$Ex_{Discharged}$ (MWh)	Capacity Ratio	Utiliz. Ratio	$\eta_{ExOverall}$	Q_{bedMax} (MWh)	$t_{T\geq 99\%}$ (min)
E	404/326	169.57	95.41	0.986	0.803	0.949	190.7	152
F	462/412	207.73	116.44	0.985	0.971	0.953	190.7	151
G	462/415	208.80	117.01	0.987	0.972	0.958	190.7	150

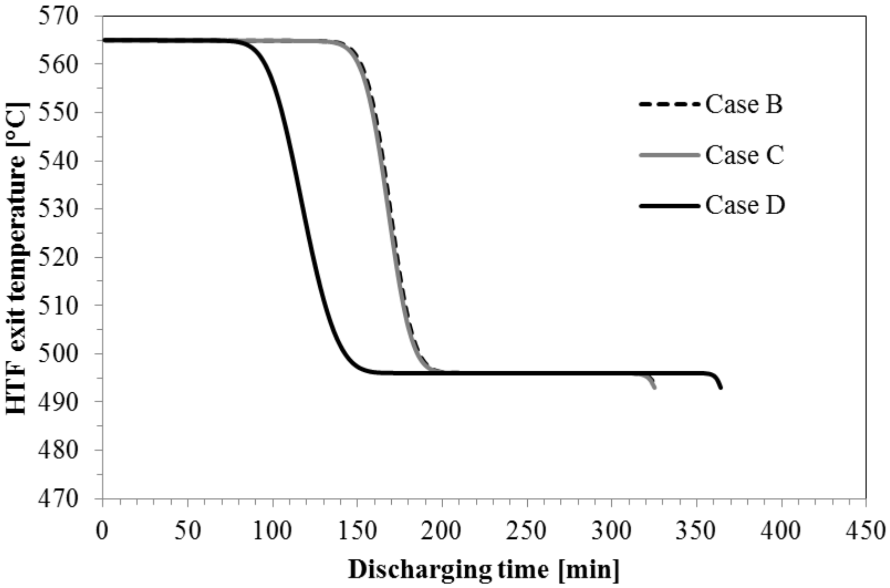

Figure 47. HTF exit temperature as a function of time for 3-PCM systems B – D.

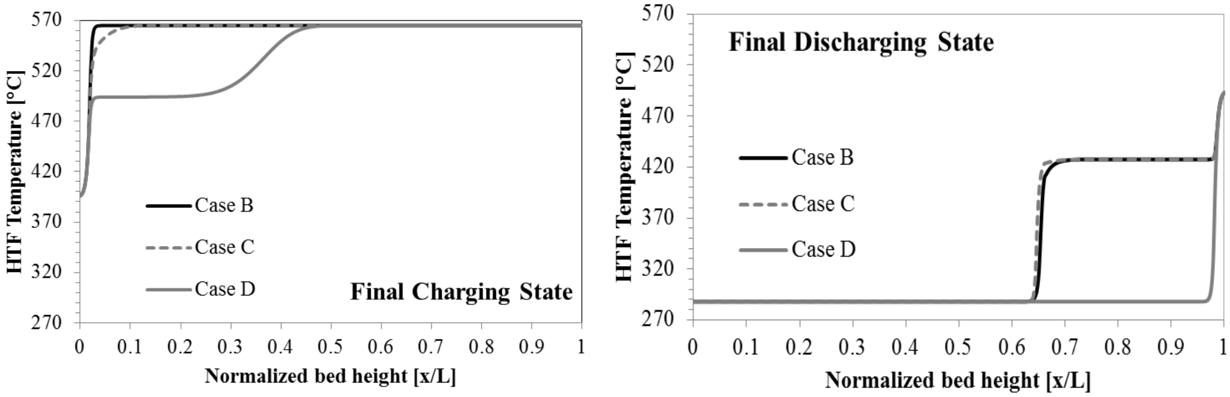

a. b.

Figure 48. The final steady state axial HTF profile of 3-PCM cases B-D. 48(a) provides the final charging state and (b) provides the final discharging state. These systems exhibit the augmented latent heat in one of the PCMs of the cascade.

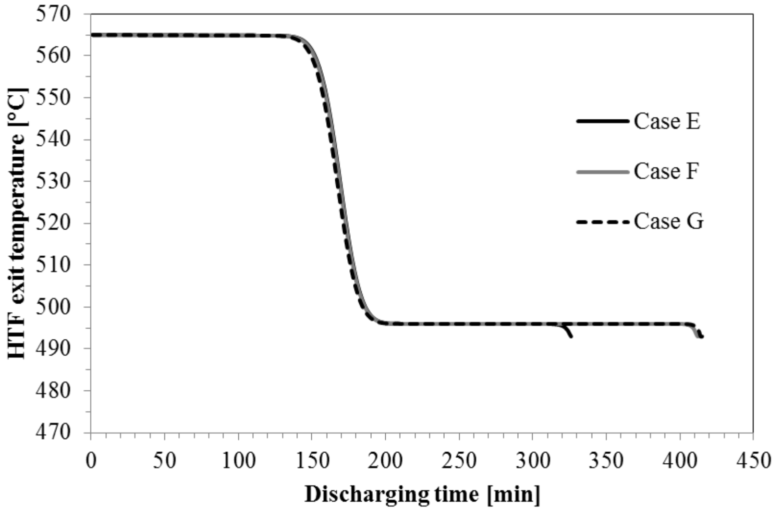

Figure 49. Outlet HTF temperature profile as a function of time for the 3-PCM cases E-F. Two PCMs in these systems exhibit the augmented latent heat value.

The above analysis is based on a specific parametric combination, as well as specific charging and discharging cut-off criteria. Under the assumed melting point combination, latent heat values, and PCM volume fraction, the advantages of a 3-PCM cascade surpassed that of the 2-PCM cascade when both held the same potential storage capacity. Nearly all 3-PCM systems could recover the maximum quantity of energy at the hot operating temperature, and benefited by extended release of energy at the melting temperature of the top PCM. The only exception was the case wherein the top PCM had the augmented latent heat (case D). This system released the HTF at the hot operating temperature for 105 minutes whereas the remaining cases did so in approximately 150 minutes.

The overall exergetic efficiency of the 3-PCM systems was not necessarily higher than the 2-PCM systems, and all cascaded systems demonstrated a decrease in exergy efficiency when compared to the SHS packed bed system and the single PCM cases. Though the second-law efficiency has previously been shown to improve with the increase in number of cascades, both charging and discharging cut-off conditions were not necessarily invoked. These threshold conditions determine and limit the quality of the flow stream as it exits the bed and affect the charging and discharging times, therefore they play a role in the amount of exergy that is stored, released, and lost.

This evaluation emphasizes the need to conduct carefully orchestrated studies on the design of packed bed LHS storage systems. The quantity and quality of useful energy that is recovered from a system are strongly influenced by the phase transition temperature, latent heat, and amount of PCM. These parameters should be judiciously chosen to maximize any gains that an be realized by employing a LHS packed bed system.

3.3.3 Analysis 3: LHS System Study with Realistic Parameters

The previous studies assumed a hypothetical PCM that adopted the same thermophysical properties as the SHS packed bed system. The current study compares the performance and tank requirements of the SHS packed bed system and a LHS system with a real salt PCM. The LHS system uses the NaCl/K_2SO_4 eutectic and its associated thermal properties. The PCM characteristics are provided in Table 21. The density and specific heat capacity of the solid and liquid phases were determined by a weighted summation of the properties of each individual component. Specific heat capacity values were obtained from the NIST WebBook [76] and density data were compiled from Janz [77]. Solid and liquid thermal conductivities could not be found in the literature, therefore a conservative value of 1 W/(m-K) was assumed and was based on the thermal conductivities of the NaCl and KCl in the solid phase.

Table 21. Thermal and physical properties of the LHS system evaluated in Analysis 3.

Parameter	***Value***
Porosity	0.35
$C_{p,PCM,solid}$	980 J/kg-K
$C_{p,PCM,liquid}$	1130 J/kg-K
$\rho,_{PCM}$	1690 kg/m3
$k,_{PCM}$	1.0 W/m-K
Latent heat	187000 J/kg
PCM shell thickness	0.00045 m
PCM shell thermal conductivity	13.94 W/m-K

Table 22 provides the parametric combination for both LHS and SHS systems of Analysis 3. In comparing the two systems, many differences become evident and these disparities may manifest in either an improvement or penalty in efficiency and system output. The LHS system employs a higher porosity, however this value is a more reasonable estimate for a randomly packed bed of spheres [78]. The low level achieved in the original SHS experiments by Pacheco et al. [36] was made possible by combining two types of particles that possessed different diameters. The thermal conductivity of the PCM is lower than the SHS case, yet this is closer to values that salts typically exhibit [79]. The particle diameter is larger in the LHS system and was chosen as a balance between ease in fabrication at a laboratory scale and maximizing heat transfer. This value can vary from system to system.

Table 22. Material properties implemented in Analysis 3.

Parameter	*SHS system*	*LHS system*
Porosity	0.22	0.35
Thermal conductivity	5 W/(m-K)	1 W/(m-K)
Inner particle diameter	19.05 mm	26.53 mm
Solid specific heat capacity	830 J/(kg-K)	980 J/(kg-K)
Liquid specific heat capacity	-	1130 J/(kg-K)
Solid density	2500 kg/m^3	2088 kg/m^3
Liquid density	-	1689 kg/m^3
Volumetric heat capacity	Solid: 2075 kJ/(m^3-K) -	Solid: 2046.24 kJ/(m^3-K) Liquid: 1908.57 kJ/(m^3-K)

Prior to evaluating the systems under their respective realistic conditions of Table 22, each parameter of the LHS system was varied one at a time while all other parameters were kept constant in order to isolate the respective parameter's effect on the output of the system. Porosity, density, heat capacity, thermal conductivity, and particle diameter were each varied from the value of the SHS system to the value of the LHS system of Table 22. The resulting performance metrics, energy output, and heat transfer characteristics of each run are provided in Table 23. The baseline case is the LHS system of Analysis 1, which had the same properties of the SHS but with the addition of latent heat. All properties were then combined and the SHS and LHS systems compared. The tank volume, height, and diameter of each run are respectively 650 m^3, 7.376 m, and 10.593 m, all corresponding to the baseline case.

Table 23. Steady state system characteristics for each case in the single parameter study.

Altered parameter	t_{Charge}/ $t_{Discharge}$ *(min)*	E_{out} *(MWh)*	*Mass PCM (kg)*	*Mass HTF (kg)*	h_p *(W/m^2K)*	k_{eff} *(W/mK)*	*Utilization Ratio*	*η Overall Exergy*
Baseline	181/205	104.68	1267500	260085	261.9	2.958	0.558	0.979
ρ_{PCM}	160/182	93.03	1058616	260085	261.9	2.958	0.522	0.982
k_{PCM}	178/201	102.62	1267200	260085	189.6	0.508	0.551	0.978
Porosity	189/213	109.61	1056250	413771	261.9	2.111	0.582	0.981
$C_{p,PCM}$	203/228	117.38	1267200	260085	261.9	2.958	0.582	0.980
D_i	179/202	103.06	1267500	260085	213.9	2.958	0.549	0.978
All parameters	181/200	103.80	882180	413771	148.6	0.507	0.534	0.979

As the thermal conductivity decreases from 5 W/(m-K) to 1 W/(m-K), the thermal energy output decreases by 2%. The reduced effective thermal conductivity and heat transfer coefficient result in a wider thermocline zone, which decreases the charging and discharging time since the threshold temperatures are reached more rapidly, resulting in a drop in useful energy output. The change in overall exergetic efficiency and utilization ratio are negligible at steady state.

Though the effect of thermal conductivity has been studied in sensible heat storage packed bed systems, there has not been a study of its effect on latent heat storage systems. Thus a quick discussion is included for the sake of completion. In Hanchen et al. [18], the thermal conductivity of a SHS packed bed system had a very minor influence on the charging, discharging, and overall efficiencies as well as the capacity factor. In Aly and El-Sharkawy [24], the thermal conductivity was varied across a wide range (0.5 W/m-K – 200 W/m-K) for the charging process in a SHS packed bed system. The authors demonstrated that effects were initially significant at high values of thermal conductivity, yet as the storage media quickly reached its storage capacity, the heat transfer rate diminished and after a certain point in time, the media with low thermal conductivity stored energy at a higher rate.

For the current simulation, the thermal conductivity can influence axial conduction through its role in thermal diffusivity, however it also appears in the effective heat transfer correlation through the Biot number. Therefore the thermal conductivity can influence convective heat transfer via thermal resistance within the PCM, unlike in the aforementioned sensible heat studies. To assess the degree of this effect, the thermal conductivity was varied between 0.5 W/(m-K) and 20 W/(m-K) while all other parameters remained at their nominal values. Figure 50 illustrates the variation in useful energy extracted from the system at steady state as well as the overall exergy efficiency. The figure demonstrates that the efficiency hovers near 98% for each case, and the energy output does grow with an increase in thermal conductivity, however it levels off at 5 W/(m-K) after which, the energy output varies to an almost negligible degree. Many salt PCMs possess low thermal conductivity (i.e. less than 5 W/(m-K)), therefore the high surface area of packed bed configurations serves as an enhancement mechanism for heat transfer. The significance of the slight gain in energy output may or may not warrant additional measures to enhance the PCM thermal conductivity and would depend upon the economic tradeoff between energy output and material/manufacturing costs of the enhancement technique.

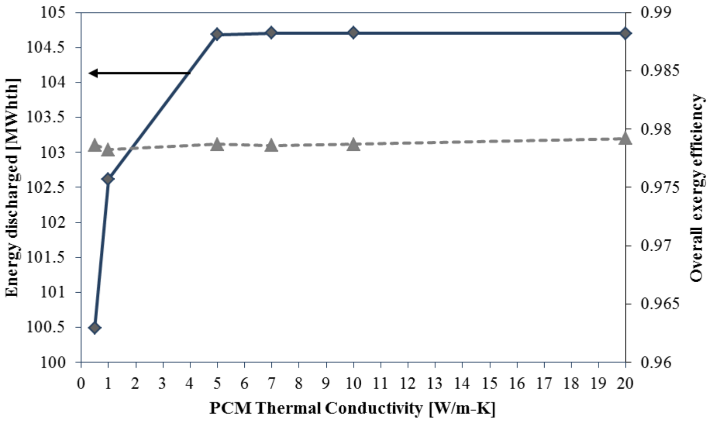

Figure 50. Effect of PCM thermal conductivity on recovered energy and overall exergy efficiency.

As expected, the increase in particle diameter reduces the energy discharged from the system due to the decrease in surface area per unit volume (i.e. a 28% reduction) and thus lower convective heat transfer rate and higher conductive resistance. The energy discharged from the system drops from 104.68 MWh to 103.06 MWh, a mere 1.6% reduction. The change in second law efficiency is also negligible.

For the same tank volume and porosity, the decrease in density of the PCM reduces its mass and maximum potential storage capacity by 16.5% while maintaining the same mass of HTF. With the same rate of energy entering the system, the low density case has less energy capacity per unit volume, therefore less energy is removed from the HTF and it reaches the charging threshold temperature in a shorter amount of time than the baseline case. This results in an 11.1% drop in useful energy extracted from the baseline case at steady state.

The increase in specific heat capacity augments the useful energy discharged from the system by 12.1% from the baseline case. This increase is a consequence of the enhanced thermal inertia caused by the larger storage capacity during the sensible heating phases, which delays the system from reaching the threshold charging and discharging temperatures. The sensible energy capacity increases from the nominal value of 416.9 kJ/kg to 465.9 kJ/kg, i.e. an 11.7% increase, over the operating temperature range of the system.

In maintaining a constant tank volume, augmenting the porosity from 0.22 to 0.35 reduces the mass of the PCM with a concomitant increase in mass of HTF. Similar to the effect of decreasing the PCM density, the lower PCM mass reduces the energy capacity per unit volume in the storage media. By increasing the porosity however, the additional mass of HTF supplements the stored energy in the system and this storage capacity is not inhibited by the phase change process, which tends to serve as a bottle neck in heat transfer as discussed in the previous sections. Figure 51 demonstrates that the potential storage capacity of the system decreases as the bed voidage increases. This is contrary to the way the system actually behaves at steady state. As the porosity increases, the total stored energy simultaneously grows, as illustrated in Figure 52. This contradiction between the hypothetical trend versus the simulated trend emphasizes the need to conduct detailed systems level studies. Though LHS systems seem thermodynamically favorable, they are plagued by limitations in the dynamics of heat transfer.

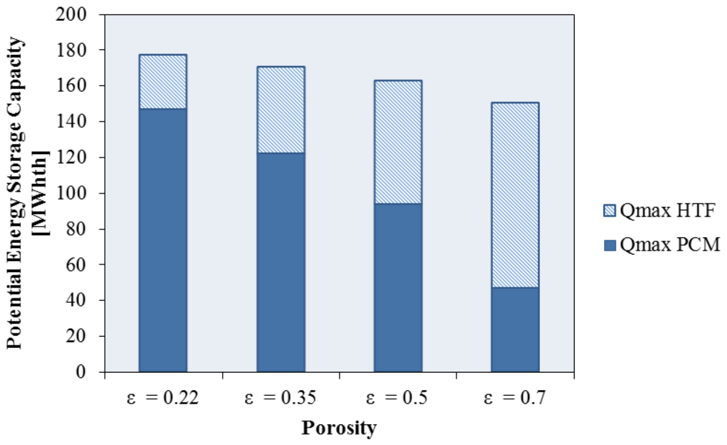

Figure 51. Effect of bed porosity on potential energy storage capacity. The figure includes the individual contribution of storage capacity due to the HTF and PCM.

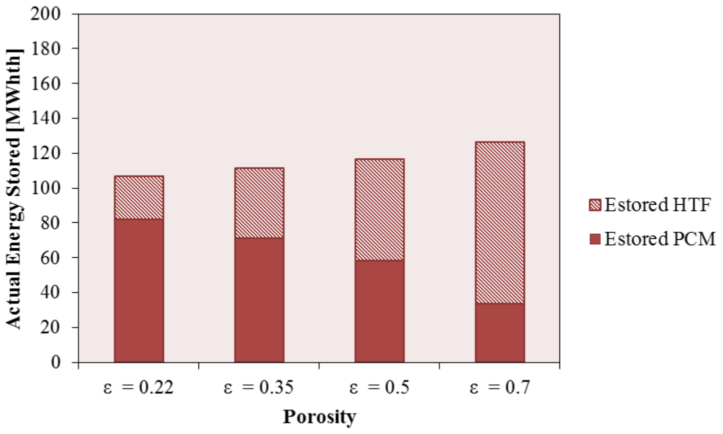

Figure 52. Effect of bed porosity on actual energy stored in the system at steady state. The figure includes the individual contribution of storage due to the HTF and PCM.

After combining all parameters such that the LHS system has the characteristics as defined in Table 22, the final useful energy discharged from the system is slightly less than the baseline case. The increase in porosity and specific heat capacity, which appreciably increased the energy output, were dwarfed by the adverse effects of reduced density, and reduced convective and conductive heat transfer due to the smaller particle diameter and lower thermal conductivity, respectively. Though not included in the table, the cumulative influence of density and specific heat capacity was investigated by merging the two as the volumetric heat capacity. This system produced 103.5 MWh at steady state, which is a 1.1% departure from the baseline case. Though the specific heat capacity had the strongest impact on increasing the output of the system, the low density suppressed this response.

In order to compare the SHS and LHS systems using realistic parameters, the SHS tank was sized such that it produced the equivalent useful energy discharged as the LHS system. The characteristics of each system are summarized in Table 24.

Table 24. LHS and SHS system performance indicators and sizing requirements for equivalent energy output at steady state.

	Bed Height (m)	*Bed Volume (m^3)*	*Mass PCM (kg)*	*Mass HTF (kg)*	*Util. Ratio*	$\eta_{ExOverall}$	Q_{bedMax} *(MWh)*	$Ex_{discharge}$ *(MWh)*	$E_{discharge}$ *(MWh)*
SHS system	8.193	722	1407900	288894	0.856	0.992	90	59.6	104.7
LHS system	7.427	654.5	888287	1864081	0.534	0.982	115	58.9	104.8

The LHS system increases slightly in volume from the hypothetical case to accommodate the parametric combination of the realistic case. The SHS packed bed system requires a larger volume and storage media mass to meet the discharged energy requirement. As shown in Figure 53, both systems complete the charging process in approximately the same amount of time, with the SHS system completing in 184 minutes and the LHS system in 183 minutes, therefore nearly the same amount of exergy enters the systems. Figure 54 provides the outlet HTF temperature of the LHS and SHS systems for the discharging process. The temporal variation in discharging outlet temperature of the LHS system shows a step response associated with the moving solidification front. The discharging process completes in 202 minutes. The SHS system maintains the outlet discharging temperature near $T_{HTF,h}$ for an extended period of time before declining as the thermocline zone exits from the top of the bed, at which point discharging terminates in 180 minutes. The extended period of high outlet temperature allows the system to provide the same quantity of energy, yet slightly higher quantity of exergy above the LHS case despite the fact that the discharging time is lower for the SHS system.

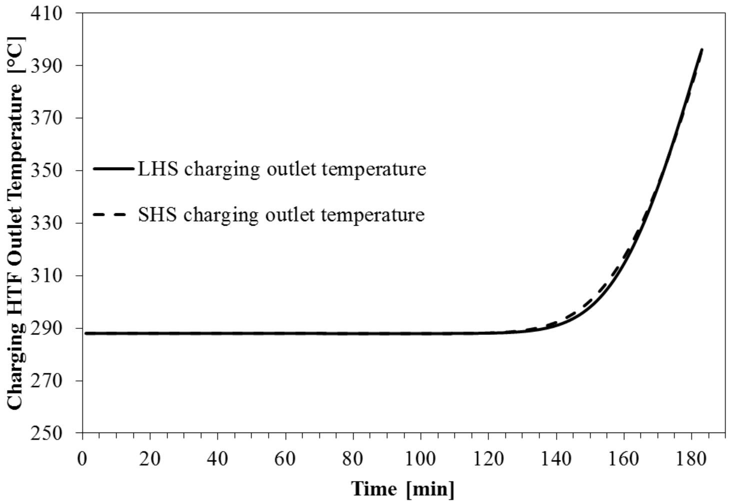

Figure 53. Outlet HTF temperature as a function of time for the LHS and SHS packed bed systems during the steady state charging process.

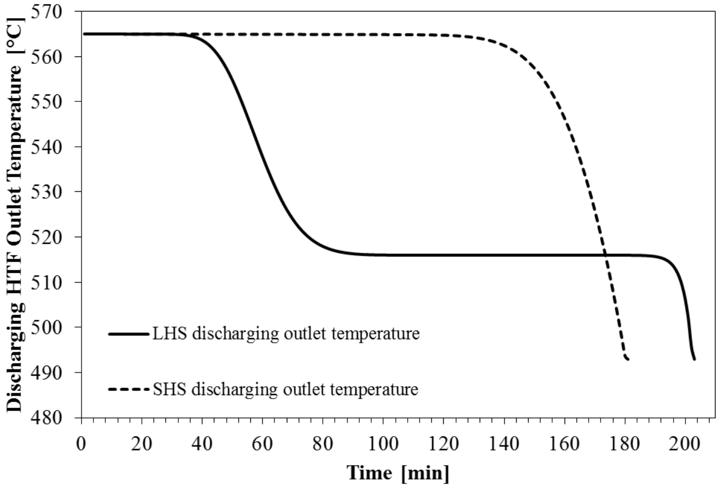

Figure 54. Outlet HTF temperature as a function of time for the LHS and SHS packed bed systems during the steady state discharging process.

In the LHS$_{high}$ system of Analysis 1, it was shown that the addition of latent heat increased the potential storage capacity of the system, yet a small fraction of this addition was exploited. Additionally, a higher fraction of the sensible heat capacity was utilized in the LHS system than in the SHS system due to the large degree of depletion during discharging. In the current scenario, the LHS system has a higher porosity, thus a large fraction of the energy extracted from the system is due to the storage capacity of the HTF. Of the 104.8 MWh extracted at steady state, 43.4 MWh (41.4% of the total) was due to the HTF, 49.1 MWh (46.9% of the total) was released as sensible heat, and 12.3 MWh (11.7% of the total) was released as latent heat. The degree of depletion is slightly lower and this is likely due to the thicker thermocline zone, which is a result of the larger particle diameter and lower thermal conductivity. Though lower than the baseline case of Analysis 1, the degree of discharge depletion is still greater than the SHS system, as illustrated in Figure 41, which provides the axial variation in HTF fluid temperature for consecutive charging and discharging states of the two systems.

All of the above cases exhibited high overall exergy efficiencies of approximately 98% or greater at steady state, therefore they performed well and demonstrated minimal exergetic losses over the course of a steady state cycle. This metric does not give an accurate assessment of the behavior or utilization of the system however. The LHS system required a smaller tank size, which would be a benefit in terms of cost, yet it is not able to tap into its full storage capacity, therefore the major benefit of reduced storage material cost is compromised. Thus the economic assessment is used to compare the cost benefit of the PCM system. Prior to doing so, a 3-PCM cascaded system study with salt PCMs ensues.

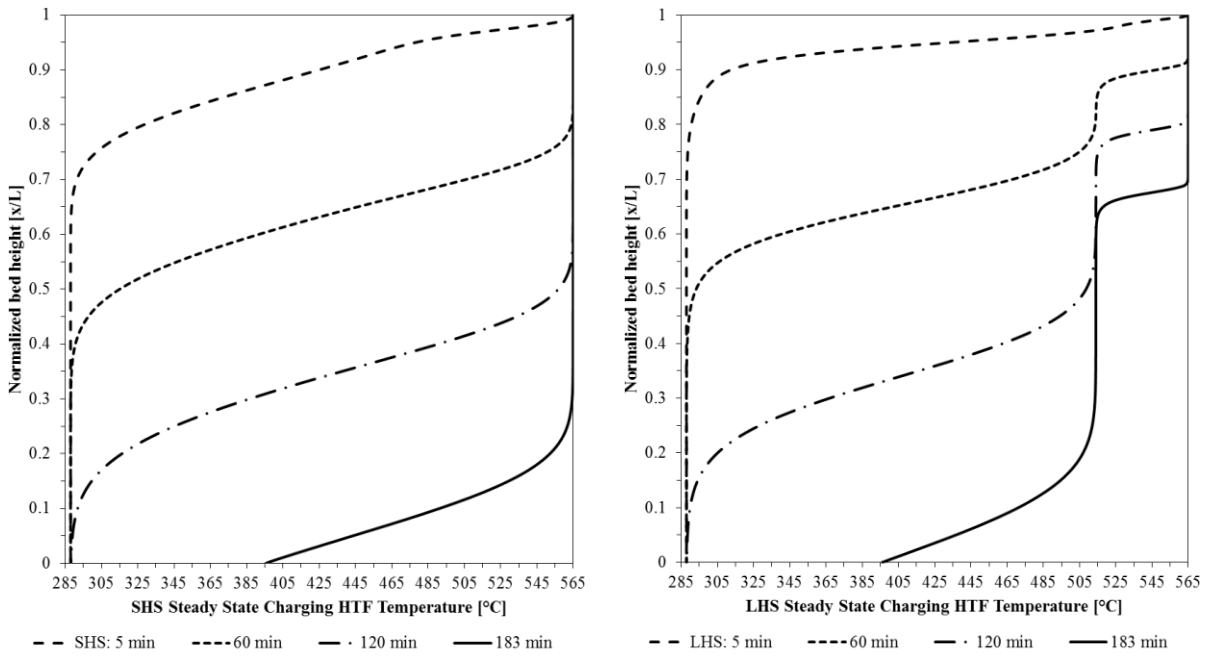

a.

b.

Figure 55. Steady state axial temperature profile at consecutive charging times for a) the SHS system, and b) the LHS system.

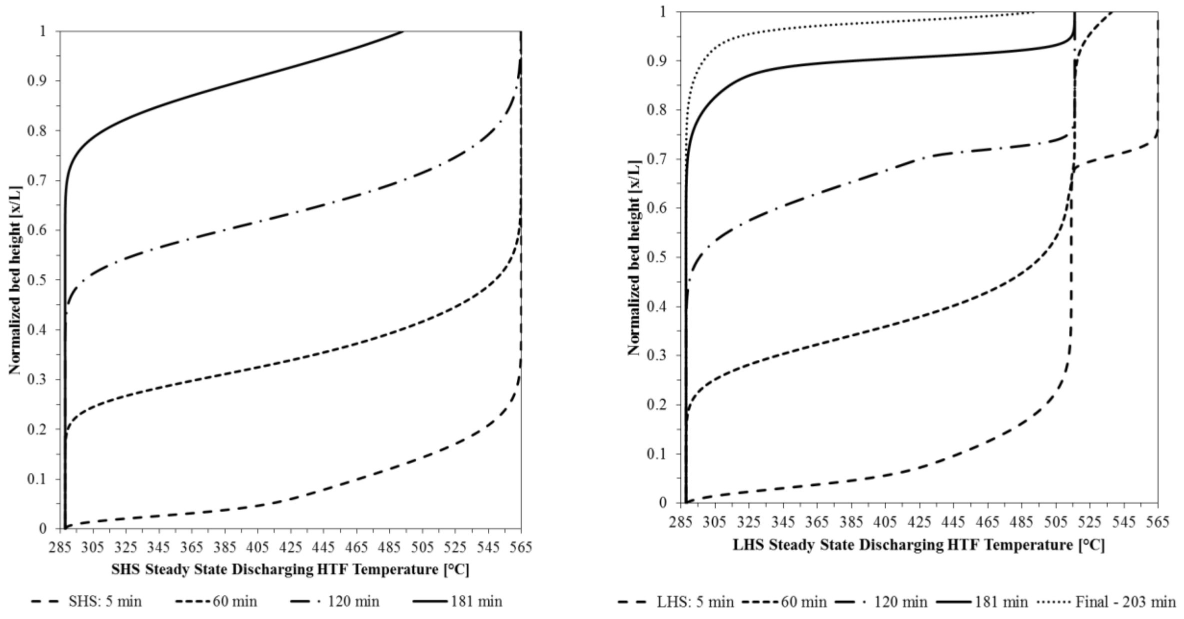

a.

b.

Figure 56. Steady state axial temperature profile at consecutive discharging times for a) the SHS system, and b) the LHS system.

3.3.3.1 Three-PCM Cascaded System with Salt PCMs

A cascaded system with three potential PCMs is analyzed using the porosity and particle diameter of the realistic LHS system scenario. Three salts were selected based on their phase change temperature and latent heat of fusion. The top PCM remained as the NaCl/K_2SO_4 eutectic, and Kenisarin's [79] extensive review of high temperature PCMs served as a guide in selecting the two remaining materials. Many PCMs were dismissed, including metals and lithium and fluoride salts due to their high cost. For instance, lithium carbonate has a relatively high thermal conductivity and specific heat capacity, and demonstrates greater thermal stability than some chlorides, yet the salt can exceed $4000/metric ton [80]. Potassium nitrate was excluded as a bottom PCM due to its low latent heat value. A $MgCl_2$/NaCl salt mixture was chosen as the middle PCM, primarily for its cost and availability of thermal properties. The latent heat of fusion/solidification as well as the melting/solidification temperatures were characterized in Trahan et al. [81]. For similar reasons, a KCl/$MgCl_2$/NaCl eutectic was chosen as the bottom PCM. The ternary eutectic was investigated by Gomez [82], who provided the melting/solidification temperatures and the latent heat values. The density and specific heat capacity of the middle and bottom PCM were estimated by a molar weighted average of the pure component properties, which were collected from the NIST Database [76, 77]. This method is found to be fairly accurate when compared to experimental measurements [83]. The individual solid thermal conductivities at elevated temperature were not available, therefore the same value of 1 W/m-K for the solid and liquid phases of the top PCM was assumed. This is close to the values that were defined for the binary eutectic in Kenisarin [79] and simplifies the analysis. It should be noted that magnesium chloride has handling and stability issues that are caused by its hygroscopic nature [81], however it was demonstrated in Zhao et al. [84] that it is suitable for use as a high temperature phase change material. For reference, Nemecek et al. [85] evaluates the ternary eutectic's use as a latent heat storage material and discusses its handling and drying procedure. Calcium chloride is also plagued by the same challenges. The final characteristics of the system are provided in Table 25.

Table 25. PCM properties and bed characteristics for the 3-PCM cascade system that employs real PCMs.

	Top PCM *32wt% NaCl- 68% K_2SO_4*	***Middle PCM*** *55 wt% $MgCl_2$ – 45% NaCl*	***Bottom PCM*** *59.98 wt% MgCl2 – 20.42% KCl – 19.6% NaCl*
Melting temperature [°C]	515	439.8*	382.1*
Solidification temperature [°C]	515	429.8*	390.9*
Latent heat of fusion [kJ/kg]	187	214.9*	197.6*
Latent heat of solidification [kJ/kg]	187	162.9*	183.7*
Solid density [kg/m^3]	2088	2109	2118
Liquid density [kg/m^3]	1130	1604	1607
Solid thermal conductivity [W/m-K]	1.0	1.0	1.0
Liquid thermal conductivity [W/m-K]	1.0	1.0	1.0
Solid specific heat capacity [J/kg-K]	980	1005	928
Liquid specific heat capacity [J/kg-K]	1130	1096	1035

* Values were obtained from the third heating/cooling cycle of the DSC/TGA measurements of the respective reference.

Table 26. Steady state characteristics of the 3-PCM cascade with salts. The first row provides the characteristics of a tank equal in size to the baseline single PCM case, and the second row is sized to provide the same energy output as the baseline case.

Tank size (m^3)	*t_{Ch}/t_{Dch} (min)*	*$E_{Discharged}$ (MWh)*	*Utiliz. Ratio*	*$\eta_{ExOverall}$*	*Q_{bedMax} (MWh)*
650	266/234	128.1	0.614	0.935	119.8
536.5	218/192	104.8	0.606	0.936	98.9

Table 27. LHS and SHS system performance indicators and sizing requirements for equivalent energy output at steady state of realistic storage systems. The PCM mass of the 3-PCM system is the total mass of all 3 PCMs combined. The top PCM mass required 242,713 kg, the middle PCM required 245,154 kg, and the bottom PCM required 246,200 kg. The Utilization ratio and QbedMax are based on the average heat capacity of the PCMs and the latent heat of melting.

	Bed Height (m)	*Bed Volume (m^3)*	*Mass PCM (kg)*	*Mass HTF (kg)*	*Utiliz. ratio*	*$\eta_{ExOverall}$*	*Q_{bedMax} (MWh)*	*$E_{stored\ in\ Solid}$ (MWh)*	*$E_{discharged}$ (MWh)*
SHS system	8.193	722	1407900	288894	0.856	0.992	90	77	104.7
1-PCM LHS	7.427	654.5	888287	416636	0.534	0.982	115	61	104.8
3-PCM LHS	6.088	536.5	734066	341520	0.606	0.936	98.1	60	104.8

Table 26 provides the characteristics of the 3-PCM cascade with salts for two different scenarios. The utilization ratio and maximum potential storage capacity of the bed are based on the latent heat of fusion and average specific heat capacities of the salts. The first row demonstrates the energy output if the system has the same tank size as the baseline case and all of the cascaded systems that were studied, i.e. a size of 650 m^3. The system provides 128.1 MWh and is able to utilize 67.2% of the potential storage capacity. The same size tank filled with capsules of the NaCl/K_2SO_4 eutectic only, produced 103.8 MWh and had a utilization ratio of 53.4%. Thus the 3-PCM cascade increased the potential energy output by 23.4%. The exergy efficiency decreased however. Table 27 presents the final tank dimensions, mass requirements, and performance indicators for the three realistic systems that are going to be evaluated in the economic analysis of the following chapter.

CHAPTER 4: ECONOMIC ANALYSIS

4.1 Introduction

The goal of the previous chapter was to compare the performance and system output of SHS and LHS packed bed systems using conditions that may be realistically encountered. Though the phase change process augments the potential storage capacity of LHS systems, the pinch point phenomenon hinders the system’s ability to capitalize on this capacity. Despite this shortcoming, the LHS system required a smaller tank size than the SHS system to discharge the same quantity of energy. The current chapter evaluates the cost of a single-PCM LHS system, 3-PCM LHS system, and the SHS system to understand the economic gain that one may have over the other. It is only a preliminary estimate used to compare the material costs of the different systems and does not include the balance of system costs that would represent a more accurate assessment. The economic assessment is also based on the metric of energy output, which does not directly correspond to electricity production due to the variation in the quality of energy recovered from the storage systems.

Studies that have compared system costs have primarily focused on comparisons between LHS packed bed systems or SHS packed bed systems with the conventional molten salt 2-tank design. Mathur et al. [86] compared the cost of a 2-tank system and a cascaded PCM system with equivalent thermal energy storage capacity. Balance of system costs were included, however the study did not account for the HTF that fills the pore space of the packed bed system. The study demonstrated that the LHS system costs are 40% lower per kWh_{th} than the conventional 2-tank design. Nandi et al. [87] compared the system cost and Levelized Electricity Cost (LEC) of a 2-tank system, and SHS thermocline, each providing 6 hours of storage for a 50 MW parabolic trough CSP plant. The 2-tank system capital storage cost was 78% higher and the LEC cost was 59% higher than the SHS packed bed system. Nithyanandam and Pitchumani [68] conducted a plant-level study for a Rankine cycle and Supercritical s-CO_2 cycle and evaluated the LEC when a 2-tank system and LHS packed bed system was integrated. Various design conditions were investigated and the study compared the costs of the LHS systems with lowest LEC. For the 200 MW Rankine cycle plant, the storage capital cost of the 2-tank system was $204.6 US Million and the lowest capital storage cost of the PCM packed bed storage was $74.6 US Million, a 63.5% decrease in capital cost. In Pacheco et al. [36], the costs of a 688 MWh two-tank and SHS packed bed storage system were compared. The study found that the packed bed system was approximately 66% of the cost of the 2-tank molten salt system. These previous studies illustrate that packed bed systems do cost less than the conventional 2-tank design. The current study investigates the relative storage system cost for each of the SHS, LHS, and cascaded LHS packed bed systems using recent pricing and compares this to the 2-tank design.

4.2 Pricing Method

A cost estimate of each system was calculated by adopting historical cost data and applying the Chemical Engineering Plant Cost Index (CEPCI) [88] to account for inflation [52]. The tanks are constructed of stainless steel 347 due to the system's high operating temperature [32]. Estimates for installed costs of field erected vertical storage tanks can be calculated with the following correlation that is valid for 21,000 < V_{tank} < 11,000,000 gallons and accounts for economies of scale [89]

$$C = 1.218F_M \exp[11.662 - 0.6104(lnV_t) + 0.04536(lnV_t)^2] \tag{68}$$

The correlation is defined for carbon steel, therefore the material cost factor, F_M, for the price of stainless steel 347 relative to carbon steel is applied. F_M is equal to 3.0. The installed price is then calculated by multiplying the purchase price of Equation 68 by the installed cost multiplier for field erected stainless steel storage tanks, which is equal to 1.2 [89].

$$Installed\ Cost = (purchase\ price)(multiplier) \tag{69}$$

Equation 68 is based on cost data from 2002. For an updated cost estimate, the annual 2013 CEPCI is applied:

$$C_{2013} = C_{2002}\frac{CEPCI_{2013}}{CEPCI_{2002}} \tag{70}$$

where the annual average CEPCI for 2002 is 395.6 and for 2013 is 567.3 [88].

Calcium silicate block insulation prices were derived from [90]. The insulation unit cost was taken as a constant value of $235/m^2 for a thickness of 500 mm. The study in [90] did not specify the year in which these prices were derived, therefore compensation for inflation is neglected.

The tank foundation was similarly priced from data in [90]. The foundation diameter was assumed equivalent to the tank diameter. Three foundation layers were implemented. The bottom most layer is a 610 mm thick concrete slab in which 73 kg of steel reinforcement per cubic meter of slab is used. The concrete slab is $85/m^3 and the steel reinforcement is $0.80/kg. The second layer is a 230 mm thick insulating concrete slab that is estimated as $100/m^3. The top-most layer is then a 300 mm thick foam glass insulation that costs $356/m^3.

Sodium chloride bulk prices were acquired from the 2014 USGS mineral commodity summary [91]. The 2013 price for vacuum and open pan salt is $175/metric ton, which was the highest purity grade salt that was provided in the summary. The nitrate eutectic that served as the HTF was priced as $1.25/kg [86]. The price of potassium sulfate was provided through personal communication from Great Salt Lake Mines, a U.S. company that mines and distributes sulfate of potash, which is a form of the salt used in the fertilizer industry. The value used in the analysis is $940/metric ton. The price of 98% purity magnesium chloride was based on a quote from a company specializing in the sale of inorganic chemicals. It is typically sold in aqueous form due to its hygroscopic nature, therefore the price in anhydrous form of $1300/ton is relatively high compared to its hydrated counterpart. The price of potassium chloride was based on an internet survey of commodity prices for the salt. The assumed value is $500/metric ton. Encapsulation cost was taken as $0.25/kg, which is an estimate provided in [86]. This value is only used as a starting point for the analysis. The price of 8x12 silica sand was provided by Premier Silica as $195/short ton and the price of 3/8” quartzite was provided by Ulm Quartzite Quarry as $17.50/short ton. Using the mass fraction of 30% silica sand and 70% quartzite, the total price for the SHS filler material is

$78/metric ton. After conducting a survey of prices found in the literature and previously requested quotes from salt distributors, the prices of sodium chloride, potassium sulfate, magnesium chloride, and the nitrate eutectic were chosen due to the fact that they were at the high range of the price spectrum. These values are only for a preliminary cost assessment and can change significantly based on location of the CSP facility, annual market fluctuations, and purity of the material. Freight charges are neglected in the analysis since they are unknown, and salt melting costs for both the HTF and PCM are not estimated, however they would increase system costs to differing degrees for each system. Table 28 summarizes the cost of the storage media. Since the prices can vary significantly between distributors and location, the relative storage system costs are provided as a range of values. For example, several references cite different values for the cost of the eutectic nitrate solar salt used as the HTF. The capital cost estimate in Kelly [32] cites the price of the solar salt, including handling, as $1.10/kg, whereas Mathur et al. [86] provides a cost of $1.25/kg, and Kenisarin [79] identifies the price as $0.50/kg. Therefore a low, middle, and high estimate in capital storage cost is included, and the range is based on a 20% increase and decrease in the quoted prices of the HTF and filler materials provided in Table 28. Tank costs are not varied. The head space in each tank that may be needed to accommodate storage material/HTF expansion was ignored, therefore the tanks were solely sized according the packed bed volume requirement. Balance of system costs, such as manifold piping, heat tracing elements, and pumps, were additionally neglected.

Table 28. Storage material and HTF cost

Storage Media	*Specific cost ($/kg)*	*High estimate ($/kg)*	*Low estimate ($/kg)*
Quartzite/8x12 silica sand mixture	$0.078/kg	$0.094/kg	$0.062/kg
NaCl - K_2SO_4 eutectic	$0.695/kg	$0.834/kg	$0.556/kg
$MgCl_2$ – NaCl eutectic	$0.794/kg	$0.953/kg	$0.635/kg
KCl – $MgCl_2$ – NaCl eutectic	$0.916/kg	$1.10/kg	$0.733/kg
solar salt HTF	$1.25/kg	$1.50/kg	$1.00/kg
Encapsulation	$0.25/kg	$0.30/kg	$0.20/kg

4.3 Cost Comparison of SHS vs. LHS Packed Bed Thermocline Systems

Table 29 itemizes the cost of each system, the sizes of which are based on the requirements needed to establish the same energy output, and Figure 58 plots each system's cost breakdown using the middle filler and HTF price estimate. The low and high total estimates are also provided in Figure 58 as error bars. As is illustrated, both LHS systems exceed the cost of the SHS system, which is largely due to the cost of the phase change material and encapsulation. The SHS system benefits from not requiring encapsulation, from having a low porosity which reduces the HTF cost, and from the very low storage material cost. If encapsulation was disregarded, the LHS systems would continue to remain above the SHS cost. Even with the high cost of the middle and bottom PCM, the cascaded system does benefit from lower material requirements when compared to the single PCM system.

Table 29. Itemized cost of each packed bed system.

Item	*SHS system*	*1-PCM LHS system*	*3-PCM LHS system*
Tank volume, m^3	722	654.5	536.5
Tank cost, $k	$356.71	$340.02	$309.40
Insulation cost, $k	$84.78	$78.79	$68.32
Foundation cost, $k	$19.15	$19.15	$19.15
Total cost (Low estimate), $k	$909.61	$1526.14	$1356.26
Total cost (Mid estimate), $k	$931.57	$1798.18	$1596.11
Total cost (High estimate), $k	$953.53	$2070.23	$1799.25

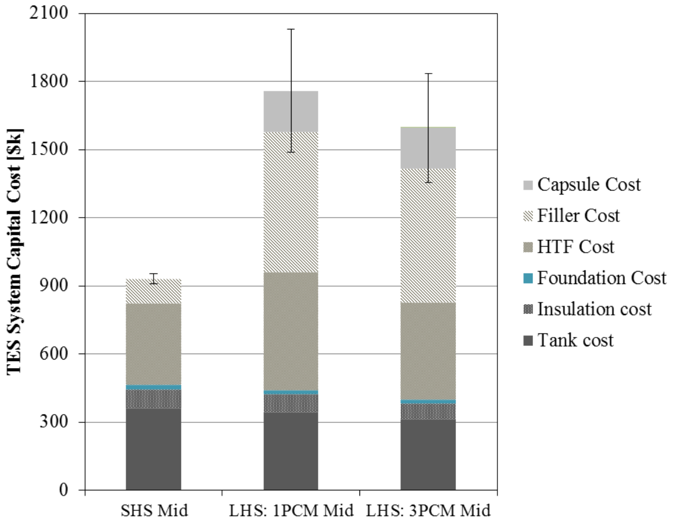

Figure 57. Capital cost breakdown of the SHS, 1-PCM, and 3-PCM LHS packed bed systems. The cost of each item is provided for the middle filler and HTF estimate. The high and low total cost are provided.

To determine if the cost of the LHS systems would benefit in lower porosity and particle diameter, two additional scenarios were analyzed. These include:

1.) The same porosity and particle diameter of the SHS system of Pacheco et al. [36] was employed. The tank size was 528 m^3 when a porosity of 0.22 and particle diameter of 19.05 mm was employed.

2.) A significantly smaller particle diameter of 10 mm and a porosity of 30% was employed for the 3-PCM cascaded system. The second scenario was demonstrated in [86] to produce a high utilization ratio for a 3-PCM cascade. The resulting tank volume is 515 m^3. This produced a slightly higher output of 105.1 MWh.

The resulting costs using the middle storage media price estimates are provided in Table 30. The total cost of this system is slightly less than the 3-PCM cascade with higher porosity and particle diameter due to the large reduction in HTF cost, however the PCM and encapsulation costs keep the price largely elevated above the SHS system.

Table 30. Total cost of the 3-PCM cascaded system with low particle diameter and porosity.

Item	*3-PCM LHS system with low D_p and ε*	
Particle diameter, mm	19.05	10.0
Porosity	0.22	0.30
Tank volume, m^3	528	515
Tank cost, $k	$307.11	$303.6
Insulation cost, $k	$67.56	$66.41
Foundation cost, $k	$19.15	$19.15
HTF cost, $k	$264.09	$351.25
Storage media cost, $k	$695.40	$608.71
Encapsulation cost, $k	$216.73	$189.71
Total cost (mid estimate), $k	$1570.04	$1538.82

4.4 Cost Comparison of Packed Bed Thermocline Systems with the 2-Tank Design

The state-of-the-art system requires two tanks and only utilizes the HTF to store energy. Heat exchangers may also be required if the HTF differs from the molten salt storage media. With the high cost of the HTF and two tank requirement, it is expected that the cost of this design would exceed that of the single tank systems. To test this hypothesis, a 2-tank system was sized for the same energy requirement of 104.8 MWh based on a temperature differential of 277°C (565°C - 288°C) and same average HTF density and specific heat capacity that was employed in the packed bed studies. To simplify the analysis, any inactive volume needed for HTF expansion or vapor pressure head was neglected. The same tank diameter of 10.593 m, which was used in all other analyses, was adopted. Based on these assumptions, each tank would require a volume of 493.9 m^3. This is very similar to the size of the Solar Two storage tanks, which had a volume of 544.73 m^3 for an energy output of 110 MWh for the same temperature range [92], though sizing the system with the above assumptions deflates the volume requirement. Table 31 adds the the 2-tank cost to Table 29 so the values may be compared. The tank, insulation, and foundation costs provided in the table are for a single tank and the total cost doubles these values. The HTF cost is based on the volume needed for one tank. The values demonstrate that the elevated costs of the LHS systems are still lower than the 2-tank design, however there is significantly greater cost advantage with the SHS packed bed system. The exergy recovered from the systems varies, therefore the specific price ($/kWhth) was not included as this would be a misleading cost metric [68].

Table 31. Cost comparison for all systems. The costs of the foundation, tank, and insulation for the 2-tank system are for a single tank only. The total cost includes the both tanks and the HTF.

Item	*SHS system*	*1-PCM LHS system*	*3-PCM LHS system*	*2-Tank system*
Tank volume, m^3	722	654.5	536.5	494 (single tank)
Tank cost, $k	$356.71	$340.02	$309.40	$297.78
Insulation cost, $k	$84.78	$78.79	$68.32	$64.54
Foundation cost, $k	$19.15	$19.15	$19.15	$19.15
Total cost (low estimate), $k	$909.61	$1526.14	$1356.26	$1661.15
Total cost (mid estimate), $k	$931.57	$1798.18	$1596.11	$1885.71
Total cost (high estimate), $k	$953.53	$2070.23	$1799.25	$2110.26

CHAPTER 5: DISCUSSION, CONCLUSIONS, AND RECOMMENDATIONS

Numerous research efforts are currently dedicated to developing low cost utility-scale CSP thermal energy storage systems that employ the single tank packed bed concept. The motivation for this work was to conclude if these systems are indeed economically favorable and show promise for future endeavors. Historical studies in phase change storage have evaluated these systems under simplified conditions. With advancements in CSP technology and a transition to high temperature systems, newer TES studies must adopt conditions that are more likely to be encountered. Cycling a system to steady state, and employing charging and discharging cut-off temperatures invokes results that may differ from the simplified assumptions previously adopted. For instance, Adebiyi et al. [70] showed that the latent heat must be highest at the bottom of a 3-PCM cascade for optimal second-law efficiency. The current study demonstrates however, that the charging and discharging threshold temperatures strongly affect the optimal configuration for enhanced system output, and rather than a thermodynamic gain in efficiency, there is a penalty when multiple PCMs are used. Many investigations also evaluate LHS packed bed systems with a hypothetical PCM in order to parametrically study the factors that influence performance. This study expands the scope of performance studies by comparing a hypothetical case to a realistic system in order to understand the differences and drawbacks that may be encountered.

The performance study examines the heat transfer mechanisms that prevent full utilization of the storage capacity of LHS systems, and discusses problems and tradeoffs that are faced in PCM selection. For single-PCM systems, the following conclusions were made:

1.) The charging process benefits from the use of a PCM that melts below the charging threshold value. The large temperature difference between the melting point and inlet HTF temperature induces a high rate of heat transfer that facilitates a faster travel rate of the pinch point interface. Thus a large fraction of the bed reaches the hot operating temperature, and the system can discharge HTF at the high exergy state for an extended period of time before the thermocline exits the bed. However, since the melting point falls below the discharging cut-off temperature, they cannot recover all of the latent heat.

2.) The discharging process benefits from a PCM with high melting temperature that lies above the discharging threshold temperature. Since the systems discharge HTF above the threshold value, they are able to extract a large fraction of the latent heat. The drawback is the reduced quality of energy released from the system since they do not store much energy at the hot operating temperature.

Cascaded systems take advantage of the benefits provided by employing a low and a high melting PCM. The low melting PCM serves as a buffer, extending the charging time such that the system can store and recover energy at the high exergy state. The high melting PCM auments the amount of energy that is released from the system. This added energy is liberated at the melting temperature of the top PCM, which is lower in exergy yet still functional in producing electricity. The degree to which cascaded systems benefit from multiple PCMs is highly dependent on the volume fraction of each PCM and the distribution of latent heat. Phase change temperature also affects useful energy output, however this effect was not studied for cascaded systems. The conclusions place emphasis on the need to evaluate the quality of energy rather than quantity of energy that is discharged from packed bed systems. The 2-PCM and 3-PCM systems consistently produced more energy than the single-PCM systems, however some cascaded structures discharged HTF at the high exergy state for less time. A plant level study is needed to understand how the distribution of energy that is discharged from the cascade systems affects annual electricity production.

The economic study demonstrates that there are advantages in single tank packed bed systems over the conventional 2-tank systems. There are further studies that must be pursued to firmly establish the economic benefit. These include:

1.) The preliminary economic assessment neglected heat exchanger, piping, pump, O&M, and salt melting costs, as well as balance of system costs that are inherently necessary for a true capital cost study. These should be included in future investigations.

2.) A plant level study that compares the electrical output and levelized cost of energy from each of the systems should be conducted.

3.) An exploratory cost study on potential sensible heat and phase change materials would be beneficial. This should include recycled materials such as that found in Py et al. [93] which presents a very low cost material that can be used for high temperature applications.

4.) Encapsulation methods and costs for high temperature packed bed LHS systems are still needed. There are many technical hurdles in developing encapsulation techniques that are robust enough to withstand thousands of thermal cycles. Until this has been established, SHS packed bed systems are likely to be technically and economically superior in the near future.

REFERENCES

[1] Kolb, G. J., Ho, C. K., Mancini, T. R. and Gary, J. A., 2011, "Power Tower Technology Roadmap and Cost Reduction Plan," Albuquerque, NM, Sandia National Laboratories, SAND2011-2419, p. 38.

[2] Kuravi, S., Trahan, J., Goswami, D. Y., Rahman, M. M. and Stefanakos, E. K., 2013, "Thermal Energy Storage Technologies and Systems for Concentrating Solar Power Plants," Progress in Energy and Combustion Science, 39 (4), p. 285-319.

[3] EPRI, 2010, "Solar Thermocline Storage Systems: Preliminary Design Study," Palo Alto, CA, Electric Power Research Institute, 1019581, June 2010.

[4] Bindra, H., Bueno, P., Morris, J. F. and Shinnar, R., 2013, "Thermal Analysis and Exergy Evaluation of Packed Bed Thermal Storage Systems," Applied Thermal Engineering, 52 (2), p. 255-263.

[5] Flueckiger, S. M. and Garimella, S. V., 2014, "Latent Heat Augmentation of Thermocline Energy Storage for Concentrating Solar Power – a System-Level Assessment," Applied Energy, 116, p. 278-287.

[6] Brosseau, D., Kelton, J. W., Ray, D., Edgar, M., Chisman, K. and Emms, B., 2005, "Testing of Thermocline Filler Materials and Molten-Salt Heat Transfer Fluids for Thermal Energy Storage Systems in Parabolic Trough Power Plants," Transactions of the ASME Journal of Solar Energy Engineering, 127, p. 109-116.

[7] Achenbach, E., 1995, "Heat and Flow Characteristics of Packed Beds," Experimental Thermal and Fluid Science, 10, p. 17-27.

[8] Atmakidis, T. and Kenig, E. Y., 2009, "CFD-Based Analysis of the Wall Effect on the Pressure Drop in Packed Beds with Moderate Tube/Particle Diameter Ratios in the Laminar Flow Regime," Chemical Engineering Journal, 155 (1–2), p. 404-410.

[9] Cheng, N.-S., 2011, "Wall Effect on Pressure Drop in Packed Beds," Powder Technology, 210 (3), p. 261-266.

[10] Choi, Y., Kim, S. and Kim, D., 2008, "A Semi-Empirical Correlation for Pressure Drop in Packed Beds of Spherical Particles," Transport in Porous Media, 75 (2), p. 133-149.

[11] Chu, C. F. and Ng, K. M., 1989, "Flow in Packed Tubes with a Small Tube to Particle Diameter Ratio," AIChE Journal, 35 (1), p. 148-158.

[12] Cohen, Y. and Metzner, A. B., 1981, "Wall Effects in Laminar Flow of Fluids through Packed Beds," AIChE Journal, 27 (5), p. 705-715.

[13] de Klerk, A., 2003, "Voidage Variation in Packed Beds at Small Column to Particle Diameter Ratio," AIChE Journal, 49 (8), p. 2022-2029.

[14] Di Felice, R. and Gibilaro, L. G., 2004, "Wall Effects for the Pressure Drop in Fixed Beds," Chemical Engineering Science, 59 (14), p. 3037-3040.

[15] Eisfeld, B. and Schnitzlein, K., 2001, "The Influence of Confining Walls on the Pressure Drop in Packed Beds," Chemical Engineering Science, 56 (14), p. 4321-4329.

[16] Winterberg, M. and Tsotsas, E., 2000, "Impact of Tube-to-Particle-Diameter Ratio on Pressure Drop in Packed Beds," AIChE Journal, 46 (5), p. 1084-1088.

[17] Benyahia, F. and O'Neill, K. E., 2005, "Enhanced Voidage Correlations for Packed Beds of Various Particle Shapes and Sizes," Particulate Science and Technology, 23, p. 169-177.

[18] Hanchen, M., Bruckner, S. and Steinfeld, A., 2011, "High-Temperature Thermal Storage Using a Packed Bed of Rocks - Heat Transfer Analysis and Experimental Validation," Applied Thermal Engineering, 31, p. 1798-1806.

[19] Bruch, A., Fourmigué, J. F. and Couturier, R., 2014, "Experimental and Numerical Investigation of a Pilot-Scale Thermal Oil Packed Bed Thermal Storage System for CSP Power Plant," Solar Energy, 105, p. 116-125.

[20] Ergun, S., 1952, "Fluid Flow through Packed Columns," Chemical Engineering Progress, 48 (2), p. 89-94.

[21] Wakao, N. and Kaguei, S., 1982, *Heat and Mass Transfer in Packed Beds*, Gordon and Breach Science Publishers, New York.

[22] Xu, C., Li, X., Wang, Z., He, Y. and Bai, F., 2013, "Effects of Solid Particle Properties on the Thermal Performance of a packed-Bed Molten-Salt Thermocline Thermal Storage System," Applied Thermal Engineering, 57 (1–2), p. 69-80.

[23] Yang, X., Yang, X., Ding, J., Shao, Y., Qin, F. G. F. and Jiang, R., 2012, "Criteria for Performance Improvement of a Molten Salt Thermocline Storage System," Applied Thermal Engineering, 48, p. 24-31.

[24] Aly, S. L. and El-Sharkawy, A. I., 1990, "Effect of Storage Medium on Thermal Properties of Packed Beds," Heat Recovery Systems and CHP, 10 (5–6), p. 509-517.

[25] Adebiyi, G. A., Nsofor, E. C., Steele, W. G. and Jalalzadeh-Azar, A. A., 1998, "Parametric Study on the Operating Efficiencies of a Packed Bed for High-Temperature Sensible Heat Storage," ASME Journal of Solar Energy Engineering, 120, p. 2-13.

[26] Ismail, K. A. R. and Stuginsky Jr, R., 1999, "A Parametric Study on Possible Fixed Bed Models for PCM and Sensible Heat Storage," Applied Thermal Engineering, 19 (7), p. 757-788.

[27] Xu, C., Wang, Z., He, Y., Li, X. and Bai, F., 2012, "Sensitivity Analysis of the Numerical Study on the Thermal Performance of a Packed-Bed Molten Salt Thermocline Thermal Storage System," Applied Energy, 92, p. 65-75.

[28] Yang, Z. and Garimella, S. V., 2010, "Thermal Analysis of Solar Thermal Energy Storage in a Molten-Salt Thermocline," Solar Energy, 84 (6), p. 974-985.

[29] Yang, Z. and Garimella, S. V., 2013, "Cyclic Operation of Molten-Salt Thermal Energy Storage in Thermoclines for Solar Power Plants," Applied Energy, 103, p. 256-265.

[30] Xu, C., Wang, Z., He, Y., Li, X. and Bai, F., 2012, "Parametric Study and Standby Behavior of a Packed-Bed Molten Salt Thermocline Thermal Storage System," Renewable Energy, 48, p. 1-9.

[31] Flueckiger, S. M., Iverson, B. D., Garimella, S. V. and Pacheco, J. E., 2014, "System-Level Simulation of a Solar Power Tower Plant with Thermocline Thermal Energy Storage," Applied Energy, 113, p. 86-96.

[32] Kelly, B., 2010, "Advanced Thermal Storage for Central Receivers with Supercritical Coolants," Lakewood, CO, Abengoa Solar Inc., DE-FG36-08GO18149, June 15, 2010, p. 184.

[33] Peng, H., Dong, H. and Ling, X., 2014, "Thermal Investigation of PCM-Based High Temperature Thermal Energy Storage in Packed Bed," Energy Conversion and Management, 81, p. 420-427.

[34] Wu, M., Xu, C. and He, Y.-L., 2014, "Dynamic Thermal Performance Analysis of a Molten-Salt Packed-Bed Thermal Energy Storage System Using PCM Capsules," Applied Energy, 121, p. 184-195.

[35] Nithyanandam, K., Pitchumani, R. and Mathur, A., 2014, "Analysis of a Latent Thermocline Storage System with Encapsulated Phase Change Materials for Concentrating Solar Power," Applied Energy, 113, p. 1446-1460.

[36] Pacheco, J. E., Showalter, S. K. and Kolb, W. J., 2002, "Development of a Molten-Salt Thermocline Thermal Storage System for Parabolic Trough Plants," ASME Journal of Solar Energy Engineering, 124, p. 153-159.

[37] Adebiyi, G. A., 1991, "A Second-Law Study on Packed Bed Energy Storage Systems Utilizing Phase-Change Materials," ASME Journal of Solar Energy Engineering, 113, p. 146-156.

[38] Jalalzadeh-Azar, A. A., Steele, W. G. and Adebiyi, G. A., 1996, "Heat Transfer in a High-Temperature Packed Bed Thermal Energy Storage System - Roles of Radiation and Intraparticle Conduction," Transactions of the ASME Journal of Energy Resources Technology, 118, p. 50-57.

[39] Shah, R. K., 1981, *Thermal Design Theory for Regenerators*, Hemisphere Publishing Corp., New York, p. 721-763.

[40] Wakao, N., Kaguei, S. and Funazkri, T., 1979, "Effect of Fluid Dispersion Coefficients on Particle-to-Fluid Heat Transfer Coefficients in Packed Beds: Correlation of Nusselt Numbers," Chemical Engineering Science, 34 (3), p. 325-336.

[41] Incropera, F. P., Dewitt, D. P., Bergman, T. L. and Lavine, A. S., 2007, *Introduction to Heat Transfer*, John Wiley & Sons, Hoboken, NJ.

[42] Beek, J., 1962, "Design of Packed Catalytic Reactors," Advances in Chemical Engineering, 3, p. 203-271.

[43] Gonzo, E. E., 2002, "Estimating Correlations for the Effective Thermal Conductivity of Granular Materials," Chemical Engineering Journal, 90 (3), p. 299-302.

[44] Ozisik, N., 2013, *Boundary Value Problems of Heat Conduction*, Dover Publications, p. 419.

[45] Ozisik, N. M., 1993, *Heat Conduction*, John Wiley & Sons, New York, p. 394-395.

[46] Alexiades, V. and Solomon, A. D., 1993, *Mathematical Modeling of Melting and Freezing Processes*, Hemisphere Publishing Corporation, Washington D.C., p. 180-272.

[47] Voller, V. R., 1996, *An Overview of Numerical Methods for Solving Phase Change Problems*, Taylor & Francis, London, p. 341-375.

[48] Idelsohn, S. R., Storti, M. A. and Crivelli, L. A., 1994, "Numerical Methods in Phase-Change Problems," Archives of Computational Methods in Engineering, 1, p. 49-74.

[49] Arkar, C. and Medved, S., 2005, "Influence of Accuracy of Thermal Property Data of a Phase Change Material on the Result of a Numerical Model of a Packed Bed Latent Heat Storage with Spheres," Thermochimica Acta, 438 (1–2), p. 192-201.

[50] Alisetti, E. L. and Roy, S. K., 1999, "Forced Convection Heat Transfer to Phase Change Material Slurries in Circular Ducts," Journal of Thermophysics, 14 (1), p. 115-118.

[51] Lamberg, P., Lehtiniemi, R. and Henell, A.-M., 2004, "Numerical and Experimental Investigation of Melting and Freezing Processes in Phase Change Material Storage," International Journal of Thermal Sciences, 43 (3), p. 277-287.

[52] Sinnott, R. K., 2005, *Chemical Engineering Design*, Elsevier Butterworth-Heinemann, Oxford, UK, p. 245.

[53] Huston, R. and Josephs, H., 2009, *Practical Stress Analysis in Engineering Design*, CRC Press Taylor & Francis Group, Boca Raton, FL.

[54] Singh, R. K., Singh, S. N. and Seshadri, V., 2010, "CFD Prediction of the Effects of the Upstream Elbow Fittings on the Performance of Cone Flowmeters," Flow Measurement and Instrumentation, 21 (2), p. 88-97.

[55] Bryant, J. A. and O'Neal, D. L., 1996, "Effect of a 90 Degree Elbow on the Accuracy of an Insertion Flowmeter, Results and Comparisons for 4 and 6 In. Diameter PVC Pipe", Tenth Symposium on Improving Building Systems in Hot and Humid Climates, Fort Worth, TX.

[56] Fried, E. and Idelchik, I. E., 1989, *Flow Resistance: A Design Guide for Engineers*, Hemisphere Publishing Corporation, New York, p. 391.

[57] Li, L. and Ma, W., 2011, "Experimental Study on the Effective Particle Diameter of a Packed Bed with Non-Sperical Particles," Transport in Porous Media, 89, p. 35-48.

[58] Singh, R., Saini, R. P. and Saini, J. S., 2006, "Nusselt Number and Friction Factor Correlations for Packed Bed Solar Energy Storage System Having Large Sized Elements of Different Shapes," Solar Energy, 80 (7), p. 760-771.

[59] Geldart, D., 1990, "Estimation of Basic Particle Properties for Use in Fluid-Particle Process Calculations," Powder Technology, 60, p. 1-13.

[60] Wadell, H., 1935, "Volume, Shape, and Roundness of Quartz Particles," The Journal of Geology, 43 (3), p. 250-280.

[61] Alam, T. E., Bellan, S., Dhau, J., Goswami, D. Y., Rahman, M. M., Stefanakos, E. K., Gonzalez-Aguilar, J. and Romero, M., 2014, "Experimental and Numerical Investigation of a Packed-Bed Latent Heat Thermal Storage System with Encapsulated Phase Change Material", EuroSun 2014, Aix-les-Bains, France, International Solar Energy Society, p.

[62] Alam, T. E., Dhau, J., Goswami, D. Y., Rahman, M. M. and Stefanakos, E. K., 2014, "Experimental Investigation of a Packed-Bed Latent Heat Thermal Storage System with Encapsulated Phase Change Material", International Mechanical Engineering Congress & Exposition, Montreal, Quebec, Canada, American Society of Mechanical Engineers.

[63] Bailey, C., "Carbon Steel Thermal Properties," http://www.mace.manchester.ac.uk/project/research/structures/strucfire/materialInFire/Steel/HotRolledCarbonSteel/thermalProperties.htm.

[64] Bauer, T., Laing, D., Kroner, U. and Tamme, R., 2009, "Sodium Nitrate for High Temperature Latent Heat Storage", The 11th International Conference on Thermal Energy Storage - Effstock, Stockholm, Sweden, p. 1-8.

[65] Carling, R. W., 1983, "Heat Capacities of NaNO3 and KNO3 from 350 to 800 K," Thermochimica Acta, 60, p. 265-275.

[66] Jeffreson, C. P., 1972, "Prediction of Breakthrough Curves in Packed Beds: 1. Applicability of Single Parameter Models," AIChE Journal, 18 (2), p. 409-416.

[67] Jalalzadeh-Azar, A. A., Steele, W. G. and Adebiyi, G. A., 1997, "Performance Comparison of High-Temperature Packed Bed Operation with Pcm and Sensible-Heat Pellets," International Journal of Energy Research, 21, p. 1039-1052.

[68] Nithyanandam, K. and Pitchumani, R., 2014, "Cost and Performance Analysis of Concentrating Solar Power Systems with Integrated Latent Thermal Energy Storage," Energy, 64, p. 793-810.

[69] Jegadheeswaran, S., Pohekar, S. D. and Kousksou, T., 2010, "Exergy Based Performance Evaluation of Latent Heat Thermal Storage System: A Review," Renewable and Sustainable Energy Reviews, 14 (9), p. 2580-2595.

[70] Adebiyi, G. A., Hodge, B. K., Steele, W. G., Jalalzadeh-Azar, A. A. and Nsofor, E. C., 1996, "Computer Simulation of a High-Temperature Thermal Energy Storage System Employing Multiple Families of Phase-Change Storage Materials," ASME Journal of Energy Resources Technology, 118, p. 102-111.

[71] Cui, H., Yuan, X. and Hou, X., 2003, "Thermal Performance Analysis for a Heat Receiver Using Multiple Phase Change Materials," Applied Thermal Engineering, 23 (18), p. 2353-2361.

[72] Gong, Z.-X. and Mujumdar, A. S., 1997, "Thermodynamic Optimization of the Thermal Process in Energy Storage Using Multiple Phase Change Materials," Applied Thermal Engineering, 17 (11), p. 1067-1083.

[73] Shabgard, H., Robak, C. W., Bergman, T. L. and Faghri, A., 2012, "Heat Transfer and Exergy Analysis of Cascaded Latent Heat Storage with Gravity-Assisted Heat Pipes for Concentrating Solar Power Applications," Solar Energy, 86 (3), p. 816-830.

[74] Gong, Z.-X. and Mujumdar, A. S., 1996, "Finite Element Analysis of a Multstage Latent Heat Thermal Storage System," Numerical Heat Transfer, Part A, 30, p. 669-684.

[75] Gong, Z.-X. and Mujumdar, A. S., 1996, "Exergy Analysis of Energy Storage Using Multiple Phase-Change Materials," ASME Journal of Energy Resources Technology, 118, p. 242-248.

[76] Linstrom, P. J. and Mallard, W. G., *Nist Chemistry Webbook, Nist Standard Reference Database Number 69*, National Institute of Standards and Technology, Gaithersburg, MD, 20899.

[77] Janz, G. J., Allen, C. B., Bansal, N. P., Murphy, R. M. and Tomkins, R. P. T., 1979, "Physical Properties Data Compilations Relevant to Energy Storage. Ii. Molten Salts: Data on Single and Multi-Component Salt Systems," Troy, NY, Molten Salts Data Center, NSRDS-NBS 61, Part II.

[78] Zhang, W., Thompson, K. E., Reed, A. H. and Beenken, L., 2006, "Relationship between Packing Structure and Porosity in Fixed Beds of Equilateral Cylindrical Particles," Chemical Engineering Science, 61 (24), p. 8060-8074.

[79] Kenisarin, M. M., 2010, "High-Temperature Phase Change Materials for Thermal Energy Storage," Renewable and Sustainable Energy Reviews, 14 (3), p. 955-970.

[80] *Personal Communication with SQM Corp, March 2011*.

[81] Trahan, J., Kuravi, S., Goswami, D. Y., Rahman, M. M. and Stefanakos, E. K., 2012, "Thermal Characterization of High Temperature Inorganic Phase Change Materials for Thermal Energy Storage Applications", ASME 6th International Conference on Energy Sustainability, San Diego, CA, p. 623-630.

[82] Gomez, J. C., 2011, "High-Temperature Phase Change Materials (PCM) Candidates for Thermal Energy Storage (TES) Applications," Golden, CO, National Renewable Energy Laboratory, NREL/TP-5500-51446, p. 36.

[83] Williams, D. F., 2006, "Assessment of Candidate Molten Salt Coolants for the NGNP/NHI Heat-Transfer Loop," Oak Ridge, TN, Oak Ridge National Laboratory, ORNL/TM-2006/69, p. 44.

[84] Zhao, W., Zheng, Y., Sabol, J. C., Tuzla, K., Neti, S., Oztekin, A. and Chen, J. C., 2013, "High Temperature Calorimetry and Use of Magnesium Chloride for Thermal Energy Storage," Renewable Energy, 50, p. 988-993.

[85] Nemecek, J. J., Simmons, D. E. and Chubb, T. A., 1978, "Demand Sensitive Energy Storage in Molten Salts," Solar Energy, 20, p. 213-217.

[86] Mathur, A., Kasetty, R., Oxley, J., Mendez, J. and Nithyanandam, K., 2014, "Using Encapsulated Phase Change Salts for Concentrated Solar Power Plant," Energy Procedia, 49, p. 908-915.

[87] Nandi, B. R., Bandyopadhyay, S. and Banerjee, R., 2012, "Analysis of High Temperature Thermal Energy Storage for Solar Power Plant", Sustainable Energy Technologies (ICSET), 2012 IEEE Third International Conference on, p. 438-444.

[88] 2014, "Economic Indicators," Chemical Engineering, 121 (11), p. 184-184.

[89] Couper, J. R., Penney, W. R., Fair, J. R. and Walas, S. M., 2010, "Chapter 21 - Costs of Individual Equipment," *Chemical Process Equipment (Second Edition)*, Gulf Professional Publishing, Boston, p. 717-726.

[90] Kelly, B. and Kearney, D., 2006, "Thermal Storage Commercial Plant Design Study for a 2-Tank Indirect Molten Salt System," Golden, CO, National Renewable Energy Laboratory, NREL/SR-550-40166, May 13, 2002 - December 31, 2004, p. 32.

[91] Bolen, W. P., 2014, "Salt Mineral Commodity Summaries," U.S. Geological Survey, http://minerals.usgs.gov/minerals/pubs/commodity/salt/mcs-2014-salt.pdf.

[92] Pacheco, J. E., 2002, "Final Test and Evaluation Results from the Solar Two Project,". Albuquerque, NM, Sandia National Laboratories, SAND2002-0120, January 2002, p. 294.

[93] Py, X., Calvet, N., Olives, R., Meffre, A., Echegut, P., Bessada, C., Veron, E. and Ory, S., 2011, "Recycled Material for Sensible Heat Based Thermal Energy Storage to Be Used in Concentrated Solar Thermal Power Plants," ASME Journal of Solar Energy Engineering, 133, p. 0310081-0310088.

[94] Trahan, J., Graziani, A., Goswami, D. Y., Stefanakos, E., Jotshi, C. and Goel, N., 2014, "Evaluation of Pressure Drop and Particle Sphericity for an Air-Rock Bed Thermal Energy Storage System," Energy Procedia, 57, p. 633-642.

APPENDICES

Appendix A. Nomenclature

Bi	Biot number, $h(r/3)/k_s$	*Subscripts*	
C_p	Specific heat capacity (J/kg-K)	c	Cold
$C_{p,eff}$	Effective/apparent specific heat capacity (J/kg-K)	eff	Effective
d	Tank diameter (m)	h	Hot
D_p	Particle diameter (m)	HTF	Heat transfer fluid
G	Air mass flux (kg/m^2-s)	s	Solid phase
h	Convective heat transfer coefficient (W/m^2-K)		
H	Bed height (m)		
hp	Horsepower		
k	Thermal conductivity (W/-K)		
L	Latent heat (J/kg)		
Nu	Nusselt number, hD_p/k		
Pr	Prandtl number, $c_{p,HTF}\ \mu_{HTF}/k_{HTF}$		
Re	Particle Reynolds number ($GD_p/\ \mu_{HTF}$)		
v_t	Propagation velocity of thermocline zone		
ΔP	Pressure drop (Pa)		
T	Temperature		
T_L	Liquidus temperature		
T_m	Phase change temperature		
T_S	Solidus temperature		
U	Superficial bed velocity (m/s)		
ρ	Density (kg/m^3)		
μ	Dynamic viscosity (kg/m-s)		
ε	Average bed porosity		

Appendix B. Supplemental Information on the SHS Packed Bed Prototype System

B.1 Flow Conditioners

The only design that showed favorable results for the flow from the top of the system was that of a commercially available CRV vane produced by Cheng Fluid Systems. A small prototype was built and tested by inserting the device before the elbow of the small-scale system. Figure B.2 illustrates the difference in velocity across the bed diameter when the vane is included versus when it is removed. The velocity exhibits a parabolic shape that is symmetric about the central axis when the vane is implemented. This is opposed to the situation when the conditioner is removed, wherein the velocity peaks along one wall of the bed, dips at the center of the bed, and rises slightly along the opposing wall. Due to the high cost of purchasing a large stainless steel CRV vane for the pilot-scale system, the flow conditioner was not purchased and the system was operated without any device.

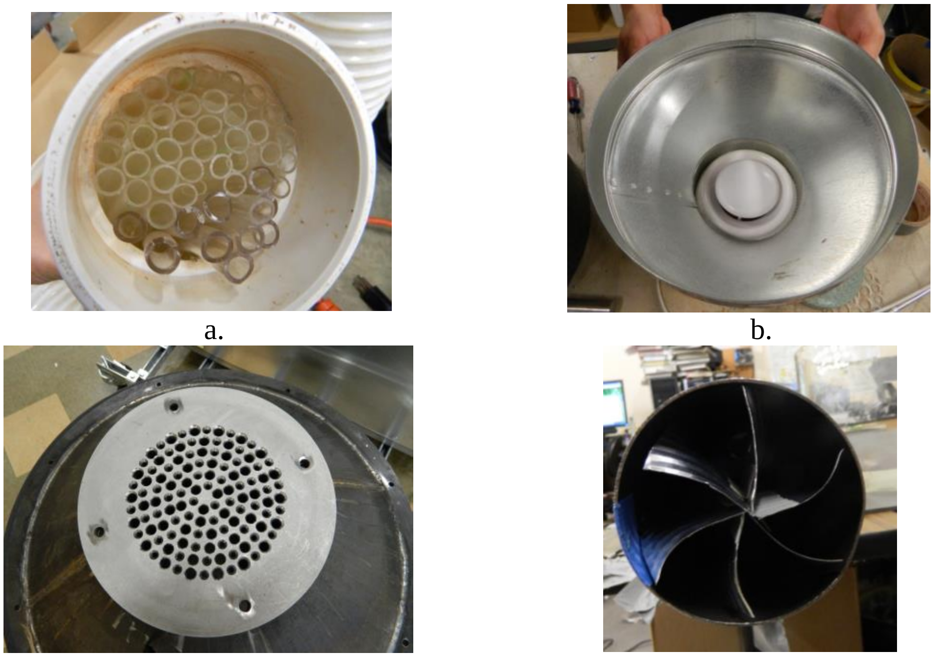

a.

b.

c.

d.

Figure B.1. Flow conditioners that were tested to examine their ability to uniformly distribute air flow. a) a tube bundle made with ClearFlex PVC tubing was placed in the elbow, b) a Deflect-o adjustable 4 inch diffuser was placed in the entrance plenum, c) stainless steel diffuser plate made with countersunk holes and placed at bottom of the lower entrance plenum, and d) handmade CRV vane made with aluminum sheeting.

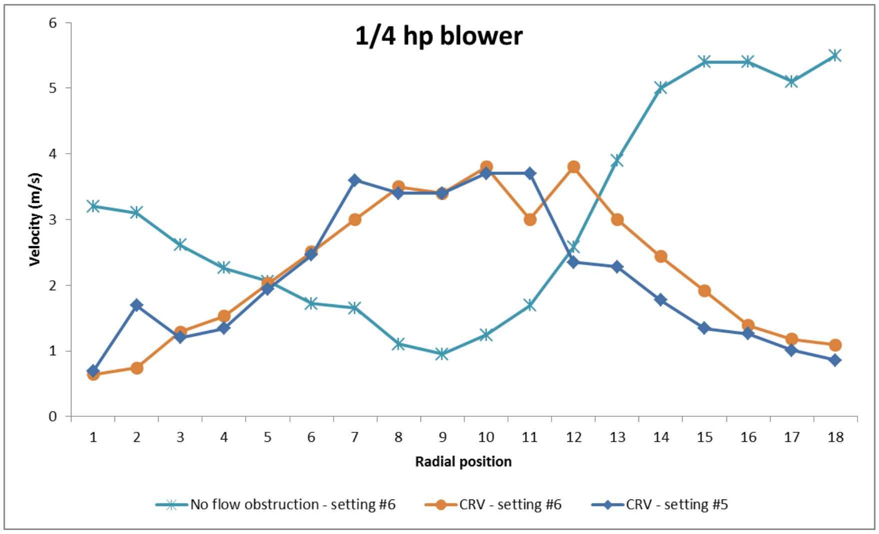

Figure B.2. Measured velocity profile across tank diameter with and without CRV vane.

B.2 Prototype System Components and Construction

The following images provide details on the construction of USF's SHS prototype system.

Figure B.3. Two 24" flanged tank sections.

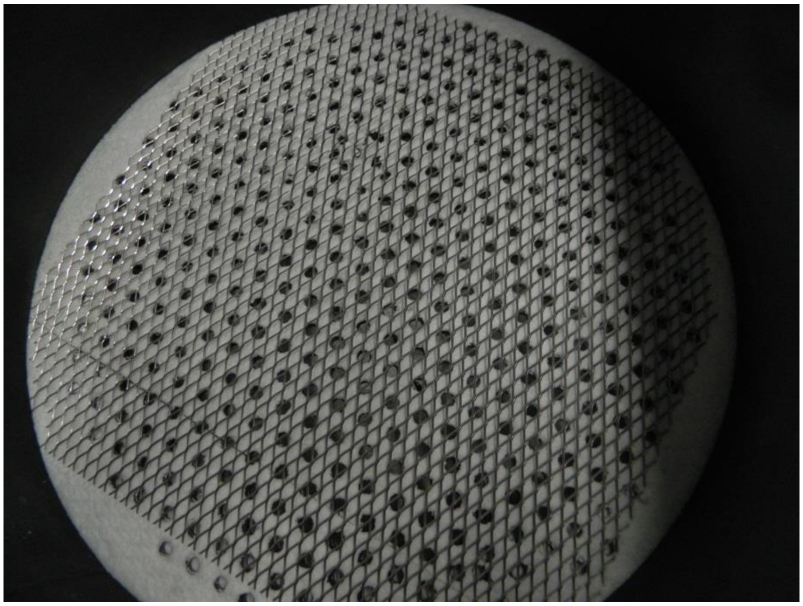

Figure B.4. Perforated packed bed plate topped with a layer of insulation and stainless steel mesh.

Figure B.5. Final system setup prior to insulating.

Figure B.6. Omega k-type thermocouples (type XCIB) used in USF’s packed bed system.

Figure B.7. Heater control system (left) and thermocouple board (right).

Appendix C. Copyright Permissions

This section includes the permissions obtained to use the copyrighted materials.

- Permission to use Figure 1 in reference [3]

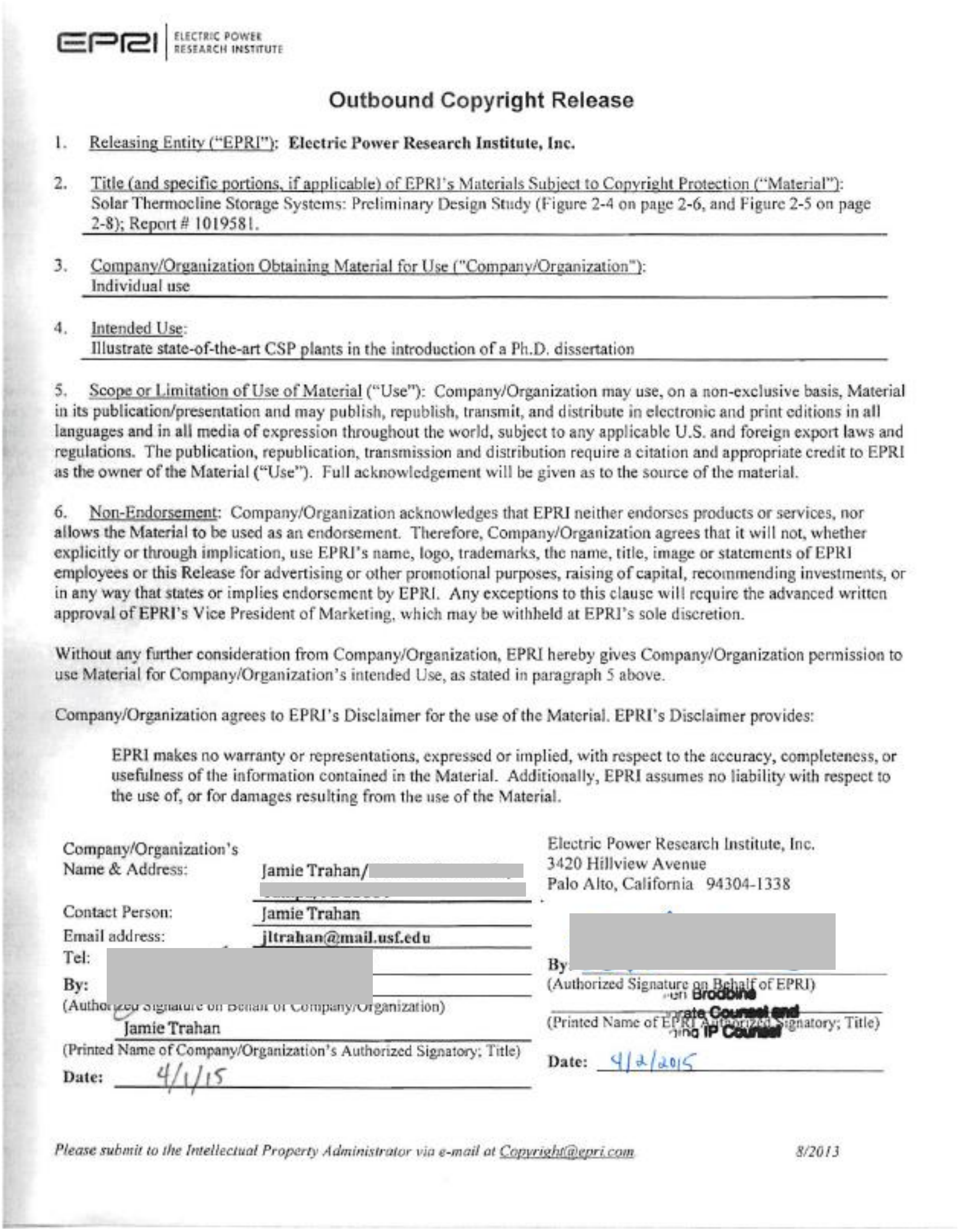

ELECTRIC POWER RESEARCH INSTITUTE

Outbound Copyright Release

1. Releasing Entity ("EPRI"): **Electric Power Research Institute, Inc.**

2. Title (and specific portions, if applicable) of EPRI's Materials Subject to Copyright Protection ("Material"): Solar Thermocline Storage Systems: Preliminary Design Study (Figure 2-4 on page 2-6, and Figure 2-5 on page 2-8); Report # 1019581.

3. Company/Organization Obtaining Material for Use ("Company/Organization"): Individual use

4. Intended Use: Illustrate state-of-the-art CSP plants in the introduction of a Ph.D. dissertation

5. Scope or Limitation of Use of Material ("Use"): Company/Organization may use, on a non-exclusive basis, Material in its publication/presentation and may publish, republish, transmit, and distribute in electronic and print editions in all languages and in all media of expression throughout the world, subject to any applicable U.S. and foreign export laws and regulations. The publication, republication, transmission and distribution require a citation and appropriate credit to EPRI as the owner of the Material ("Use"). Full acknowledgement will be given as to the source of the material.

6. Non-Endorsement: Company/Organization acknowledges that EPRI neither endorses products or services, nor allows the Material to be used as an endorsement. Therefore, Company/Organization agrees that it will not, whether explicitly or through implication, use EPRI's name, logo, trademarks, the name, title, image or statements of EPRI employees or this Release for advertising or other promotional purposes, raising of capital, recommending investments, or in any way that states or implies endorsement by EPRI. Any exceptions to this clause will require the advanced written approval of EPRI's Vice President of Marketing, which may be withheld at EPRI's sole discretion.

Without any further consideration from Company/Organization, EPRI hereby gives Company/Organization permission to use Material for Company/Organization's intended Use, as stated in paragraph 5 above.

Company/Organization agrees to EPRI's Disclaimer for the use of the Material. EPRI's Disclaimer provides:

> EPRI makes no warranty or representations, expressed or implied, with respect to the accuracy, completeness, or usefulness of the information contained in the Material. Additionally, EPRI assumes no liability with respect to the use of, or for damages resulting from the use of the Material.

Company/Organization's Name & Address: Jamie Trahan/[redacted]
[redacted]

Contact Person: Jamie Trahan

Email address: jltrahan@mail.usf.edu

Tel: [redacted]

By:

(Authorized Signature on Behalf of Company/Organization)

Jamie Trahan

(Printed Name of Company/Organization's Authorized Signatory; Title)

Date: 4/1/15

Electric Power Research Institute, Inc.
3420 Hillview Avenue
Palo Alto, California 94304-1338

[redacted]

By:

(Authorized Signature on Behalf of EPRI)

en Brodbine
rate Counsel and
ing IP Counsel

(Printed Name of EPRI Authorized Signatory; Title)

Date: 4/2/2015

Please submit to the Intellectual Property Administrator via e-mail at Copyright@epri.com *8/2013*

- Permission to use Figure 3 in reference [7]

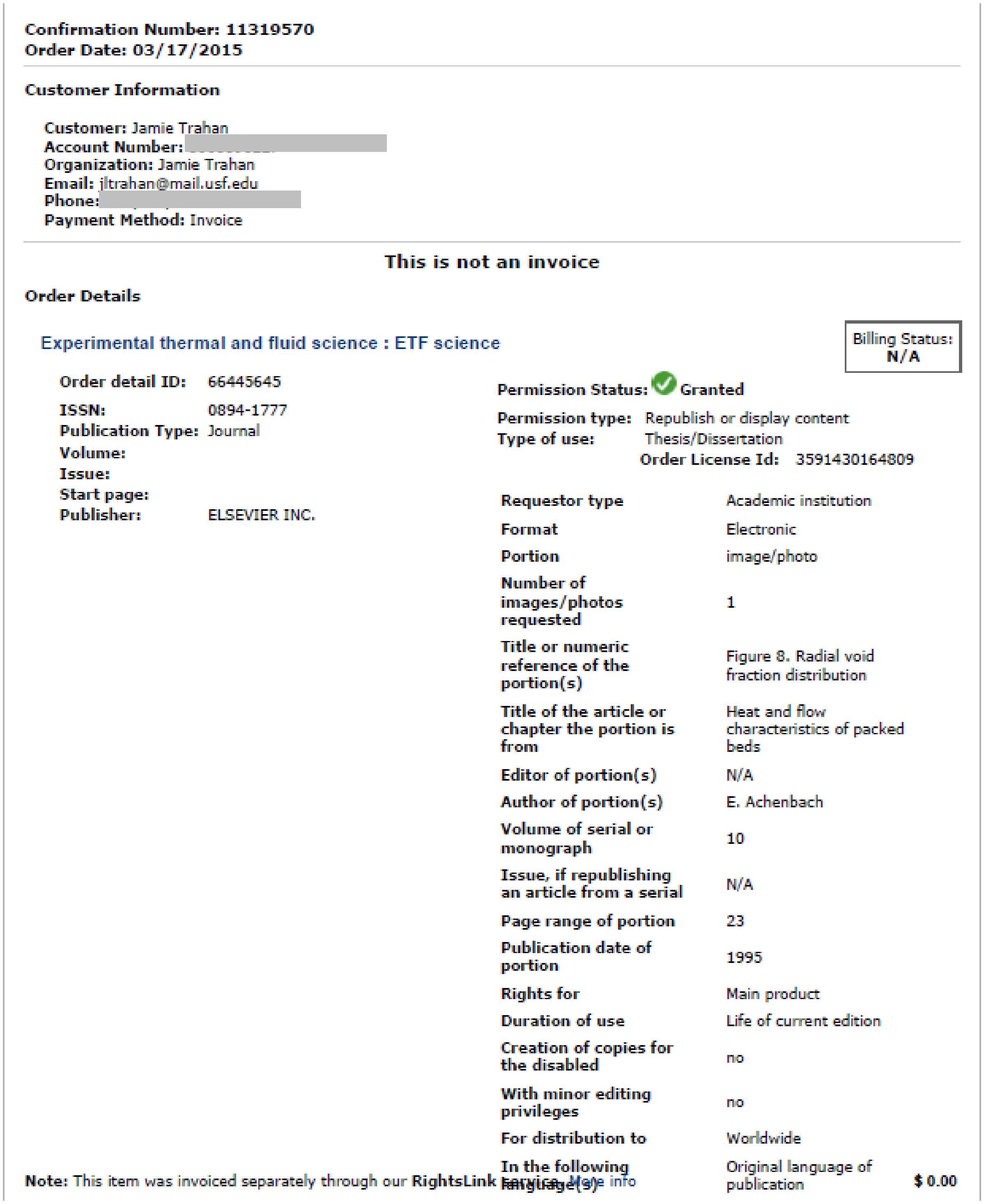

Confirmation Number: 11319570
Order Date: 03/17/2015

Customer Information

Customer: Jamie Trahan
Account Number: [redacted]
Organization: Jamie Trahan
Email: jltrahan@mail.usf.edu
Phone: [redacted]
Payment Method: Invoice

This is not an invoice

Order Details

Experimental thermal and fluid science : ETF science

Billing Status:
N/A

Order detail ID: 66445645
ISSN: 0894-1777
Publication Type: Journal
Volume:
Issue:
Start page:
Publisher: ELSEVIER INC.

Permission Status: ✓ **Granted**

Permission type: Republish or display content
Type of use: Thesis/Dissertation
Order License Id: 3591430164809

Requestor type	Academic institution
Format	Electronic
Portion	image/photo
Number of images/photos requested	1
Title or numeric reference of the portion(s)	Figure 8. Radial void fraction distribution
Title of the article or chapter the portion is from	Heat and flow characteristics of packed beds
Editor of portion(s)	N/A
Author of portion(s)	E. Achenbach
Volume of serial or monograph	10
Issue, if republishing an article from a serial	N/A
Page range of portion	23
Publication date of portion	1995
Rights for	Main product
Duration of use	Life of current edition
Creation of copies for the disabled	no
With minor editing privileges	no
For distribution to	Worldwide
In the following language(s)	Original language of publication

Note: This item was invoiced separately through our **RightsLink service.** More info

$ 0.00

- Permission to re-use previously published article [94] in Chapter 2.

Copyright Clearance Center

Confirmation Number: 11322370
Order Date: 03/20/2015

Customer Information

Customer: Jamie Trahan
Account Number: [redacted]
Organization: Jamie Trahan
Email: jltrahan@mail.usf.edu
Phone: [redacted]
Payment Method: Invoice

This is not an invoice

Order Details

Energy procedia

Billing Status:
N/A

Order detail ID:	66484392
ISSN:	1876-6102
Publication Type:	e-Journal
Volume:	
Issue:	
Start page:	
Publisher:	Elsevier Ltd

Permission Status: ✓ **Granted**

Permission type: Republish or display content
Type of use: Thesis/Dissertation
Order License Id: 3593210103932

Requestor type	Author of requested content
Format	Electronic
Portion	chapter/article
Number of pages in chapter/article	10
Title or numeric reference of the portion(s)	Pages 633-642
Title of the article or chapter the portion is from	Evaluation of Pressure Drop and Particle Sphericity for an Air-rock bed thermal energy storage system
Editor of portion(s)	Prakash Ghosh
Author of portion(s)	Jamie Trahan
Volume of serial or monograph	54
Page range of portion	633-642
Publication date of portion	2014
Rights for	Main product
Duration of use	Life of current edition
Creation of copies for the disabled	no
With minor editing privileges	no
For distribution to	Worldwide
In the following language(s)	Original language of publication

Note: This item was invoiced separately through our **RightsLink service.** More info **$ 0.00**

- Permission to use Figure 37 in reference [35]

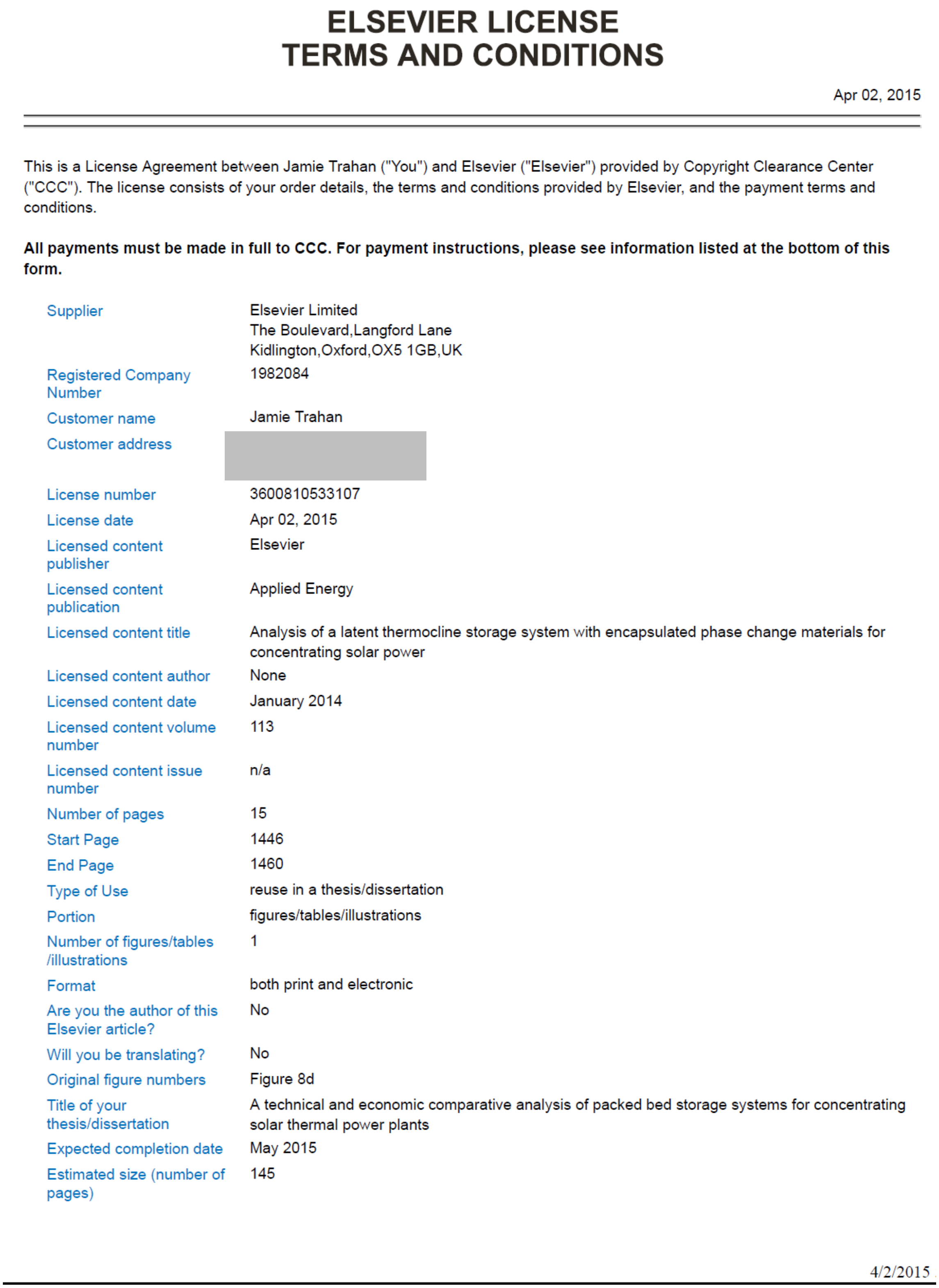

ELSEVIER LICENSE
TERMS AND CONDITIONS

Apr 02, 2015

This is a License Agreement between Jamie Trahan ("You") and Elsevier ("Elsevier") provided by Copyright Clearance Center ("CCC"). The license consists of your order details, the terms and conditions provided by Elsevier, and the payment terms and conditions.

All payments must be made in full to CCC. For payment instructions, please see information listed at the bottom of this form.

Supplier	Elsevier Limited The Boulevard,Langford Lane Kidlington,Oxford,OX5 1GB,UK
Registered Company Number	1982084
Customer name	Jamie Trahan
Customer address	[redacted]
License number	3600810533107
License date	Apr 02, 2015
Licensed content publisher	Elsevier
Licensed content publication	Applied Energy
Licensed content title	Analysis of a latent thermocline storage system with encapsulated phase change materials for concentrating solar power
Licensed content author	None
Licensed content date	January 2014
Licensed content volume number	113
Licensed content issue number	n/a
Number of pages	15
Start Page	1446
End Page	1460
Type of Use	reuse in a thesis/dissertation
Portion	figures/tables/illustrations
Number of figures/tables /illustrations	1
Format	both print and electronic
Are you the author of this Elsevier article?	No
Will you be translating?	No
Original figure numbers	Figure 8d
Title of your thesis/dissertation	A technical and economic comparative analysis of packed bed storage systems for concentrating solar thermal power plants
Expected completion date	May 2015
Estimated size (number of pages)	145

4/2/2015

Appendix D. MATLAB Code

D.1 Dispersion-Concentric Model

```
%************************Packed Bed Storage*************************
%Written by Jamie Trahan, September 1, 2014
%Updated March 6, 2015
%This code evaluates a packed bed system undergoing multiple charging/discharging
%cycles.
%Intended for single or cascaded storage.
%It is based on the dispersion concentric model.
%The implicit method is used to solve the governing equations.
%There are 2 methods of calculating effective Cp:
%1) Logistic function method
%2) Rectangular Cp method
%First and second law efficiency calculations are included.
 %********************************************************************

%Input Temperature (Celsius)
Tai = 565; %Inlet temperature of HTF
Tbi = 288; %Inlet temperature to bed during discharging.
TmaxCh = Tbi+(0.39*(Tai-Tbi)); %Maximum outlet temperature during charging.
TminDch = Tbi+(0.74*(Tai-Tbi)); %Minimum outlet temperature of HTF during discharging.
Tbini = 288; %Initial bed temperature
Tinf = 23; %Ambient temperature
Tave = (Tai+Tbi)/2; %Average temperature for air properties
TaveIn = (Tai+Tinf)/2; %Average temperature of HTF for calculating energy in

%Select the HTF to determine correct thermophysical properties.
%for HTFprops(x,Tave)
%if x = 1, HTF = Air
%if x = 2, HTF = solar salt

%HTF properties (All in SI units)(based on degrees C)
[rhoHTF,muHTF,cpHTF,kHTF] = HTFprops(2,Tave);

% Phase change material properties

thetaM1 = 0.75; %dimensionless melting temperature
thetaM2 = 0.5;
thetaM3 = 0.25;
Tmelt1 = 515; %Tbi+(thetaM1*(Tai-Tbi)); (degC)
Tmelt2 = Tbi+(thetaM2*(Tai-Tbi)); %second PCM
Tmelt3 = Tbi+(thetaM3*(Tai-Tbi)); %melting temperature of 3rd PCM
Tsolidify1 = Tmelt1;
Tsolidify2 = Tmelt2;
Tsolidify3 = Tmelt3;
Tsolidus1 = Tmelt1-1; % Lower melting temperature range (degC)
Tsolidus2 = Tmelt2-1;
Tsolidus3 = Tmelt3-1;
```

```
Tliquidus1 = Tmelt1+1; %Upper melting temperature range
Tliquidus2 = Tmelt2+1;
Tliquidus3 = Tmelt3+1;
TsolidusD1 = Tsolidify1-1; %Lower solidification temperature range (degC)
TsolidusD2 = Tsolidify2-1;
TsolidusD3 = Tsolidify3-1;
TliquidusD1 = Tsolidify1+1; %Upper solidificaiton temperature range (degC)
TliquidusD2 = Tsolidify2+1;
TliquidusD3 = Tsolidify3+1;

cpsolid = 830; % specific heat capacity of solid PCM (J/kg-K)
cpliquid = 830; % specific heat capacity of liquid PCM (J/kg-K)
cpave = (cpsolid+cpliquid)/2; %Average specific heat capacity (J/kg-K)

%InvSte1 = Lhm1/(cpave*(Tai-Tbi))
%InvSte2 = Lhm2/(cpave*(Tai-Tbi))
%InvSte3 = Lhm3/(cpave*(Tai-Tbi))

Lhm1 = 187000;  %InvSte3*(cpave*(Tai-Tbi)) ; latent heat of melting (J/kg)
Lhm2 = 187000;
Lhm3 = 187000;
Lhs1 = 187000;  %latent heat of solidification (J/kg)
Lhs2 = 187000;
Lhs3 = 187000;

% InvSte1 = Lhm1/(cpave*(Tai-Tbi))
% InvSte2 = Lhm2/(cpave*(Tai-Tbi))
% InvSte3 = Lhm3/(cpave*(Tai-Tbi))

rholiquid = 2500; % density of liquid PCM (kg/m3)
rhosolid = 2500;  % density of solid PCM (kg/m3)
rhoave = (rhosolid+rholiquid)/2;
ksolid = 5.0; %thermal conductivity of solid pcm (W/mK)
kliquid = 5.0; %conductivity of liquid (W/mK)
kave = (ksolid+kliquid)/2; %average thermal conductivity
kmelt = 1.0; %enhancement factor during melting
ksolidify = 1.0; % enhancement factor during solidification
alphalMelt = kliquid*kmelt/(rholiquid*cpliquid); %thermal diffusivity of liquid phase during melting
alphasMelt = ksolid*kmelt/(rhosolid*cpsolid); %thermal diffusivity of solid phase during melting
alphalSolidify = kliquid*ksolidify/(rholiquid*cpliquid); %thermal diffusivity of liquid phase during
melting
alphasSolidify = ksolid*ksolidify/(rhosolid*cpsolid); %thermal diffusivity of solid phase during melting
kAlumina = 5.5+(34.5*exp(-0.0033*((Tave+273)-273))); %conductivity of Alumina coating. (W/m-K)
cpAlumina = 1000*(1.0446+((1.742e-4)*(Tave+273))-((2.796e4)*(Tave+273)^-2)); %specific heat of
alumina. (J/kg-K)
rhoAlumina = 3700; %density of alumina (kg/m^3)
zeta = 9; %cp parameter

%Bed properties
ep = 0.22; %bed porosity based on outer capsule diameter volume
```

```
Di = 0.01905; %(0.02653 for NaNO3/0.01905 for SHS) particle diameter (m)
Wp = 0.00045; % Particle wall thickness (m)
Dp = Di+(2*Wp); % (Dp) Inner diameter of particle
Ro = Dp/2; %outer particle radius (m)
Ri = Di/2; %Inner radius of pellet (m)
Ap = 4*pi*(Ro^2); %Outer surface area of sphere (m2)
Vp = (4/3)*pi*(Ro^3); %volume of single sphere of PCM(m3);
Vpi = (4/3)*pi*(Ri^3);
Vcoat = Vp-Vpi; %Volume of coating of single sphere
Vratio = Vpi/Vp; %ratio of PCM volume to total sphere volume

%Bed dimensions
HrsStore = 3; %Number of hours of storage
QthermalWh = 106.5e6; %Qthermal/3600; %Required storage system energy (Wh)
Qthermal = QthermalWh*3600; %(PowerE*HrsStore*3600)/EffPB; %Required storage system energy
(joules)
mdotD = Qthermal/(cpHTF*(Tai-Tbi)*(HrsStore*3600)); %Design mass flow rate (kg/s)
PCMmassD = 3*(Qthermal/((cpsolid*(Tsolidus1+Tsolidus2+Tsolidus3-
(3*Tbini)))+Lhm1+Lhm2+Lhm3+(cpliquid*((3*Tai)-Tliquidus1-Tliquidus2-
Tliquidus3))+(cpave*(Tliquidus1+Tliquidus2+Tliquidus3-Tsolidus1-Tsolidus2-Tsolidus3)))); %design
mass of PCM
PCMvolumeD = PCMmassD/rholiquid; %Design volume of PCM
VtankD = 650; %PCMvolumeD/(1-ep); %Design tank volume.
LDratio = 0.5; %Height to diameter ratio of tank.
DbedD = 10.5925; %(((4*VtankD)/(LDratio*pi))^(1/3)); %Design bed diameter
AbedD = pi()*(DbedD^2)/4;
HbedD = VtankD/AbedD; %LDratio*DbedD; %Design bed height
Dbed = DbedD; %diameter of bed (meters)
Hbed = HbedD; %height of bed (m)
Abed = (pi*(Dbed^2))/4; %area of bed (m2)
Vtank = Abed*Hbed; %Tank volume (m^3)
VtankG = Vtank*264.172; %Tank volume (gallons)
SATank = Hbed*pi*Dbed; %Tank surface area (m^2)
Rbed = Dbed/2; %Outer tank diameter, including insulation.
Vbed = Vtank*(1-ep); %volume of  bed (m^3)
Twall = 2.0*0.0254; %thickness of steel wal1; (m)(enter inches)
Tinsul = 0.5; %thickness of insulation (m) (enter inches)
MassPCM = rhosolid*Vbed; %Total PCM mass
MassPCM1 = (1/3)*MassPCM;
MassPCM2 = (1/3)*MassPCM;
MassPCM3 = (1/3)*MassPCM;
MassHTF = Vtank*ep*rhoHTF; %Total HTF mass
%QbedMax = (MassPCM/3)*((cpsolid*(Tsolidus1+Tsolidus2+Tsolidus3-
(3*Tbini)))+Lhm1+Lhm2+Lhm3+(cpliquid*((3*Tai)-Tliquidus1-Tliquidus2-
Tliquidus3))+(cpave*(Tliquidus1+Tliquidus2+Tliquidus3-Tsolidus1-Tsolidus2-Tsolidus3)));
QbedMax = (MassPCM*(cpsolid*(Tai-
Tbi)))+(MassPCM2*Lhm2)+(MassPCM1*Lhm1)+(MassPCM3*Lhm3);
QlatentMax = (MassPCM1*Lhm1)+(MassPCM2*Lhm2)+(MassPCM3*Lhm3);

%Spatial and time parameters for bed
```

```
Nx = 296; %Number of mesh points; Number of elements = Nx-1
deltax = Hbed/(Nx-1) %mesh length (m)

%Spatial parameters for single sphere
Rx = 30;
deltar = Ri/(Rx-1);

ax = 98; % Top third of cascade ends at this grid point for charging mode
bx = 196; %Second third of cascade ends at this grid point

az = 98; % Defines grid point at bottom third of cascade during dischargin mode
bz = 196; % Defines grid point at second third of cascade during discharging mode

%Inlet flow conditions
tchmin = 10*60; %charging time in minutes
tdchmin = 10*60; %discharging time in minutes
tch = tchmin*60; %charging time in seconds
tdch = tdchmin*60; %discharging time in seconds
numcycle = 20; %number of charging/discharging cycles

% Bed Flow rate
%Input volumetric flow rate in m3/hr
mdotch = mdotD; % mass flow rate
mdotdch = mdotD; %Discharging mass flow rate (kg/s)
Vch = mdotch/(rhoHTF*Abed); %Charging superficial bed velocity (m/s)
Vdch = mdotdch/(rhoHTF*Abed); %Discharging superficial bed velocity (m/s)
Gch = mdotch/Abed; % charging HTF mass flux (kg/m2s)
Gdch = mdotdch/Abed; % Discharging HTF mass flux (kg/m2s)

Rech = rhoHTF*Vch*Dp/muHTF %muHTF; Particle Reynolds number during charging.
Redch = rhoHTF*Vdch*Dp/muHTF %Particle Reynolds number during discharging.

Pr = cpHTF*muHTF/kHTF;  %Prandtl number for HTF at Tave;

%Pressure drop calculation
Pdch =(Hbed*(Gch^2)/(1.191*(Dp)))*((1.75*(1-ep)/(ep^3))+(150*(1-ep)*muHTF/((ep^3)*Gch*Dp)))
%pressure drop (Pa)
Patm = 101325; %Atmospheric pressure in Pascals


%Effective Thermal conductivity calculations
phi = 1-ep;
beta = (ksolid-2*kHTF)/(ksolid+(2*kHTF));
Kseff = kHTF*((1+(2*beta*phi)+(((2*(beta^3))-(0.1*beta))*(phi^2))+((phi^3)*0.05*exp(4.5*beta)))/(1-
(beta*phi)));
diffu = Kseff/(ep*cpHTF*rhoHTF);  %thermal diffusivity of air


%Heat transfer coefficient based on Wakao
NuBch = (2+(1.1*(Pr^(1/3))*(Rech^0.6)));
```

```
hch = NuBch*kHTF/Dp
Bich = (hch*Dp)/(2*ksolid); %Biot number as defined in Jeffreson to calc heff.
heffch = hch/(1+0.2*Bich); %Effective heat transfer coefficient.

NuBdch = (2+(1.1*(Pr^(1/3))*(Redch^0.6)));
hdch = NuBdch*kHTF/Dp;
Bidch = (hdch*Dp)/(2*ksolid); %Biot number as defined in Jeffreson to calc heff.
heffdch = hdch/(1+0.2*Bidch); %Effective heat transfer coefficient.

%Overall heat transfer coefficient for single sphere
Rcoat = (Ri/Ro)*((Ro-Ri)/kAlumina); %Resistance due to coating (used in boundary condition)
Rextch = (1/heffch)*((Ri/Ro)^2); %External resistance (charging mode)
Rextdch = (1/heffdch)*((Ri/Ro)^2); %External resistance (discharging mode)
hoverallch = 1/(Rextch+Rcoat); %Overall heat transfer coefficient for single sphere.
hoveralldch = 1/(Rextdch+Rcoat); %Overall heat transfer coefficient for single sphere.

%Overall heat transfer coefficient for bed
hoverallVch = hoverallch*6*(1-ep)/Dp;
hoverallVdch = hoveralldch*6*(1-ep)/Dp;

%Heat loss calculations:
%Inner Wall heat transfer coefficient from Beek
hwall = (kHTF/Dp)*((0.203*(Rech^(1/3))*(Pr^(1/3)))+(0.22*(Rech^0.8)*(Pr^0.4)));
kinsul = 0.06; %insulation thermal conductivity (W/mK)
%http://www.mace.manchester.ac.uk/project/research/structures/strucfire/materialInFire/Steel/HotRolled
CarbonSteel/thermalProperties.htm
%ksteel = 54-Tave*(0.0333); %Carbon steel thermal conductivity for 20C < Tsteel < 800C (W/mK)
ksteel = 14.6+(Tave*1.27e-2); %thermal conductivity of stainless steel (W/m-K)
%Stainless props from
http://www.mace.manchester.ac.uk/project/research/structures/strucfire/materialInFire/Steel/StainlessStee
l/thermalProperties.htm
term1 = (1/hwall);
term2 = (Rbed/ksteel)*(log((Rbed+Twall)/Rbed));
term3 = (Rbed/kinsul)*(log((Rbed+Twall+Tinsul)/(Rbed+Twall)));
Uloss = 1/(term1+term2+term3); %(W/m^2-K)



%**************************************************************************
%**************************************************************************

%Time step conditions
deltat = 1;  % (sec)
Nt = tch/deltat; % Number of time steps during charging

%Define number of columns to store data
tz = 1; %Increment of minutes to store in excel.
tcolumn = (1/deltat)*60*tz  %In order to store data every 1 min, this specifies the number of time steps in
1 minute.
numcolumnch = (tchmin/tz); %Number of columns in excel spreadsheet to store data every 1 min.
```

```
cyclestepch = tchmin/tz;  %Defines number of times to execute cycle to store 1 min of data.
numcolumndch = (tdchmin/tz); %Number of columns in excel spreadsheet to store data every 1 min.
cyclestepdch = tdchmin/tz;  %Defines number of times to execute cycle to store 1 min of data.


%Temperature Calculations
Ta = zeros(Nx,numcolumnch);
Tb = zeros(Nx,numcolumnch); %volume weighted average temperature of sphere for each row m.
TaD = zeros(Nx,numcolumnch);
TbD = zeros(Nx,numcolumnch);
TaStIni = zeros(Nx,1);
TbStIni = zeros(Nx,1);

TbAve = zeros(Rx,1); %stores average sphere temperature (charging mode)
TbAveD = zeros(Rx,1); %stores average sphere temperature (discharging mode)
Tbcenter = zeros(Nx,numcolumnch); %Stores center of sphere temperature (charging mode)
Tbfirst = zeros(Nx,numcolumnch); %Stores surface of sphere temperature (charging mode)
Tbhalf = zeros(Nx,numcolumnch); %Stores quarter of sphere temperature (charging mode)
TbcenterD = zeros(Nx,numcolumnch); %Stores center of sphere temperature (discharging mode)
TbfirstD = zeros(Nx,numcolumnch); %Stores surface of sphere temperature (discharging mode)
TbhalfD = zeros(Nx,numcolumnch); %Stores quarter of sphere temperature (discharging mode)

Ts = zeros (Rx,tcolumn); %Matrix to store each element within the sphere
sphSt = zeros(Rx,Nx);  %Matrix to store the sphere of each height along bed. (charging mode)
sphDSt = zeros(Rx,Nx);
sphStIni= zeros(Rx,Nx);

%A = sparse(Rx,Rx); %Creates a sparse coefficient matrix for implicit method
A = zeros(Rx,Rx); %PCM Coefficient matrix (charging mode)
b = zeros(Rx,1); %PCM Right hand side vector (charging mode)
x = zeros(Rx,1); %PCM solution vector (charging mode)

J = zeros(Nx,Nx-1); %HTF Coefficient Matrix (charging mode)
c = zeros(Nx,1); %HTF right hand side vector (charging mode)
TaSt = zeros(Nx,1); %HT solution matrix (charging mode)
TbSt = zeros(Nx,1); %Stores PCM average sphere temperature (charging mode)
Lf = zeros(Rx,Nx); %Stores liquid fraction of each control volume in capsules.
LfD = zeros(Rx,Nx);
qCh = zeros(Rx,Nx); %Stores energy stored for each control volume in capsules.
qSCh = zeros(Rx,Nx); qLCh = zeros(Rx,Nx);

B = zeros(Rx,Rx); %PCM Coefficient matrix (discharging mode)
g = zeros(Rx,1); %PCM right hand side vector (discharging mode)
z = zeros(Nx,1); %PCM solution matrix (discharging mode)
K = zeros(Nx,Nx-1); %HTF Coefficient matrix (discharging mode)
d = zeros(Nx,1); %HTF right hand side vector (discharging mode)
TaDSt = zeros(Nx,1); %HTF solution matrix (discharging mode)
TbDSt = zeros(Nx,1); %Stores PCM average sphere temperature (discharging mode)

Chargetime = zeros(numcycle,1); Dischargetime = zeros(numcycle,1);
```

```
qChTotal = zeros(numcycle,1);   sChTotal = zeros(numcycle,1);    exChTotal = zeros(numcycle,1);
qSChTotal = zeros(numcycle,1); qLChTotal = zeros(numcycle,1);
EstoreHat = zeros(numcycle,1);  SstoreHat = zeros(numcycle,1);   ExstoreHat = zeros(numcycle,1);
QInNetCh = zeros(cyclestepch,numcycle); EinNetch = zeros(numcycle,1);

QlossCh = zeros(cyclestepch,numcycle);
Exloss = zeros(Nx,1); ExEffCh = zeros(numcycle,1);
NetExIn = zeros(cyclestepch,numcycle);  EsaltStore = zeros(numcycle,1);
ExlossCh = zeros(cyclestepch,numcycle); ExHTFChNetIn = zeros(numcycle,1);
EoutflowC = zeros(tchmin,numcycle); %Vector stores the energy removed from the bed during charging
at each minute.
EoutflowD = zeros(tdchmin,numcycle); %This vector stores the energy discharged from air at each
minute.
ExpcmLCh = zeros(Nx,1);  effectivenessCh = zeros(numcycle,1);
Estorech = zeros(numcycle,1); ExSaltStore = zeros(numcycle,1);
EstoreCh = zeros(numcycle,1); %Energy stored for given cycle
EffCh = zeros(numcycle,1); %Efficiency for given cycle
CapFact = zeros(numcycle,1); CapFactL = zeros(numcycle,1); CapFactS = zeros(numcycle,1);

qDch = zeros(Rx,Nx); sDch =  zeros(Rx,Nx); exDch = zeros(Rx,Nx);
qDchTotal = zeros(numcycle,1); exDchTotal = zeros(numcycle,1);
qSDchTotal = zeros(numcycle,1); qLDchTotal = zeros(numcycle,1);
QoutDch = zeros(cyclestepdch,1);  ExHTFDchNetOut = zeros(numcycle,1); SoutDch =
zeros(cyclestepdch,1);
QlossDch = zeros(cyclestepdch,numcycle);  NetExOut = zeros(cyclestepdch,numcycle);
EoutDch = zeros(numcycle,1);
EffDch = zeros(numcycle,1); EffOverall = zeros(numcycle,1); EffOverallT = zeros(numcycle,1);
ExEffDch = zeros(numcycle,1); ExEffOverall = zeros(numcycle,1);  ExEffOverallT = zeros(numcycle,1);

SensibleOut = zeros(numcycle,1); %Sensible energy extracted during discharging
LatentOut = zeros(numcycle,1); %Latent energy extracted during discharging
Utotal = zeros(numcycle,1); %Total Utilization factor
Usensible = zeros(numcycle,1); %Sensible heat Utilization factor
Ulatent = zeros(numcycle,1); %Latent heat Utilization factor
LatentRatio = zeros(numcycle,1); %Ratio of latent discharged over max.
LatentStore = zeros(numcycle,1); %Ratio of latent stored over max.
LatentEff =  zeros(numcycle,1);    SensibleEff = zeros(numcycle,1);


%Creating an excel spreadsheet for each cycle

for i = 1:1:(numcycle*2)
    xlssheetnames(i) = {['Sheet',int2str(i)]};
end

for j = 1:1:numcycle %Creating a table to store the last temperature of each charging cycle.
    xlrange(j) = {['B',int2str(j)]};
end

for k = 1:1:numcycle %Creating a table to store the last temperature of each discharging cycle.
```

```
    xlrangedch(k) = {['C',int2str(k)]};
end


%***********************Start charging conditions: **********************
%**********************************************************************


for m = 1:1:Nx %air Initial condition; note that t= 1 is before heating starts.
    Ta(m,1) = Tbini;
end
TaStIni(:,1)=Tbini;

%Solid Initial conditions; at time = 1, heating hasn't started.
Ts(:,1) = Tbini;
sphSt(:,:) = Tbini;
sphStIni(:,:) = Tbini;
TaSt(:,1) = Tbini;
c(1) = Tbini;
TbStIni(:,1) = Tbini;

%Creating a table for HTF inlet temperature boundary condition for each
%minute
%Taia = xlsread('NaNO3inletSolidify151.xlsx','Sheet1','B1:B202');


%HTF Boundary conditions
for j = 2:1:tcolumn  %HTF Boundary condition
     Ta(1,j) = Tai;
end

FolMelt = alphalMelt*deltat/(deltar^2); %Fourier number for liquid phase during melting
FosMelt = alphasMelt*deltat/(deltar^2); %Fourier number for solid phase during melting
FolSolid = alphalSolidify*deltat/(deltar^2); %Fourier number for liquid phase during solidification
FosSolid = alphasSolidify*deltat/(deltar^2); %Fourier number for solid phase during solidification
Be = deltat/(rhoHTF*cpHTF*ep); %Fourier number for HTF
currentdigits = digits;

 %Coefficient matrix for Charging HTF Temperature
for n = 2:1:Nx-1
     J(n,n-1) = (-Be*Gch*cpHTF/deltax)-(diffu*deltat/(deltax^2));
     J(n,n) =
1+(Gch*cpHTF*Be/deltax)+(hoverallVch*Be)+(Uloss*Dbed*pi*Be/Abed)+(2*diffu*deltat/(deltax^2));
     J(n,n+1) = -diffu*deltat/(deltax^2);
 end
 J(Nx,Nx-1) = (-Be*Gch*cpHTF/deltax)-(2*diffu*deltat/(deltax^2));
 J(Nx,Nx) =
1+(Gch*cpHTF*Be/deltax)+(hoverallVch*Be)+(Uloss*Dbed*pi*Be/Abed)+(2*diffu*deltat/(deltax^2));
 J(1,1) = 1;
```

```
 %Coefficient matrix for Discharging HTF Temperature
for n = 2:1:Nx-1
     K(n,n-1) = (-Be*Gdch*cpHTF/deltax)-(diffu*deltat/(deltax^2));
     K(n,n) =
1+(Gdch*cpHTF*Be/deltax)+(hoverallVdch*Be)+(Uloss*Dbed*pi*Be/Abed)+(2*diffu*deltat/(deltax^2)
);
     K(n,n+1) = -diffu*deltat/(deltax^2);
 end
 K(Nx,Nx-1) = (-Be*Gdch*cpHTF/deltax)-(2*diffu*deltat/(deltax^2));
 K(Nx,Nx) =
1+(Gdch*cpHTF*Be/deltax)+(hoverallVdch*Be)+(Uloss*Dbed*pi*Be/Abed)+(2*diffu*deltat/(deltax^2)
);
 K(1,1) = 1;


count = 1;  %defining excel spreadsheet to place data

for q = 1:1:numcycle
 breakflag = false; %Flag to break from outer loop
%Bed and air temperature calculations - Charging Mode
    for t = 1:1:cyclestepch

         %Charging HTF equation constants

         for i = 1:1:(tcolumn)  %Calculating tz minutes of charging."i" is each time step

             if TaSt(Nx,1) >= TmaxCh
              breakflag = true;
              break
             end

             c(1) = Tai;
             for m = 2:1:Nx
                 c(m,1) = TaSt(m,1)+(hoverallVch*Be*sphSt(1,m))+(Tinf*(Uloss*Dbed*pi*Be/Abed));
             end

             TaSt = J\c;

             for m = 1:1:ax    %1:1:Nx/3
                 for n = 2:1:Rx-1
                    rx = Ri-((n-1)*deltar);
                    if sphSt(n,m) > Tliquidus1
                        A(n,n-1) = -(FolMelt+(FolMelt*deltar/rx));
                        A(n,n) = (2*FolMelt)+1;
                        A(n,n+1) = (FolMelt*deltar/rx)-FolMelt;
                    end
                    if  (Tliquidus1 >= sphSt(n,m)) && (sphSt(n,m)>=Tsolidus1)
                        %Cp = cpsolid+((cpliquid-cpsolid)*(1/(1+exp(-zeta*(sphSt(n,m)-
Tmelt)))))+((Lhm*zeta)/((exp(-zeta*(sphSt(n,m)-Tmelt)))+(exp(zeta*(sphSt(n,m)-Tmelt)))+2));
                        Cp = cpave+(Lhm1/(Tliquidus1-Tsolidus1));
```

```
            Fop1 = (kave*kmelt*deltat)/(rhoave*Cp*(deltar^2));
            A(n,n-1) = -(Fop1+(Fop1*deltar/rx));
            A(n,n) = (2*Fop1)+1;
            A(n,n+1) = (Fop1*deltar/rx)-Fop1;

         end

         if sphSt(n,m) < Tsolidus1
            A(n,n-1) = -(FosMelt+(FosMelt*deltar/rx));
            A(n,n) = (2*FosMelt)+1;
            A(n,n+1) = (FosMelt*deltar/rx)-FosMelt;
         end
       end
      %Surface of sphere boundary condition
      A(1,1) = hoverallch+(ksolid*kmelt/deltar);
      A(1,2) = -ksolid*kmelt/deltar;

      %Center of sphere boundary condition
      if sphSt(Rx,m) > Tliquidus1
         A(Rx,Rx-1) = -6*FolMelt;
         A(Rx,Rx) = 1+(6*FolMelt);
      end
      if (Tliquidus1 >= sphSt(Rx,m)) && (sphSt(Rx,m)>=Tsolidus1)
         %Cp = cpsolid+((cpliquid-cpsolid)*(1/(1+exp(-zeta*(sphSt(Rx,m)-Tmelt)))))+((Lhm*zeta)/((exp(-zeta*(sphSt(Rx,m)-Tmelt)))+(exp(zeta*(sphSt(Rx,m)-Tmelt)))+2));
         Cp = cpave+(Lhm1/(Tliquidus1-Tsolidus1));
         Fop1 = (kave*kmelt*deltat)/(rhoave*Cp*(deltar^2));
         A(Rx,Rx-1) = -6*Fop1;
         A(Rx,Rx) = 1+(6*Fop1);
      end

      if sphSt(Rx,m) < Tsolidus1
         A(Rx,Rx-1) = -6*FosMelt;
         A(Rx,Rx) = 1+(6*FosMelt);
      end
      %Calculate new temperature
       b(2:Rx) = sphSt(2:Rx,m);
       b(1) = hoverallch*TaSt(m,1);

       x = A\b;

       sphSt(:,m) = x(:,1);
    end

    for m = (ax+1):1:bx %((Nx/3)+1):1:(2*Nx/3)
       for n = 2:1:Rx-1
         rx = Ri-((n-1)*deltar);
         if sphSt(n,m) > Tliquidus2
            A(n,n-1) = -(FolMelt+(FolMelt*deltar/rx));
            A(n,n) = (2*FolMelt)+1;
```

```
           A(n,n+1) = (FolMelt*deltar/rx)-FolMelt;
        end
        if  (Tliquidus2 >= sphSt(n,m)) && (sphSt(n,m)>=Tsolidus2)
           %Cp = cpsolid+((cpliquid-cpsolid)*(1/(1+exp(-zeta*(sphSt(n,m)-
Tmelt)))))+((Lhm*zeta)/((exp(-zeta*(sphSt(n,m)-Tmelt)))+(exp(zeta*(sphSt(n,m)-Tmelt)))+2));
           Cp = cpave+(Lhm2/(Tliquidus2-Tsolidus2));
           Fop1 = (kave*kmelt*deltat)/(rhoave*Cp*(deltar^2));
           A(n,n-1) = -(Fop1+(Fop1*deltar/rx));
           A(n,n) = (2*Fop1)+1;
           A(n,n+1) = (Fop1*deltar/rx)-Fop1;

        end

        if sphSt(n,m) < Tsolidus2
           A(n,n-1) = -(FosMelt+(FosMelt*deltar/rx));
           A(n,n) = (2*FosMelt)+1;
           A(n,n+1) = (FosMelt*deltar/rx)-FosMelt;
        end
       end
      %Surface of sphere boundary condition
      A(1,1) = hoverallch+(ksolid*kmelt/deltar);
      A(1,2) = -ksolid*kmelt/deltar;

      %Center of sphere boundary condition
      if sphSt(Rx,m) > Tliquidus2
         A(Rx,Rx-1) = -6*FolMelt;
         A(Rx,Rx) = 1+(6*FolMelt);
      end
      if (Tliquidus2 >= sphSt(Rx,m)) && (sphSt(Rx,m)>=Tsolidus2)
         %Cp = cpsolid+((cpliquid-cpsolid)*(1/(1+exp(-zeta*(sphSt(Rx,m)-
Tmelt)))))+((Lhm*zeta)/((exp(-zeta*(sphSt(Rx,m)-Tmelt)))+(exp(zeta*(sphSt(Rx,m)-Tmelt)))+2));
         Cp = cpave+(Lhm2/(Tliquidus2-Tsolidus2));
         Fop1 = (kave*kmelt*deltat)/(rhoave*Cp*(deltar^2));
         A(Rx,Rx-1) = -6*Fop1;
         A(Rx,Rx) = 1+(6*Fop1);
      end

      if sphSt(Rx,m) < Tsolidus2
         A(Rx,Rx-1) = -6*FosMelt;
         A(Rx,Rx) = 1+(6*FosMelt);
      end

      %Calculate new temperature
       b(2:Rx) = sphSt(2:Rx,m);
       b(1) = hoverallch*TaSt(m,1);

       x = A\b;

       sphSt(:,m) = x(:,1);
    end
```

```
        for m = (bx+1):1:Nx    %((2*Nx/3)+1):1:Nx
          for n = 2:1:Rx-1
            rx = Ri-((n-1)*deltar);
            if sphSt(n,m) > Tliquidus3
               A(n,n-1) = -(FolMelt+(FolMelt*deltar/rx));
               A(n,n) = (2*FolMelt)+1;
               A(n,n+1) = (FolMelt*deltar/rx)-FolMelt;
            end
            if  (Tliquidus3 >= sphSt(n,m)) && (sphSt(n,m)>=Tsolidus3)
               %Cp = cpsolid+((cpliquid-cpsolid)*(1/(1+exp(-zeta*(sphSt(n,m)-
Tmelt)))))+((Lhm*zeta)/((exp(-zeta*(sphSt(n,m)-Tmelt)))+(exp(zeta*(sphSt(n,m)-Tmelt)))+2));
               Cp = cpave+(Lhm3/(Tliquidus3-Tsolidus3));
               Fop1 = (kave*kmelt*deltat)/(rhoave*Cp*(deltar^2));
               A(n,n-1) = -(Fop1+(Fop1*deltar/rx));
               A(n,n) = (2*Fop1)+1;
               A(n,n+1) = (Fop1*deltar/rx)-Fop1;

            end

            if sphSt(n,m) < Tsolidus3
               A(n,n-1) = -(FosMelt+(FosMelt*deltar/rx));
               A(n,n) = (2*FosMelt)+1;
               A(n,n+1) = (FosMelt*deltar/rx)-FosMelt;
            end
          end
         %Surface of sphere boundary condition
         A(1,1) = hoverallch+(ksolid*kmelt/deltar);
         A(1,2) = -ksolid*kmelt/deltar;

         %Center of sphere boundary condition
         if sphSt(Rx,m) > Tliquidus3
            A(Rx,Rx-1) = -6*FolMelt;
            A(Rx,Rx) = 1+(6*FolMelt);
         end
         if (Tliquidus3 >= sphSt(Rx,m)) && (sphSt(Rx,m)>=Tsolidus3)
            %Cp = cpsolid+((cpliquid-cpsolid)*(1/(1+exp(-zeta*(sphSt(Rx,m)-
Tmelt)))))+((Lhm*zeta)/((exp(-zeta*(sphSt(Rx,m)-Tmelt)))+(exp(zeta*(sphSt(Rx,m)-Tmelt)))+2));
            Cp = cpave+(Lhm3/(Tliquidus3-Tsolidus3));
            Fop1 = (kave*kmelt*deltat)/(rhoave*Cp*(deltar^2));
            A(Rx,Rx-1) = -6*Fop1;
            A(Rx,Rx) = 1+(6*Fop1);
         end

         if sphSt(Rx,m) < Tsolidus3
            A(Rx,Rx-1) = -6*FosMelt;
            A(Rx,Rx) = 1+(6*FosMelt);
         end
          %Calculate new temperature
          b(2:Rx) = sphSt(2:Rx,m);
```

```
     b(1) = hoverallch*TaSt(m,1);

     x = A\b;

     sphSt(:,m) = x(:,1);
   end


end

%Calculation of volume averaged solid temperature:
for m = 1:1:Nx
  %Average sphere temperature at first control volume of sphere:
  TbAve(1) = ((4/3)*pi*((Ri^3)-((Ri-(deltar/2))^3)))*sphSt(1,m);
  for n = 2:1:Rx-1
     rx1 = Ri-((n-1)*deltar);
     v1 = ((4/3)*pi*((rx1+(deltar/2))^3));
     v2 = ((4/3)*pi*((rx1-(deltar/2))^3));
     TbAve(n) = (v1-v2)*sphSt(n,m);
  end
  %Average sphere temperature at center of sphere.
  TbAve(Rx) = (4/3)*pi*((deltar/2)^3)*(sphSt(Rx,m));

  TbSt(m,1) = sum(TbAve)/Vpi;
end

Tbfirst(:,t) = sphSt(2,:).';
Tbcenter(:,t) = sphSt(Rx,:).';
Tbhalf(:,t) = sphSt((Rx/2),:).';
Ta(:,t) = TaSt(:,1);
Tb(:,t) = TbSt(:,1);

%Exporting the (tz)th minute into excel:
Taircharge(1,t) = t*tz; %Places the number of minutes of charging in the 1st row.
Tbedcharge(1,t) = t*tz; %Note that the 1st column is reserved for the initial time.
Tbedcenter(1,t) = t*tz;
Tbedfirst(1,t) = t*tz;
Tbedhalf(1,t) = t*tz;
for m = 2:Nx+1     %Places the last time step in the correct column of the excel table.
   Taircharge(m,t) = Ta(m-1,t);
   Tbedcharge(m,t) = Tb(m-1,t);
   Tbedcenter(m,t) = Tbcenter(m-1,t);
   Tbedfirst(m,t) = Tbfirst(m-1,t);
   Tbedhalf(m,t) = Tbhalf(m-1,t);
end


%Calculating the net amount of energy into the bed at each
%minute:
QInNetCh(t,q) = mdotch*cpHTF*(Tai-TaSt(Nx,1))*60;
```

```
        %EoutflowC(t) = Qoutch;

        %Calculating total heat loss of out system at each minute:
        QlossCh(t,q) = (Uloss*Dbed*pi*deltax*sum(Tinf-TaSt(:,1))*60);

        %Calculating Net Exergy into system per minute:
        NetExIn(t,q) = mdotch*cpHTF*((Tai+273.15)-(TaSt(Nx)+273.15)-
((Tinf+273.15)*log((Tai+273.15)/(TaSt(Nx)+273.15))))*60;



        if breakflag == true
            break
        end
    end

    Chargetime(q) = t-1 %Charging time in minutes

    %Calculating energy stored in tank:
    for m = 1:1:Nx
          if (m >=1) && (m <= ax) %(m >= 1) && (m <= (Nx/3))
              Tliquidus = Tliquidus1;
              Tsolidus = Tsolidus1;
              Lhm = Lhm1;
              Tmelt = Tmelt1;
          end
          if (m > ax) && (m<= bx) %(m > (Nx/3)) && (m <= (2*Nx/3))
              Tliquidus = Tliquidus2;
              Tsolidus = Tsolidus2;
              Lhm = Lhm2;
              Tmelt = Tmelt2;
          end
          if (m > bx) && (m <= Nx)   %(m > (2*Nx/3)) && (m <= Nx)
              Tliquidus = Tliquidus3;
              Tsolidus = Tsolidus3;
              Lhm = Lhm3;
              Tmelt = Tmelt3;
          end

       %Average energy stored at first control volume of sphere:
           vo = (((4/3)*pi*((Ri^3)-((Ri-(deltar/2))^3)))*Abed*(1-ep)*deltax)/Vpi;
           if sphSt(1,m) > Tliquidus
               Lf(1,m) = 1;
               qCh(1,m) = vo*rholiquid*((cpliquid*(sphSt(1,m)-Tliquidus))+Lhm+(cpsolid*(Tsolidus-
Tbini))+(cpave*(Tliquidus-Tsolidus)));
               qSCh(1,m) = vo*rholiquid*((cpliquid*(sphSt(1,m)-Tliquidus))+(cpsolid*(Tsolidus-
Tbini))+(cpave*(Tliquidus-Tsolidus)));
               qLCh(1,m) = vo*rholiquid*Lhm;
           end
           if (Tliquidus >= sphSt(1,m)) && (sphSt(1,m)>=Tsolidus)
```

```
         Lf(1,m) = (sphSt(1,m)-Tsolidus)/(Tliquidus-Tsolidus);
         qCh(1,m) = vo*rholiquid*((Lf(1,m)*Lhm)+(cpsolid*(Tsolidus-Tbini)));
         qSCh(1,m) = vo*rholiquid*(cpsolid*(Tsolidus-Tbini));
         qLCh(1,m) = vo*rholiquid*(Lf(1,m)*Lhm);
      end
      if sphSt(1,m)<Tsolidus
         Lf(1,m) = 0;
         qCh(1,m) = vo*rhosolid*cpsolid*(sphSt(1,m)-Tbini);
         qSCh(1,m) = vo*rhosolid*cpsolid*(sphSt(1,m)-Tbini);
         qLCh(1,m) = 0;
      end
      for n = 2:1:Rx-1
         rx1 = Ri-((n-1)*deltar);
         v1 = ((4/3)*pi*((rx1+(deltar/2))^3));
         v2 = ((4/3)*pi*((rx1-(deltar/2))^3));
         vi = ((v1-v2)*Abed*(1-ep)*deltax)/Vpi;
         if sphSt(n,m) > Tliquidus
            Lf(n,m) = 1;
            qCh(n,m) = vi*rholiquid*((cpliquid*(sphSt(n,m)-Tliquidus))+Lhm+(cpsolid*(Tsolidus-Tbini))+(cpave*(Tliquidus-Tsolidus)));
            qSCh(n,m) = vi*rholiquid*((cpliquid*(sphSt(n,m)-Tliquidus))+(cpsolid*(Tsolidus-Tbini))+(cpave*(Tliquidus-Tsolidus)));
            qLCh(n,m) = vi*rholiquid*Lhm;
         end
         if (Tliquidus >= sphSt(n,m)) && (sphSt(n,m)>=Tsolidus)
            Lf(n,m) = (sphSt(n,m)-Tsolidus)/(Tliquidus-Tsolidus);
            qCh(n,m) = vi*rholiquid*((Lf(n,m)*Lhm)+(cpsolid*(Tsolidus-Tbini)));
            qSCh(n,m) = vi*rholiquid*(cpsolid*(Tsolidus-Tbini));
            qLCh(n,m) = vi*rholiquid*(Lf(n,m)*Lhm);
         end
         if sphSt(n,m)<Tsolidus
            Lf(n,m) = 0;
            qCh(n,m) = vi*rhosolid*cpsolid*(sphSt(n,m)-Tbini);
            qSCh(n,m) = vi*rhosolid*cpsolid*(sphSt(n,m)-Tbini);
            qLCh(n,m) = 0;

         end
      end
      %Energy stored at center of sphere:
      vc = (4/3)*pi*((deltar/2)^3)*Abed*(1-ep)*deltax/Vpi;
      if sphSt(Rx,m) > Tliquidus
         Lf(Rx,m) = 1;
         qCh(Rx,m) = vc*rholiquid*((cpliquid*(sphSt(Rx,m)-Tliquidus))+Lhm+(cpsolid*(Tsolidus-Tbini))+(cpave*(Tliquidus-Tsolidus)));
         qSCh(Rx,m) = vc*rholiquid*((cpliquid*(sphSt(Rx,m)-Tliquidus))+(cpsolid*(Tsolidus-Tbini))+(cpave*(Tliquidus-Tsolidus)));
         qLCh(Rx,m) = vc*rholiquid*Lhm;
      end
      if (Tliquidus >= sphSt(Rx,m)) && (sphSt(Rx,m)>=Tsolidus)
         Lf(Rx,m) = (sphSt(Rx,m)-Tsolidus)/(Tliquidus-Tsolidus);
```

```
            qCh(Rx,m) = vc*rholiquid*((Lf(Rx,m)*Lhm)+(cpsolid*(Tsolidus-Tbini)));
            qSCh(Rx,m) = vc*rholiquid*(cpsolid*(Tsolidus-Tbini));
            qLCh(Rx,m) = vc*rholiquid*(Lf(Rx,m)*Lhm);
         end
         if sphSt(Rx,m)<Tsolidus
            Lf(Rx,m) = 0;
            qCh(Rx,m) = vc*rhosolid*cpsolid*(sphSt(Rx,m)-Tbini);
            qSCh(Rx,m) = vc*rhosolid*cpsolid*(sphSt(Rx,m)-Tbini);
            qLCh(Rx,m) = 0;
         end

   end

   qChTotal(q) = (0.5*sum(qCh(:,1)))+sum(sum(qCh(:,2:Nx-1)))+(0.5*sum(qCh(:,Nx)));
   qSChTotal(q) = (0.5*sum(qSCh(:,1)))+sum(sum(qSCh(:,2:Nx-1)))+(0.5*sum(qSCh(:,Nx)));
   qLChTotal(q) = (0.5*sum(qLCh(:,1)))+sum(sum(qLCh(:,2:Nx-1)))+(0.5*sum(qLCh(:,Nx)));


if q == 1
   EstoreHat(1) = qChTotal(1);
   SstoreHat(1) = qSChTotal(1);
   ExstoreHat(1) = exChTotal(1);
   LstoreHat(1) = qLChTotal(1);

else
   EstoreHat(q) = qChTotal(q) - qDchTotal(q-1);
   ExstoreHat(q) = exChTotal(q) - exDchTotal(q-1);
   LstoreHat(q) = qLChTotal(q) - qLDchTotal(q-1);
   SstoreHat(q) = qSChTotal(q) - qSDchTotal(q-1);
end

%*****************Calculcating charging 1st Law efficiency*****************

Epumpch = (Pdch*mdotch*(Chargetime(q)+1)*60)/rhoHTF; %Pumping energy consumption.
%Einflow = mdotch*cpAirIn*(Tai-Tinf)*Chargetime(q)*60; %(Tinf)Energy into system.
EinNetch(q) = sum(QInNetCh(:,q)); %Total energy leaving system (or energy removed from air going
into bed)
Eloss = sum(QlossCh(:,q)); %Total energy lost.
EsaltStore(q) = rhoHTF*Abed*ep*deltax*cpHTF*(sum(TaSt(2:(Nx-1),1)-TaStIni(2:(Nx-
1),1))+(0.5*(TaSt(1,1)-TaStIni(1,1)))+(0.5*(TaSt(Nx,1)-TaStIni(Nx,1)))); %Energy stored in salt at end
of charging
EstoreTotal(q) = EstoreHat(q)+EsaltStore(q);
EffCh(q) = (EstoreHat(q)+EsaltStore(q))/EinNetch(q)

CapFact(q) = EstoreHat(q)/QbedMax  %Capacity ratio
CapFactL(q) = LstoreHat(q)/QbedMax
CapFactS(q) = SstoreHat(q)/QbedMax
CapRatio(q) = qChTotal(q)/QbedMax
effectivenessCh(q) = EinNetch(q)/(mdotch*cpHTF*(Tai-Tbi)*Chargetime(q)*60)
```

```
%*************Calculating charging 2nd Law efficiency*********************

%Exergy calculations:  *****************************************************
ExHTFChIn(q) = mdotch*cpHTF*60*Chargetime(q)*((Tai+273.15)-(Tinf+273.15)-
((Tinf+273.15)*log((Tai+273.15)/(Tinf+273.15))));
ExHTFChNetIn(q) = sum(NetExIn(:,q)); %Net exergy in (Exergy inflow - Exergy outflow)

ExEffCh(q) = (ExstoreHat(q)+ExSaltStore(q))/(ExHTFChNetIn(q)) %Charging exergetic efficiency
based on net inflow.



%*************************************************************************
%*******************Start Discharging conditions**************************
%*************************************************************************

%Setting up Initial condition for Discharging mode

%HTF Initial condition; note that t= 1 is before heating starts.
TaDSt(:,1) = flipud(TaSt(:,1));  %Takes last time step from charging, flips it and makes it initial condition
of discharging.
TaDStIni(:,1) = flipud(TaSt(:,1)); %Sets initial condition of air during discharging mode for efficiency
calculations.


%Solid Initial condition; at time = 1, heating hasn't started
sphDSt = fliplr(sphSt); %arranges columns in reverse order so that the HTF enters bottom of bed
TbDStIni(:,1) = flipud(TbSt(:,1)); %Sets initial condition of PCM during discharging mode for efficiency
calculations

breakflagD = false;  %flag to exit outer loop

    %Bed and air temperature calculations - Discharging mode
    for t = 1:1:cyclestepdch

      %d(1) = Taia(t,1); %Sets the temperature during this minute to the input temperature for all time
steps.
      d(1) = Tbi; %Inlet temperature during discharging is Tbi.

     %Calculating t minutes of discharging. "i" is each time step

      for i = 1:1:(tcolumn)  %Calculating tz minutes of charging."i" is each time step

          if TaDSt(Nx,1) <= TminDch
            breakflagD = true;
            break
          end

          for m = 2:1:Nx
```

```
   d(m,1) = TaDSt(m,1)+(hoverallVdch*Be*sphDSt(1,m))+(Tinf*(Uloss*Dbed*pi*Be/Abed));
end

TaDSt = K\d;

for m = 1:1:az   %1:1:Nx/3
   for n = 2:1:Rx-1
     rx = Ri-((n-1)*deltar);
     if sphDSt(n,m) > TliquidusD3
        B(n,n-1) = -(FolSolid+(FolSolid*deltar/rx));
        B(n,n) = (2*FolSolid)+1;
        B(n,n+1) = (FolSolid*deltar/rx)-FolSolid;
     end
     if  (TliquidusD3 >= sphDSt(n,m)) && (sphDSt(n,m)>= TsolidusD3)
        Cp = cpave+(Lhs3/(TliquidusD3-TsolidusD3));
        %Cp = cpsolid+((cpliquid-cpsolid)*(1/(1+exp(-zeta*(sphSt(n,m)-Tmelt)))))+((Lhm*zeta)/((exp(-zeta*(sphSt(n,m)-Tmelt)))+(exp(zeta*(sphSt(n,m)-Tmelt)))+2));
        Fop1 = (kave*ksolidify*deltat)/(rhoave*Cp*(deltar^2));
        B(n,n-1) = -(Fop1+(Fop1*deltar/rx));
        B(n,n) = (2*Fop1)+1;
        B(n,n+1) = (Fop1*deltar/rx)-Fop1;
     end
     if sphDSt(n,m) < TsolidusD3
        B(n,n-1) = -(FosSolid+(FosSolid*deltar/rx));
        B(n,n) = (2*FosSolid)+1;
        B(n,n+1) = (FosSolid*deltar/rx)-FosSolid;
     end
   end
  %Surface of sphere boundary condition
  B(1,1) = hoveralldch+(ksolid*ksolidify/deltar);
  B(1,2) = -ksolid*ksolidify/deltar;


  %Center of sphere boundary condition
  if sphDSt(Rx,m) > TliquidusD3
     B(Rx,Rx-1) = -6*FolSolid;
     B(Rx,Rx) = 1+(6*FolSolid);
  end
  if  (TliquidusD3 >= sphDSt(Rx,m)) && (sphDSt(Rx,m)>=TsolidusD3)
     Cp = cpave+(Lhs3/(TliquidusD3-TsolidusD3));
     %Cp = cpsolid+((cpliquid-cpsolid)*(1/(1+exp(-zeta*(sphDSt(Rx,m)-Tmelt)))))+((Lhm*zeta)/((exp(-zeta*(sphDSt(Rx,m)-Tmelt)))+(exp(zeta*(sphDSt(Rx,m)-Tmelt)))+2));
     Fop1 = (kave*ksolidify*deltat)/(rhoave*Cp*(deltar^2));
     B(Rx,Rx-1) = -6*Fop1;
     B(Rx,Rx) = 1+(6*Fop1);
  end
  if sphDSt(Rx,m) < TsolidusD3
     B(Rx,Rx-1) = -6*FosSolid;
     B(Rx,Rx) = 1+(6*FosSolid);
  end
```

```
          %Calculate new temperature
           g(2:Rx) = sphDSt(2:Rx,m);
           g(1) = hoveralldch*TaDSt(m,1);

           z = B\g;

           sphDSt(:,m) = z(:,1);
        end

        for m = (az+1):1:bz  %((Nx/3)+1):1:(2*Nx/3)
           for n = 2:1:Rx-1
             rx = Ri-((n-1)*deltar);
             if sphDSt(n,m) > TliquidusD2
                B(n,n-1) = -(FolSolid+(FolSolid*deltar/rx));
                B(n,n) = (2*FolSolid)+1;
                B(n,n+1) = (FolSolid*deltar/rx)-FolSolid;
             end
             if  (TliquidusD2 >= sphDSt(n,m)) && (sphDSt(n,m)>= TsolidusD2)
                Cp = cpave+(Lhs2/(TliquidusD2-TsolidusD2));
                %Cp = cpsolid+((cpliquid-cpsolid)*(1/(1+exp(-zeta*(sphSt(n,m)-
Tmelt)))))+((Lhm*zeta)/((exp(-zeta*(sphSt(n,m)-Tmelt)))+(exp(zeta*(sphSt(n,m)-Tmelt)))+2));
                Fop2 = (kave*ksolidify*deltat)/(rhoave*Cp*(deltar^2));
                B(n,n-1) = -(Fop2+(Fop2*deltar/rx));
                B(n,n) = (2*Fop2)+1;
                B(n,n+1) = (Fop2*deltar/rx)-Fop2;
            end
             if sphDSt(n,m) < TsolidusD2
                B(n,n-1) = -(FosSolid+(FosSolid*deltar/rx));
                B(n,n) = (2*FosSolid)+1;
                B(n,n+1) = (FosSolid*deltar/rx)-FosSolid;
             end
           end
          %Surface of sphere boundary condition
          B(1,1) = hoveralldch+(ksolid*ksolidify/deltar);
          B(1,2) = -ksolid*ksolidify/deltar;


          %Center of sphere boundary condition
          if sphDSt(Rx,m) > TliquidusD2
             B(Rx,Rx-1) = -6*FolSolid;
             B(Rx,Rx) = 1+(6*FolSolid);
          end
          if  (TliquidusD2 >= sphDSt(Rx,m)) && (sphDSt(Rx,m)>=TsolidusD2)
             Cp = cpave+(Lhs2/(TliquidusD2-TsolidusD2));
             %Cp = cpsolid+((cpliquid-cpsolid)*(1/(1+exp(-zeta*(sphDSt(Rx,m)-
Tmelt)))))+((Lhm*zeta)/((exp(-zeta*(sphDSt(Rx,m)-Tmelt)))+(exp(zeta*(sphDSt(Rx,m)-Tmelt)))+2));
             Fop2 = (kave*ksolidify*deltat)/(rhoave*Cp*(deltar^2));
             B(Rx,Rx-1) = -6*Fop2;
             B(Rx,Rx) = 1+(6*Fop2);
          end
```

```
          if sphDSt(Rx,m) < TsolidusD2
             B(Rx,Rx-1) = -6*FosSolid;
             B(Rx,Rx) = 1+(6*FosSolid);
          end
          %Calculate new temperature
           g(2:Rx) = sphDSt(2:Rx,m);
           g(1) = hoveralldch*TaDSt(m,1);

           z = B\g;

           sphDSt(:,m) = z(:,1);
        end
        for m = (bz+1):1:Nx  %((2*Nx/3)+1):1:Nx
           for n = 2:1:Rx-1
             rx = Ri-((n-1)*deltar);
             if sphDSt(n,m) > TliquidusD1
                B(n,n-1) = -(FolSolid+(FolSolid*deltar/rx));
                B(n,n) = (2*FolSolid)+1;
                B(n,n+1) = (FolSolid*deltar/rx)-FolSolid;
             end
             if  (TliquidusD1 >= sphDSt(n,m)) && (sphDSt(n,m)>= TsolidusD1)
                Cp = cpave+(Lhs1/(TliquidusD1-TsolidusD1));
                %Cp = cpsolid+((cpliquid-cpsolid)*(1/(1+exp(-zeta*(sphSt(n,m)-
Tmelt)))))+((Lhm*zeta)/((exp(-zeta*(sphSt(n,m)-Tmelt)))+(exp(zeta*(sphSt(n,m)-Tmelt)))+2));
                Fop3 = (kave*ksolidify*deltat)/(rhoave*Cp*(deltar^2));
                B(n,n-1) = -(Fop3+(Fop3*deltar/rx));
                B(n,n) = (2*Fop3)+1;
                B(n,n+1) = (Fop3*deltar/rx)-Fop3;
             end
             if sphDSt(n,m) < TsolidusD1
                B(n,n-1) = -(FosSolid+(FosSolid*deltar/rx));
                B(n,n) = (2*FosSolid)+1;
                B(n,n+1) = (FosSolid*deltar/rx)-FosSolid;
             end
           end
          %Surface of sphere boundary condition
          B(1,1) = hoveralldch+(ksolid*ksolidify/deltar);
          B(1,2) = -ksolid*ksolidify/deltar;


          %Center of sphere boundary condition
          if sphDSt(Rx,m) > TliquidusD1
             B(Rx,Rx-1) = -6*FolSolid;
             B(Rx,Rx) = 1+(6*FolSolid);
          end
          if  (TliquidusD1 >= sphDSt(Rx,m)) && (sphDSt(Rx,m)>=TsolidusD1)
             Cp = cpave+(Lhs1/(TliquidusD1-TsolidusD1));
             %Cp = cpsolid+((cpliquid-cpsolid)*(1/(1+exp(-zeta*(sphDSt(Rx,m)-
Tmelt)))))+((Lhm*zeta)/((exp(-zeta*(sphDSt(Rx,m)-Tmelt)))+(exp(zeta*(sphDSt(Rx,m)-Tmelt)))+2));
             Fop3 = (kave*ksolidify*deltat)/(rhoave*Cp*(deltar^2));
```

```
          B(Rx,Rx-1) = -6*Fop3;
          B(Rx,Rx) = 1+(6*Fop3);
       end
       if sphDSt(Rx,m) < TsolidusD1
          B(Rx,Rx-1) = -6*FosSolid;
          B(Rx,Rx) = 1+(6*FosSolid);
       end
       %Calculate new temperature
        g(2:Rx) = sphDSt(2:Rx,m);
        g(1) = hoveralldch*TaDSt(m,1);

        z = B\g;

        sphDSt(:,m) = z(:,1);
     end


end
%Calculation of volume averaged solid temperature:
 for m = 1:1:Nx
    %Average sphere temperature at first control volume of sphere:
    TbAveD(1) = ((4/3)*pi*((Ri^3)-((Ri-(deltar/2))^3)))*sphDSt(1,m);
    for n = 2:1:Rx-1
       rx1 = Ri-((n-1)*deltar);
       v1 = ((4/3)*pi*((rx1+(deltar/2))^3));
       v2 = ((4/3)*pi*((rx1-(deltar/2))^3));
       TbAveD(n) = (v1-v2)*sphDSt(n,m);
    end
    %Average sphere temperature at center of sphere.
    TbAveD(Rx) = (4/3)*pi*((deltar/2)^3)*(sphDSt(Rx,m));

    TbDSt(m,1) = sum(TbAveD)/Vpi;
 end

 TbfirstD(:,t) = sphDSt(2,:).';
 TbcenterD(:,t) = sphDSt(Rx,:).';
 ThalfD(:,t) = sphDSt((Rx/2),:).';
 TaD(:,t) = TaDSt(:,1);
 TbD(:,t) = TbDSt(:,1);

 %Exporting the (tz)th minute into excel:
 Tairdischarge(1,t) = t*tz; %Places the number of minutes of charging in the 1st row.
 Tbeddischarge(1,t) = t*tz; %Note that the 1st column is reserved for the initial time.
 TbedcenterD(1,t) = t*tz;
 TbedfirstD(1,t) = t*tz;
 TbedhalfD(1,t) = t*tz;
 for m = 2:Nx+1     %Places the last time step in the correct column of the excel table.
    Tairdischarge(m,t) = TaD(m-1,t);
    Tbeddischarge(m,t) = TbD(m-1,t);
    TbedcenterD(m,t) = TbcenterD(m-1,t);
```

```
             TbedfirstD(m,t) = TbfirstD(m-1,t);
             TbedhalfD(m,t) = TbhalfD(m-1,t);
         end

         %Calculating the amount of energy discharged from the bed at each
         %minute:
         EoutflowD(t,q) = mdotdch*cpHTF*(TaDSt(Nx,1)-Tbi)*60;

         %Calculating energy losses per minute:
         QlossDch(t,q) = (Uloss*Dbed*pi*deltax*sum(Tinf-TaDSt(2:Nx-
1,1))*60)+(Uloss*Dbed*pi*0.5*deltax*((Tinf-TaDSt(1,1))+(Tinf-TaDSt(Nx,1)))*60);

         %Calculating Net Exergy into system per minute:
         NetExOut(t,q) = mdotdch*cpHTF*((TaDSt(Nx,1)+273.15)-(Tbi+273.15)-
((Tinf+273.15)*log((TaDSt(Nx,1)+273.15)/(Tbi+273.15))))*60;

         if breakflagD == true
             break
         end
     end

     Dischargetime(q) = t-1 %Discharging time in minutes


    %Calculating energy stored in tank:
    for m = 1:1:Nx
           if (m >= 1) && (m <= az)
             TliquidusD = TliquidusD3;
               TsolidusD = TsolidusD3;
               Lhs = Lhs3;
               Tsolidify = Tsolidify3;
           end
           if (m > az) && (m <= bz)
               TliquidusD = TliquidusD2;
               TsolidusD = TsolidusD2;
               Lhs = Lhs2;
               Tsolidify = Tsolidify2;
           end
           if (m > bz) && (m <= Nx)
               TliquidusD = TliquidusD1;
               TsolidusD = TsolidusD1;
               Lhs = Lhs1;
               Tsolidify = Tsolidify1;
           end
        %Average energy stored at first control volume of sphere:
            vo = (((4/3)*pi*((Ri^3)-((Ri-(deltar/2))^3)))*Abed*(1-ep)*deltax)/Vpi;
            if sphDSt(1,m) > TliquidusD
                LfD(1,m) = 1;
                qDch(1,m) = vo*rholiquid*((cpliquid*(sphDSt(1,m)-TliquidusD))+Lhs+(cpsolid*(TsolidusD-
Tbini))+(cpave*(TliquidusD-TsolidusD)));
```

```
       qSDch(1,m) = vo*rholiquid*((cpliquid*(sphDSt(1,m)-TliquidusD))+(cpsolid*(TsolidusD-Tbini))+(cpave*(TliquidusD-TsolidusD)));
       qLDch(1,m) = vo*rholiquid*Lhs;
    end
    if (TliquidusD >= sphDSt(1,m)) && (sphDSt(1,m)>=TsolidusD)
       LfD(1,m) = (sphDSt(1,m)-TsolidusD)/(TliquidusD-TsolidusD);
       qDch(1,m) = vo*rholiquid*((LfD(1,m)*Lhs)+(cpsolid*(TsolidusD-Tbini)));
       qSDch(1,m) = vo*rholiquid*(cpsolid*(TsolidusD-Tbini));
       qLDch(1,m) = vo*rholiquid*(LfD(1,m)*Lhs);
    end
    if sphDSt(1,m)<TsolidusD
       LfD(1,m) = 0;
       qDch(1,m) = vo*rhosolid*cpsolid*(sphDSt(1,m)-Tbini);
       qSDch(1,m) = vo*rhosolid*cpsolid*(sphDSt(1,m)-Tbini);
       qLDch(1,m) = 0;
    end
    for n = 2:1:Rx-1
       rx1 = Ri-((n-1)*deltar);
       v1 = ((4/3)*pi*((rx1+(deltar/2))^3));
       v2 = ((4/3)*pi*((rx1-(deltar/2))^3));
       vi = ((v1-v2)*Abed*(1-ep)*deltax)/Vpi;
       if sphDSt(n,m) > TliquidusD
          LfD(n,m) = 1;
          qDch(n,m) = vi*rholiquid*((cpliquid*(sphDSt(n,m)-TliquidusD))+Lhs+(cpsolid*(TsolidusD-Tbini))+(cpave*(TliquidusD-TsolidusD)));
          qSDch(n,m) = vi*rholiquid*((cpliquid*(sphDSt(n,m)-TliquidusD))+(cpsolid*(TsolidusD-Tbini))+(cpave*(TliquidusD-TsolidusD)));
          qLDch(n,m) = vi*rholiquid*Lhs;
       end
       if (TliquidusD >= sphDSt(n,m)) && (sphDSt(n,m)>=TsolidusD)
          LfD(n,m) = (sphDSt(n,m)-TsolidusD)/(TliquidusD-TsolidusD);
          qDch(n,m) = vi*rholiquid*((LfD(n,m)*Lhs)+(cpsolid*(TsolidusD-Tbini)));
          qSDch(n,m) = vi*rholiquid*(cpsolid*(TsolidusD-Tbini));
          qLDch(n,m) = vi*rholiquid*(LfD(n,m)*Lhs);
       end
       if sphDSt(n,m)<TsolidusD
          LfD(n,m) = 0;
          qDch(n,m) = vi*rhosolid*cpsolid*(sphDSt(n,m)-Tbini);
          qSDch(n,m) = vi*rhosolid*cpsolid*(sphDSt(n,m)-Tbini);
          qLDch(n,m) = 0;

       end
    end
    %Energy stored at center of sphere:
    vc = (4/3)*pi*((deltar/2)^3)*Abed*(1-ep)*deltax/Vpi;
    if sphDSt(Rx,m) > TliquidusD
       LfD(Rx,m) = 1;
       qDch(Rx,m) = vc*rholiquid*((cpliquid*(sphDSt(Rx,m)-TliquidusD))+Lhs+(cpsolid*(TsolidusD-Tbini))+(cpave*(TliquidusD-TsolidusD)));
```

```
            qSDch(Rx,m) = vc*rholiquid*((cpliquid*(sphDSt(Rx,m)-TliquidusD))+(cpsolid*(TsolidusD-Tbini))+(cpave*(TliquidusD-TsolidusD)));
            qLDch(Rx,m) = vc*rholiquid*Lhs;
         end
         if (TliquidusD >= sphDSt(Rx,m)) && (sphDSt(Rx,m)>=TsolidusD)
            LfD(Rx,m) = (sphDSt(Rx,m)-TsolidusD)/(TliquidusD-TsolidusD);
            qDch(Rx,m) = vc*rholiquid*((LfD(Rx,m)*Lhs)+(cpsolid*(TsolidusD-Tbini)));
            qSDch(Rx,m) = vc*rholiquid*(cpsolid*(TsolidusD-Tbini));
            qLDch(Rx,m) = vc*rholiquid*(LfD(Rx,m)*Lhs);
         end
         if sphDSt(Rx,m)<TsolidusD
            LfD(Rx,m) = 0;
            qDch(Rx,m) = vc*rhosolid*cpsolid*(sphDSt(Rx,m)-Tbini);
            qSDch(Rx,m) = vc*rhosolid*cpsolid*(sphDSt(Rx,m)-Tbini);
            qLDch(Rx,m) = 0;
         end

   end

   qDchTotal(q) = (0.5*sum(qDch(:,1)))+sum(sum(qDch(:,2:Nx-1)))+(0.5*sum(qDch(:,Nx)));
   qSDchTotal(q) = (0.5*sum(qSDch(:,1)))+sum(sum(qSDch(:,2:Nx-1)))+(0.5*sum(qSDch(:,Nx)));
   qLDchTotal(q) = (0.5*sum(qLDch(:,1)))+sum(sum(qLDch(:,2:Nx-1)))+(0.5*sum(qLDch(:,Nx)));

if q == 1
   EstoreHatD(1) = qDchTotal(1);
   ExstoreHatD(1) = exDchTotal(1);
else
   EstoreHatD(q) = qChTotal(q) - qDchTotal(q);
   ExstoreHatD(q) = exChTotal(q) - exDchTotal(q);
end

SensibleOut(q) = qSChTotal(q) - qSDchTotal(q);
LatentOut(q) = qLChTotal(q) - qLDchTotal(q);

%Calculating Utilization factor:

Utotal(q) = (SensibleOut(q)+LatentOut(q))/QbedMax %Total utilization
Usensible(q) = SensibleOut(q)/QbedMax %Sensible Heat Utilization
Ulatent(q) = LatentOut(q)/QbedMax %Latent Heat Utilization
LatentRatio(q) = LatentOut(q)/QlatentMax; %Ratio of discharged latent heat over max Latent heat
LatentStore(q) = qLChTotal(q)/QlatentMax; %Ratio of stored latent heat over max Latent heat.
LatentEff(q) = LatentOut(q)/qLChTotal(q) %Ratio of latent heat extracted over latent heat actually stored
SensibleEff(q) = SensibleOut(q)/qSChTotal(q)

%Calculating discharging efficiency:
EpumpDch = (Pdch*Abed*Gdch*(1+Dischargetime(q))*60)/rhoHTF; %Pumping energy consumption. (joules)
EoutDch(q) = sum(EoutflowD(:,q)); %Energy discharged from system (joules)
EoutDchWh(q) = EoutDch(q)/(3600*10^6) %Energy discharged (MWh)
ELossDch(q) = sum(QlossDch(:,q));
```

```
EffDch(q) = EoutDch(q)/(EstoreHat(q)+EsaltStore(q)) %Discharging efficiency
EffOverall(q) = EffDch(q)*EffCh(q)
EffOverallT(q) = EoutDch(q)/(EinNetch(q)+EpumpDch+Epumpch)

%*************Calculating discharging 2nd Law efficiency********************
%Exergy calculations:  ***************************************************
ExHTFDchNetOut(q) = sum(NetExOut(:,q)); %Net exergy out (Exergy outflow - Exergy inflow)

%Dicharging exergetic efficiency based on net outflow and pump work.
ExEffDch(q) = (ExHTFDchNetOut(q))/(ExstoreHat(q)+ExSaltStore(q))

ExEffOverall(q) = ExEffDch(q)*ExEffCh(q) %Overall exergetic efficiency
ExEffOverallT(q) = ExHTFDchNetOut(q)/(ExHTFChNetIn(q)+EpumpDch+Epumpch)

xlswrite('LHS_parametric_HTF.xlsx',Taircharge,xlssheetnames{count});
xlswrite('LHS_parametric_PCM.xlsx',Tbedcharge,xlssheetnames{count});
xlswrite('LHS_parametric_PCM.xlsx', Tbeddischarge,xlssheetnames{count+1});


TaSt(:,1) = flipud(TaDSt(:,1));  %Takes last time step from discharging, flips it and makes it initial condition of charging of next cycle.
TaStIni(:,1) = flipud(TaDSt(:,1)); %Sets initial condition of air during charging mode for efficiency calculations.
sphSt = fliplr(sphDSt); %arranges columns in reverse order so that the air enters top of bed for next charging cycle.
TbStIni(:,1) = flipud(TbDSt(:,1)); %Sets initial condition of PCM during charging mode for efficiency calculations.
sphStIni = fliplr(sphDSt); %sets initial temperature within each particle for next chargning cycle.

count = count+2;
Taircharge = [];
Tairdischarge = [];
Tbedcharge = [];
Tbeddischarge = [];
end
```

D.2 HTF Properties

```
function [rho,mu,cp,k] = HTFprops(x,Tave);
%This function provides the properties of the selected HTF, either air or
%salt.
%Written by Jamie Trahan, December 12, 2014
%If x == 1, the HTF is air
%If x == 2, the HTF is salt
%_______________________________________________________________________________


if x == 1
```

```
    rho = ((-5.75399E-16)*(Tave^5))+((3.02846E-12)*(Tave^4))-((6.18352E-9)*(Tave^3))+((6.29927E-
6)*(Tave^2))-((3.5422E-3)*Tave)+1.25079; %density of air (kg/m3)
    mu = (((6.10504E-10)*(Tave^3))-((2.13036E-6)*(Tave^2))+((4.71398E-3)*(Tave))+1.67555)*(10^-5);
%Dynamic viscosity of air (kg/ms)
    cp = (((1.28806E-13)*(Tave^4))-((4.46054E-10)*(Tave^3))+((4.8772E-7)*(Tave^2))+((1.82754E-
5)*Tave)+1.00651)*1000; %Cp of air (J/kg-K)
    k = ((-4.44955E-15)*(Tave^4))+((2.41702E-11)*(Tave^3))-((4.09601E-8)*(Tave^2))+((7.91034E-
5)*Tave)+.0242006; % thermal conductivity of air (W/mK)
end

if x == 2
    rho = (-0.6357*Tave)+2089.9; %density of salt (kg/m3)
    mu = ((-1.473189317978e-10)*(Tave^3))+((2.279835623143e-07)*(Tave^2))-((1.199467889194e-
04)*Tave)+2.270644077145e-02; %Dynamic viscosity of air (kg/ms)
    cp = (0.172*Tave)+1443; %Cp of air (J/kg-K)
    k = (0.00019*Tave)+0.44299; % thermal conductivity of air (W/mK)

end
```

ABOUT THE AUTHOR

Jamie Trahan received her B.S. in biology with a focus in environmental studies from the University of Tampa. She then pursued a B.S. in mechanical engineering from the University of South Florida where she developed her background in renewable energy and founded a chapter of Engineers Without Borders. While pursuing her Ph.D. in mechanical engineering, she actively promoted the adoption of solar energy technology through educational outreach, having engaged in activities such as traveling the country with a world record-breaking solar powered car, and organizing Tampa Bay's first Solar Home Tour. She is an ASME Graduate Teaching Fellow and a Department of Education GAANN Fellow. Jamie is also the first recipient of Solar Energy International's Johnny Weiss Award and a recipient of the National Go Solar Foundation Evette Harless Award. She is the principal investigator of the USF Solar Initiative, a Student Green Energy Fund project that financed the installation of two photovoltaic systems at USF's Marshall Student center.